

FINAL REPORT

2009

Program Title: *Bioinspired Haircell Receptive Sensors*

Principle Investigator: *Chang Liu, Northwestern University*

*Mechanical Engineering Department
Northwestern University
Evanston, IL*

Phone: (847) 467 0701

E-mail: changliu@northwestern.edu

*Douglas Jones, University of Illinois
Department of Electrical and Computer Engineering*

Email: d-jones@uiuc.edu

Co-Principle Investigators: *Sheryl Coombs, Bowling Green University
Vladimir Tsukruk, Georgia Tech
Joseph Humphrey, University of Virginia
Douglas Jones, University of Illinois
Horst Bleckmann, University of Bonn
Friedrich Barth, University of Vienna
Rajesh Naik, Air Force Research Laboratory*

Agreement Number: *FA 9550-05-1-0459*

20120918090

ACCOMPLISHMENTS/NEW FINDINGS

- A cross-array artificial lateral line (ALL) was developed under the guidance of Cramer-Rao lower bound theory. It was then applied to mimic its biological counterpart for localization of underwater vibrating targets. Enabled by an adaptive beamforming algorithm, the 3-D hydrodynamic imaging of the ALL has been successfully demonstrated. Using this artificial intelligent system, a crayfish generated hydrodynamic disturbance was vividly imaged.
- A two-sided ALL was built on an AUV model, and ALL-enabled station keeping between two AUV models was realized. The flow interaction with the two models was correlated with ALL responses by means of particle image velocimetry in conjunction with ALL measurements. Various station-keeping positions were examined, and autonomous station keeping was demonstrated for the case of one AUV trailing another.
- Canalled artificial haircell sensor (AHC), which mimics canalled neuromasts of fish, was realized. The canalled structure over an AHC enabled two unique functions, which have been observed in its biological counterpart. They are the band-pass filtering feature and the reduction of the noise floor. These functions significantly improved the AHC's performance in noisy environments.
- Extensive characterization of AHC's performance in turbulent boundary layer flows was accomplished in conjunction with laser Doppler velocimetry and laser Doppler vibrometry. Correlation results by different means indicate that the AHC responded to turbulent flows very well at various Reynolds numbers. It is convincing that the AHC possesses strong potential for field applications.
- An artificial weak electrosense system inspired by electric fish was developed. Using a novel beamforming technique that exploits the sparsity of sources in a scanned space, the system is capable of accurately imaging multiple objects with highly correlated signals.
- By studying fish neuromasts and understanding the hydrogel-like cupula on top of a haircell, engineered cupula was developed and applied to an AHC. The engineered cupula replicates the material and the shape of a blind cavefish cupula. It dramatically enhanced the sensitivity of the cupula-capped AHC, which to some extent rivals that of fish neuromasts.
- Through studying spider hairs, a material-based mechanical signal filtering mechanism we were elucidated. A spider inspired two-tier hair has also been developed. The hair significantly enhanced the durability of the sensors and provided the ground-work for developing air-flow sensors capable of material-based signal filtering.
- A unique, flexible photoresist formulation was developed for improvement of AHCs. It resulted in highly defined polymer hairs that resist acids, bases, solvents, and high temperatures and humidity. The hairs also withstand over 1000 flexes, greatly improving on the durability of the original design of the AHC.
- A PEG-based coating was created for antifouling coating of the AHC. Desirable attributes of this coating are that it is ultra-thin, does not affect the sensitivity of the sensor, coats hidden areas, and is uniform and elastic. Additionally, this coating can be patterned, if desired. Since the process is easily modified, thinner or thicker coatings can also be applied.

- Analytical and numerical investigations on flow interactions with various biological sensing organs/units were carried out. The research topics cover: sensors and sensing in biology and engineering, arthropod motion sensing filiform hairs, fish neuromasts, and seal whiskers. The resulting physical-mathematical models were applied to quantitatively predict the performance characteristics of the biological sensing units in air and water.
- Behavioral studies on the orienting behavior of mottled sculpin have demonstrated that (i) local 'hot spots' in the spatial activation pattern of the lateral line can be ruled out as a mechanism of encoding the location of a vibratory source, and (ii) vibratory sources stimulate both lateral line and auditory systems, but that the auditory system dominates classically-conditioned (learned behaviors), whereas the lateral line dominates unconditioned orienting responses.
- Behavioral studies on active flow-sensing and wall-following behaviors of blind cavefish have demonstrated that (i) blind cavefish have evolved enhanced wall-following behaviors more finely honed for exploratory purposes than those of sighted morphs, (ii) artifactual explanations of wall-following behaviors can be ruled out, and (iii) wall-following in blind cavefish involves a regulatory mechanism in which tactile senses are likely to play a more dominant role in informing fish when they are too close to the wall, whereas the lateral line plays a more dominant role in informing them when they are too far away.
- Artificial lateral line canals (ALLCs) were further explored by means of video measurements, artificial neuromasts, and hydrodynamic calculations under various hydrodynamic conditions. It was revealed that ALLCs could be used to determine bulk flow velocity, object position and vortex shedding frequencies. Object size is a function of bulk flow velocity and vortex shedding frequency.
- Physiological study on the goldfish midbrain was conducted under dipole flow stimulation to the lateral line of the goldfish. It was found that single midbrain (toral) lateral line units of goldfish do not encode the position of an object. However, if the responses (spike rate and phase angle) of several midbrain lateral line units are taken into account, the position and vibration direction of a stationary sphere can be determined. Thus up to the level of the midbrain (torus semicircularis), the information about sphere position and sphere vibration direction is not encoded at the single unit level of but presumably as a population code.
- Through Physiological study on lateral line afferent fibers to hydrodynamic stimuli, in-depth understanding has been gained on: (i) how lateral line fibers respond to water currents, (ii) how the lateral line system encode velocity and direction of water currents, (iii) how water currents affect the detection of sinusoidal stimuli, and (iv) how fish detect hydrodynamic trails.
- On the study of airflows eliciting the capture of flying insect prey by a spider, in-depth understanding of the fundamental principles has been achieved. The sensors guiding the spider's behavior are very selectively adapted to specific tasks (as are all biological sensory systems). Mathematical modelling and experimental examination/exploration were performed on individual airflow sensors, sensor arrays, as well as airflow elicited spider behaviour on prey detection, recognition and localization.

BIOINSPIRED HAIRCELL SENSOR, ARTIFICIAL LATERAL LINE, AND THEIR BIOMIMETIC APPLICATIONS

(PI Chang Liu, Northwestern University, Evanston, IL)

Objectives

This project aims to develop biomimetic sensors with their architectures inspired by the biological haircells, a sensing element commonly found in many species of the biological world. The haircells are used for hearing and balance (e.g. human inner ear), for flow sensors (e.g. cerci organs of certain insects), for contact sensing (skin), and for imaging of fluid fields (e.g. lateral line of fish). We focus on designing the basic artificial haircell unit, and applying them for enabling artificial lateral line (ALL). The ALL is to be implemented on autonomous underwater vehicles (AUV) for localization of underwater vibrating objects and for tracking the wake of a propeller driven vehicle.

The original technical objectives were modified twice during the execution of our phase II efforts: (i) Wake following was replaced by station keeping. This adjustment was made during the program review on February 11 - 12, 2008 at DARPA, suggested by DAPAR program manager Dr. Hylton. The new objective copes better with navy's immediate interests. (ii) Station keeping was later aborted after some successful preliminary demonstration; the remaining effort was then shifted to characterization of the haircell sensors under turbulent boundary layer flow conditions. This adjustment was made by DARPA program manager Dr. Furey during her visit to Northwestern University on February 24, 2009.

ALL-enabled hydrodynamic imaging and prey localization

The lateral line is a hydrodynamic imaging system found in fish and aquatic amphibians (Figure1A). It consists of numerous hair-cell sensors called neuromasts (Figure 1B). They are distributed all over the fish body, with many of them situated on the surface of the skin and others in subepidermal canals. Each neuromast functions as a flow sensor to gather local hydrodynamic information. The drag force acting on the neuromast from moving fluid causes the cupula of the neuromast to bend or slide. The movement of the cupula further leads to the deflection of the ciliary bundles inside the cupula, and elicits neuron-spiking activities of the underlying hair cells (Figure1C). With arrays of neuromasts along the body functioning as the lateral-line system, fish are able to encode spatial excitation patterns of a hydrodynamic stimulus, and thus image this event and respond to it. It has been shown that the lateral line allows fish to navigate in the absence of vision and chemosense.

A man-made lateral-line system can be indispensable for underwater vehicles and robots, enabling new ways of exploration, interaction, and communication. The lateral line sense can supplement the current underwater sensing methods, including sonar and vision, in important ways. In the long term, the bio-inspired sensing technique also will provide an engineered platform that can be used to test biological hypotheses. As a breakthrough in our cumulative research along this line, we have presently developed a prototype artificial lateral line (ALL) consisting of a three-dimensional system of biomimetic neuromasts – artificial haircell sensors (AHCs) wrapped around a cylinder (Fig 1D).

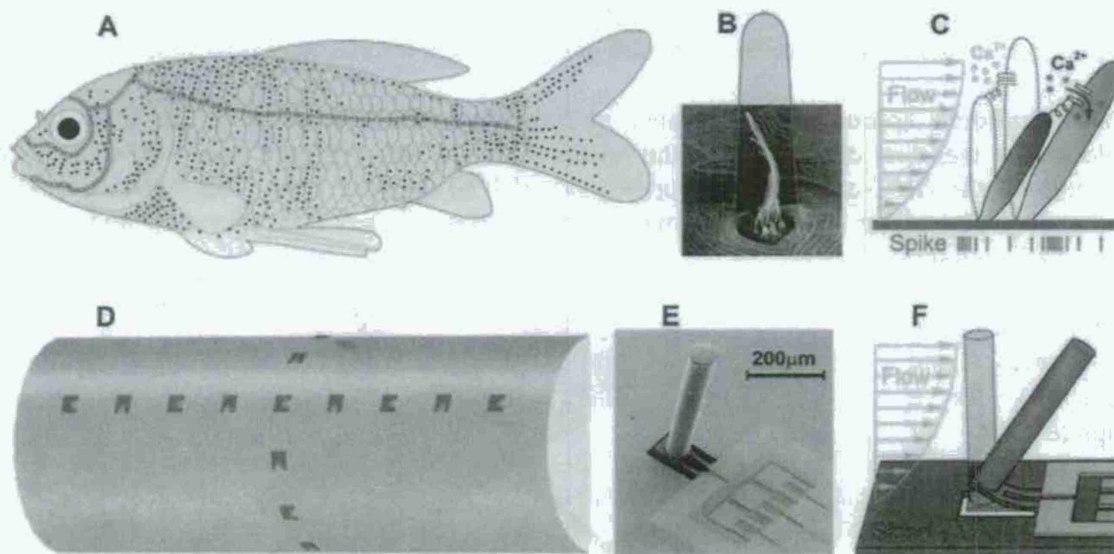


Figure 1: *A*, fish lateral line. *B*, neuromast. *C*, neuromast sensing mechanism. *D*, artificial lateral line. *E*, Artificial haircell sensor (ALL). *F*, ALL sensing mechanism.

Each individual AHC consists of a horizontal cantilever with a vertical hair attached at the distal end (Figure 1E). Each hair is 500µm tall in the current design. In comparison, the cupulae of fish lateral line neuromasts range in height from about 20 µm to at least 500 µm, depending on the species. At the fixed end of the horizontal cantilever, a piezoresistor is embedded by selective doping of silicon material. Flow impinges upon the vertical hair and therefore creates a bending torque (Figure 1F), which acts on the horizontal cantilever to induce stress concentration at the site of the piezoresistor. The change of the resistance, which can be easily converted to voltage variation (e.g., through the use of a Wheatstone bridge), is used to infer the local flow velocity.

While exposed in a flow, the AHC is only sensitive to the local velocity component along the longitudinal direction of the horizontal cantilever. This direction is termed the dominant axis. Sensitivity to cross-flow is zero in ideal cases. Along the dominant axis, the sensor responds to flow in both directions with equal sensitivity but opposite polarity. The detection limit for water flow along the dominant axis is as low as 0.1 mm/sec.

14 AHCs constitute the ALL for the present study (Figure 1D). They are laid out along a cylindrical surface to form a branched configuration. Along each branch, we alternate the dominant axes of neighboring AHCs by 90° (Figure 2, top diagram). This AHC configuration was selected by means of numerical evaluation of the Cramer-Rao lower bound to achieve the best 3-D localization performance with a limited number of sensors. The orthogonal arrangement of AHC sensing directions has been observed in many fish possessing neuromasts with polarized sensing property.

A constant-volume sinusoidally-vibrating sphere in water, referred to hereafter as a dipole source, has been commonly used as a hydrodynamic stimulus in physiological and/or performance studies on the lateral line organ. The dipole source emulates the tail beating or appendage movement of aquatic animals that generate a dipole-dominant flow field.

In our biomimetic approach, the response of individual AHCs in water in the presence of a dipole source was first characterized; the results matched well with the analytical model. We then exposed the AHC-constituted, wrap-around ALL to a dipole field. The individual AHCs simultaneously picked up local hydrodynamic information at each AHC location and over the entire ALL stretch

(Figure 2, yellow box for a portion of the signals, and Figure 3A for a complete set of ALL response). We developed a mathematical algorithm (discussed below) to localize the dipole source using the information from these spatially distributed AHCs.

To utilize the seemingly chaotic multi-channel signals from the spatially distributed AHCs to localize the dipole source, we developed artificial intelligence – a beamforming algorithm. The algorithm (Figure 2) is based on the pattern-recognition principles, which is similar to fish that use lateral-line-encoded spatial

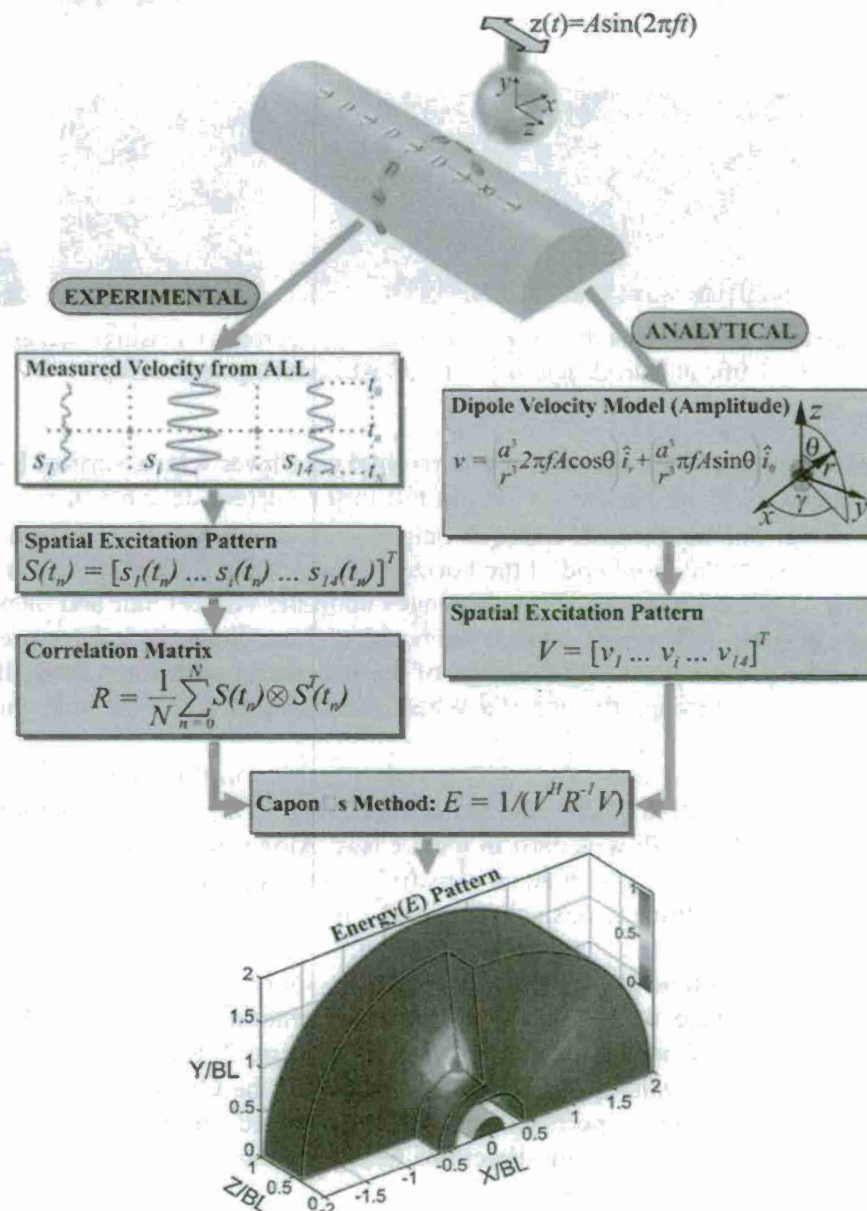


Figure 2: Algorithm for hydrodynamic imaging and prey localization.

excitation patterns for localization.

Two branches – experimental (Figure 2, left) and analytical (Figure 2, right), jointly function to fulfill the localization. On the experimental branch, at each sample instant t_n a spatial excitation pattern $S(t_n)$ (one sample from each AHC) is formed, and over all the sample instants (from t_0 to t_N) a correlation matrix R is computed. On the analytical branch, a spatial excitation pattern V is obtained from the dipole velocity model by calculating the local velocity amplitude at each AHC position and by projecting it to the AHC's dominant axis; this is done by assuming a dipole location (X, Y, Z) and orientation (azimuth and zenith angles) with respect to the ALL. By combining experimental and analytical results, Capon's method eventually gives the energy (E) level at that assumed dipole state (location and orientation). Systematically assuming dipole state in a predefined 5-D domain and repeating the process yield a 5-D energy distribution, which correlates to the likelihood with the peak representing the best prediction.

After the beamforming process, the predicted dipole location is determined by identifying the coordinates of the location with the highest energy level. A typical energy pattern yielded from a 5-D search is presented in color code in a 3-D domain (Figure 2, bottom plot). The 3-D pattern is obtained by, at each spatial-search point, taking the maximum among the values produced by all the orientation-search points. Such representation demonstrates the capability of the ALL for 3-D hydrodynamic imaging.

Using the spatial-temporal responses of the ALL (Figure 3), the localization performance of the algorithm-implemented ALL was examined at various representative dipole states (Figure 4). In biological studies the range of fish localization capability is often measured in terms of body

length (BL). Here, we define the length of the AHC array along the cylinder as the BL. With the dipole source having a fixed distance of $0.5BL$ to the surface of the cylinder and the dipole orientation along the cylinder, localization is successful at all the testing locations as shown (Figure 4). For each location examined, the 3-D energy distribution presents a well-defined high-likelihood spot (dark red area),

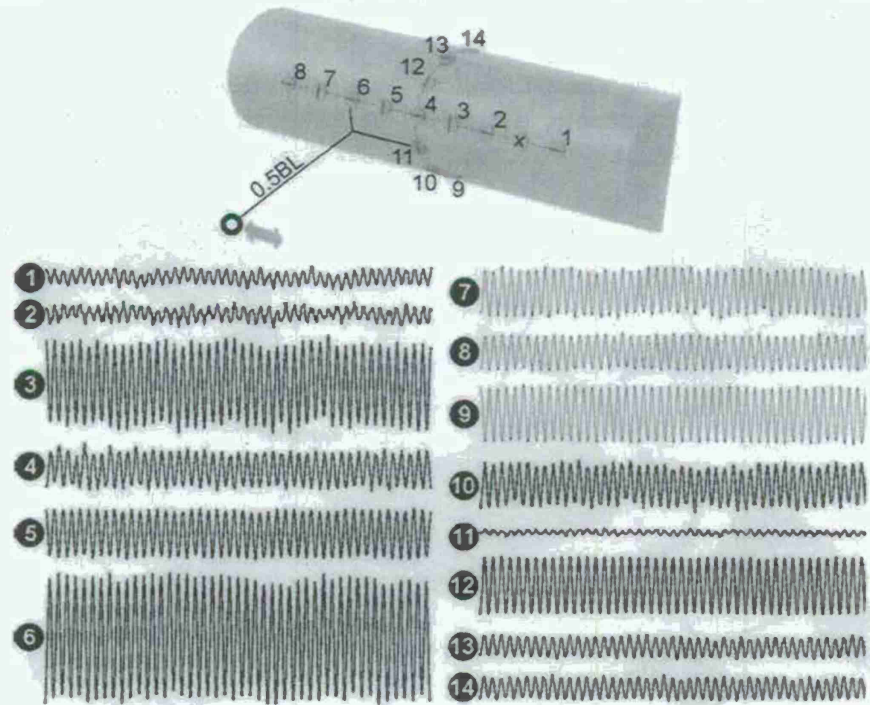


Figure 3: Typical ALL response under hydrodynamic stimulus.

demonstrating a sharp sensitivity of the ALL to the dipole location in the near field. The maximum deviation of the predicted locations to the corresponding real location is only $0.13BL$. Furthermore, the original 5-D search results (with only extracted 3-D results presented in Figure 4) indicate that the dipole orientation can also be accurately predicted to within 10° for these cases.

For dipole localization, the general interest is to determine the dipole location (3-D) rather than the full dipole state (5-D, location plus orientation). However, the 5-D search strategy embedded in the algorithm is critical to ensure satisfactory 3-D localization. This is due to the fact that the ALL-encoded spatial excitation patterns are unique to both the dipole location and orientation. To make

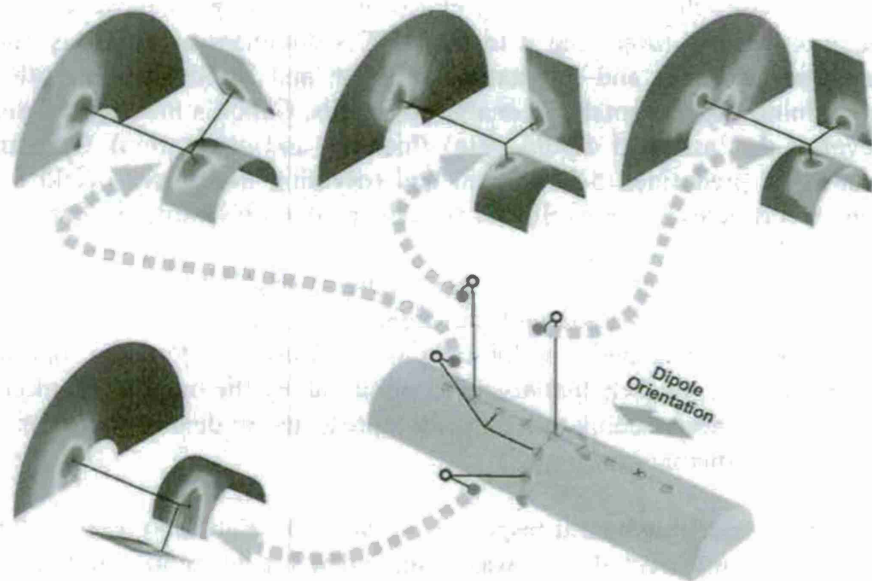


Figure 4: Effect of dipole location on localization.

the pattern-recognition-based localization algorithm work, such uniqueness is indispensable. As an advantageous outcome, the algorithm becomes orientation-tolerant for 3-D localization, simply because the unknown orientation has been accounted for, but is not reflected in, the 3-D

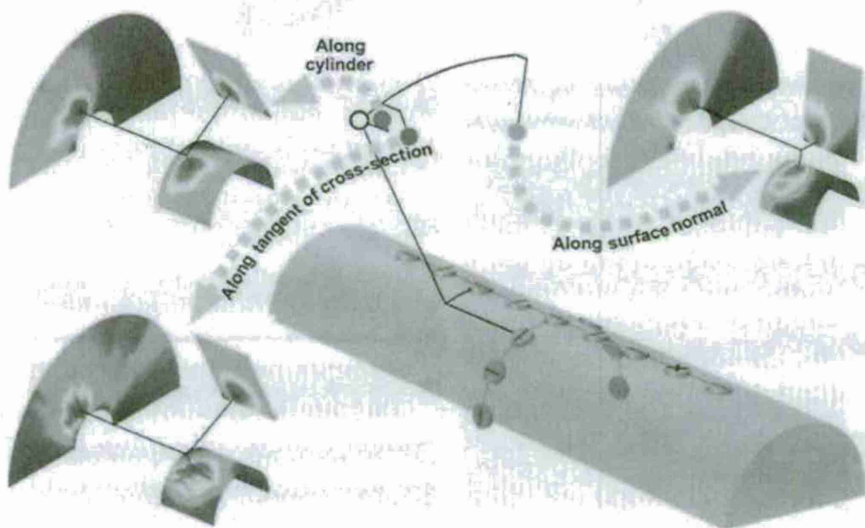


Figure 5: Effect of dipole orientation on localization.

localization. To test this orientation tolerancy, we placed the dipole source at a fixed location ($0.5BL$ to the cylinder surface) but varied the dipole orientation in three orthogonal directions (Figure 5). These tests show that all the localizations are successful despite of the large variations in orientation, although in some orientation the deviation is relatively

large ($0.3BL$).

Hydrodynamic stimuli generated by animals in real aquatic environments are much more complex than idealized dipole flows, though many are dipole-dominant. To further explore the localization performance of the algorithm-implemented ALL in the real-world environment, a tail-flicking crayfish was employed to generate a hydrodynamic stimulus near to the ALL (Figure 6A). The signal picked up by a BN near the flicking tail demonstrates a pulsed pattern (Figure 6B), which is indeed different from sinusoidal patterns usually obtained from dipole field measurement (Figure 3). Yet, by applying the same beamforming algorithm used in dipole localization, sharp localization results are still achieved (Figure 6C). With the flicking tail of the crayfish located at a distance of approximately $0.2BL$ (the location estimate is approximate due to the tail motion and slight movement of the crayfish), the predicted location is within $0.1BL$ from that point. During localization, the algorithm automatically identifies the dominant tail-flicking frequency; that enables the algorithm to tune to the frequency of interest for band-pass filtering. A biological observation evidences that, when necessary, a fish can shorten the sensing time so that it can react to the stimulus quickly. To mimic this rather dynamic localization capability, a 10-second record from the ALL, which has been used for crayfish localization in the foregoing (Figure 4), was reprocessed. The record was divided into a series of 100-millisecond segments with an overlap of 67 milliseconds between segments. Using the same algorithm as before, localization results were generated for each segment and were animated for the whole series. In the animation (not provided), the dynamic tail-flicking event has been successfully captured and visualized over time. During the experiment the crayfish, which was tethered to a wooden rod held by a human hand, was slightly moved. This subtle displacement is also reflected in the animation.

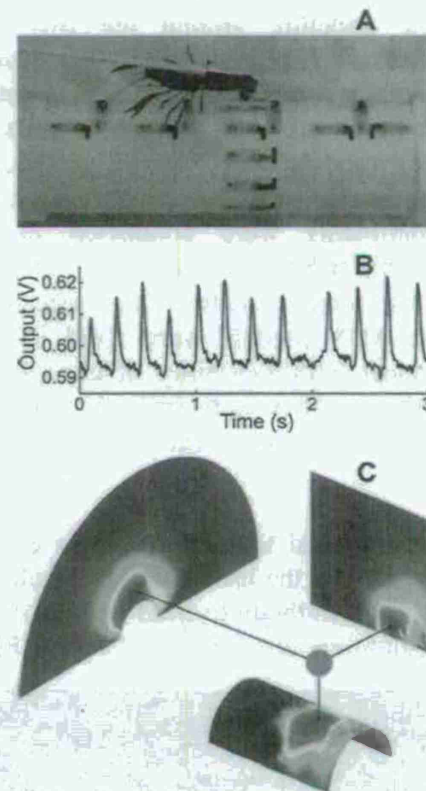


Figure 6: Crayfish localization.

ALL-enabled station keeping

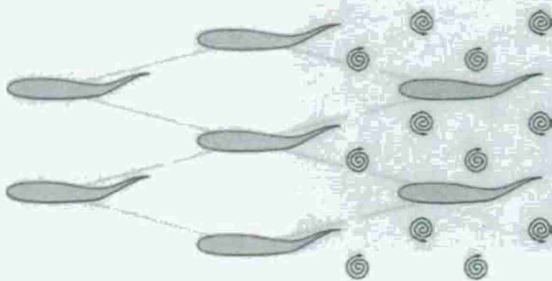


Figure 7: Fish schooling.

When fish school in certain formation, the leading ones generate well-organized vortices by undulating their bodies (Figure 7). Then through lateral line sensing to identify these vortices, the trailing fish undulate their bodies in between the vortices. Or in other words, the trailing fish ride the vortices generated by the leading ones. In doing so, fish can synchronize their swimming. And, they can reduce energy consumption.

The ALL-enabled station keeping was inspired by fish schooling – like fish using lateral line for schooling, we use ALL for station keeping. In this biomimetic approach, two AUV models were employed, where the following one was instrumented with ALL. Yet, station keeping between teamed-up AUVs differs from fish schooling. The AUVs have rigid bodies, and the hydrodynamic disturbances generated by the moving AUVs are much weaker and less organized than that generated by swimming fish with similar sizes.

To realize the station keeping of AUVs using ALL sensing, an in-depth understanding of the flow structure around the two AUVs is essential. A quantitative flow visualization technique - particle image velocimetry (PIV), has been employed for this purpose. The two AUV models were made of acrylic, with one twice as large as the other (Figure 8A). The experiments were conducted in a water channel at Reynolds number of 20,000 (based on the beam diameter of the large AUV). The two AUV models were fixed in the water channel with flexibility of changing relative positions. They were optically transparent and allowed the laser sheet to go through (Figure 8B).

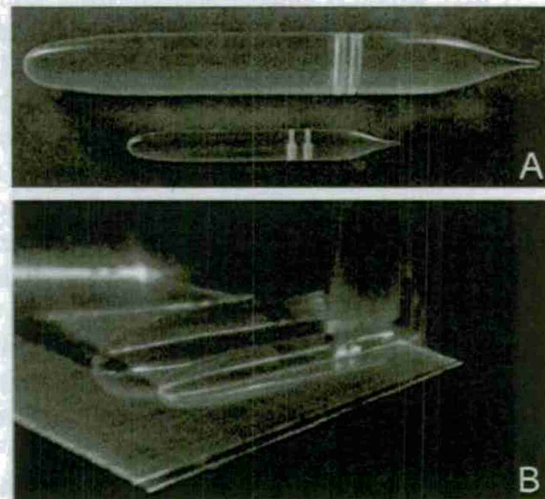


Figure 8: *A*, AUV models. *B*, AUV models in water with laser sheet going through.

Three typical teaming positions of the AUVs have been explored using PIV. With the large model to be the leader and the small one to be the follower, the three teaming positions are head-to-head, midbody-to-head and tail-to head, respectively. And for each case, relative lateral and longitudinal distances were varied. PIV results for the trailing case are presented in Figure 9. The

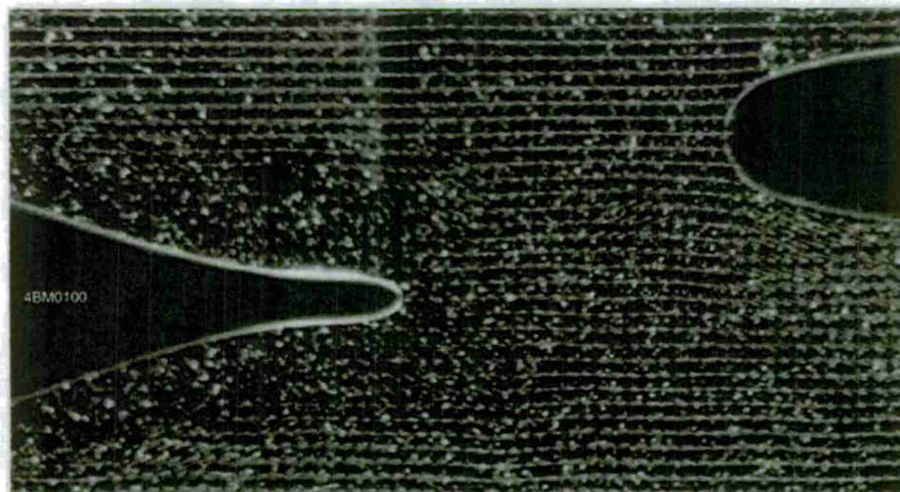


Figure 9: PIV results showing instantaneous flow structure between the two AUVs in tail-to-head teaming position with an offset.

two AUVs are in parallel, but with an offset between the centerlines. It is evident that strong flow separation has occurred in the tail area of the leader. The formed unsteady wake flow then impinges upon, and interacts with, the nose of the follower. Statistic analysis of time-resolved

PIV results indicate that for this specific teaming position, the centerline of the follower is roughly aligned with the edge of the leader-generated turbulent wake. Therefore strong asymmetric flow occurs on the two sides of the follower, which will be further discussed later.

In addition to understanding the flow structures in station keeping, the performance of the AHCs has also been validated by means of PIV. As shown in Figure 10A, an AHC has been mounted to the follower, and the sensor measurement was synchronized with PIV. The red dot in Figure 10A indicates the position of a sensing hair. Figs. 10B and 10C compare a sensor signal with PIV results. The red curve (Figure 10B) shows the time trace of the sensor output, and the blue curve (Figure 10C) is the extracted time trace from high-speed PIV at a position close to the hair. Overall, the two plots resemble each other in general waveforms and in spectrum patterns (not provided). Yet, the plots do not match exactly. This is due to the complexity of the local turbulent flow and the relatively poor spatial resolution of the PIV. In general, the AHC functioned reasonably well in this flow-sensing scenario.

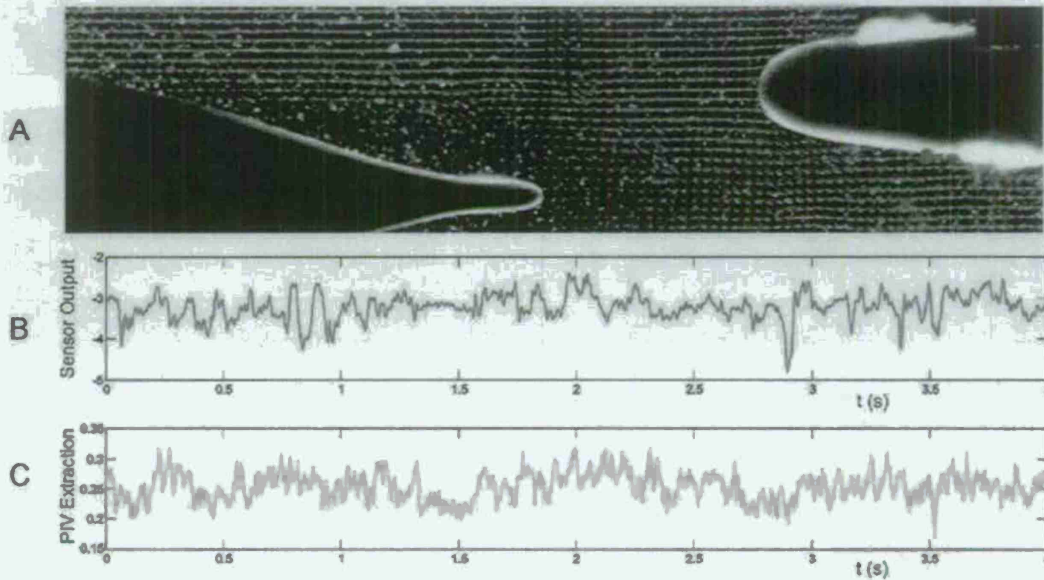


Figure 10: *A*, PIV synchronized with AHC measurement. *B*, AHC signal. *C*, Extracted time trace of the horizontal velocity component near to the position of the AHC's sensing hair.

The ALL-enabled station keeping was eventually realized in a towing tank. Two new AUV models (Figure 11A), with one twice as large as the other, were fixed to a towing carriage over the tank. They both can be towed at the same speed, but each of them has one-degree-of-freedom so that they can change their lateral positions independently. The whole towing system is motorized and computer controlled. Note that the follower (the small AUV) has metal ridges attached to its two sides. The ridges serve as the AHC holder and cable cover, and the integrated sensing platform forms the ALL for station keeping. Figure 11B provides more details on the sensor integration to a metal ridge. Limited to the availability of AHCs, 7 AHCs were integrated to the two ridges, with 4 on one and 3 on the other. The AHC distribution was illustrated by the diagram in the middle of Figure 11C.

For station keeping, we first examined the head-to-head teaming position as shown in the middle diagram of Figure 11C. By towing the two models together, individual AHCs from the ALL would respond differently, with typical signal pattern as illustrated in Figure 11C. The corresponding towing speed associated with the AHC signals is like this – staying still, speeding up, maintaining constant speed, and slowing down. After some preliminary investigation, we found that one parameter can best represent the ALL responses for station keeping, which is the difference of turbulence intensities $\Delta(\text{rms}/\text{mean})$ measured by each sensor pair at the same longitudinal positions but on the two opposite sides of the AUV model.

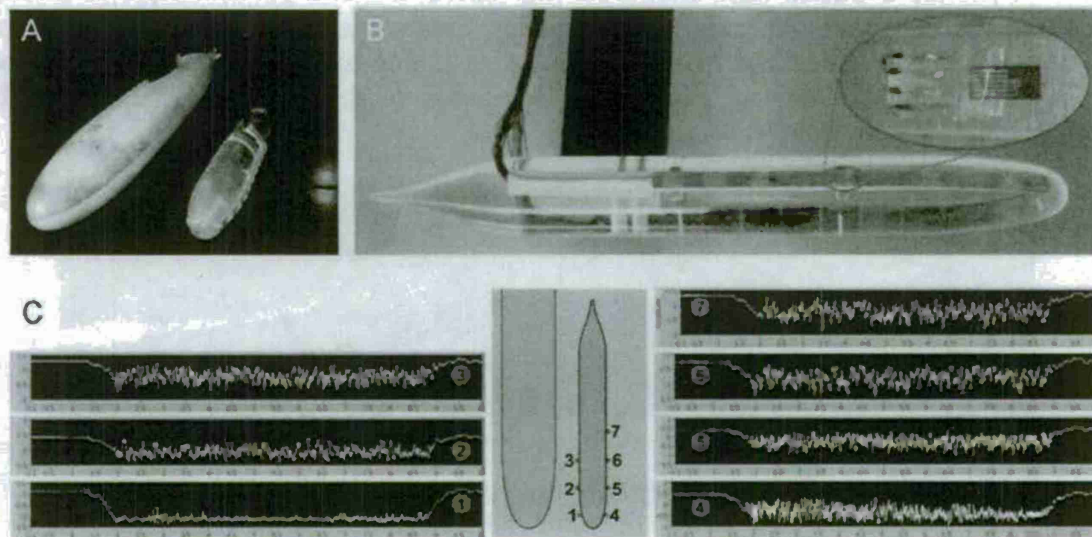


Figure 11: A, AUV models for station keeping in the towing tank. B, ALL on the follower, with close-up showing AHC integration. C, Typical ALL response during station keeping.

Using $\Delta(\text{rms}/\text{mean})$ as a measure, ALL responses for the head-to-head case were obtained at various towing speeds and gaps. Figure 12 shows the results at a fixed towing speed ($Re = 55,000$, based on the beam diameter of the leading AUV). It is evident that when the gap changes, the lateral line response pattern changes accordingly. This implies that the lateral line can tell whether or not the follower is keeping up with the leader. In other

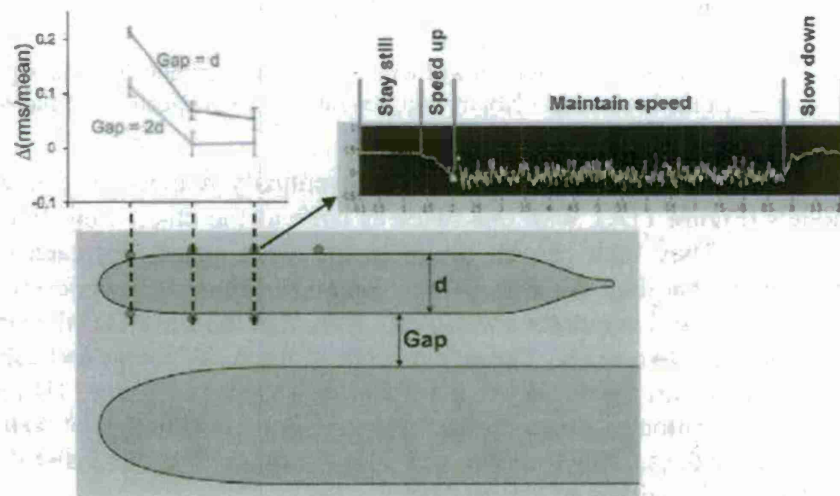


Figure 12: Lateral line responses with varying gaps.

words, at this teaming position, we can surely do controlled station keeping based on ALL sensing.

The second station-keeping position we explored is the trailing case – tail-to-head. Both AUVs were again towed at the same speed. The tail-to-head distance was fixed, which is $3.5d$ (Figure 13A). But we varied the offset systematically to see how the lateral line responses. For this case, we only used one pair of AHCs near the nose on the follower. Figure 13B shows the ALL responses in terms of $\Delta(\text{rms}/\text{mean})$ versus the offset. The experiments were repeated five times. The averaged results and corresponding error bars are presented. The plot clearly demonstrates a relatively sharp peak at the offset of $0.5d$, which is a distinctive feature we can use for autonomous station keeping. For comprehensive understanding of this trend, numerical simulation was conducted under the same flow conditions. This part of work was done in collaboration with co-PI Joseph Humphrey at the University of Virginia. Figures 13C and 13D are sectional views of the turbulent kinetic energy from CFD at a specified longitudinal position (red straight dashed line) for two different values of the offset. It is intuitive that when the offset is large, e.g., Figure 13D for $1.8d$, the leader-generated turbulent wake is relatively far aside from the follower. Therefore, the two sensors are picking up nearly the same turbulence intensity, which yields very low difference. With a decreasing offset, e.g., Figure 13C for $0.83d$, the leader-generated turbulent wake swipes over the follower from one side while the other side remains out of the wake. Accordingly, the resulting difference from the two sensors will be large. With a further decreasing offset, e.g., the extreme case of no offset, both AHCs would pick up strong but nearly the same turbulent intensity since they are both inside the wake and at symmetrical positions with respect to the center of the wake.

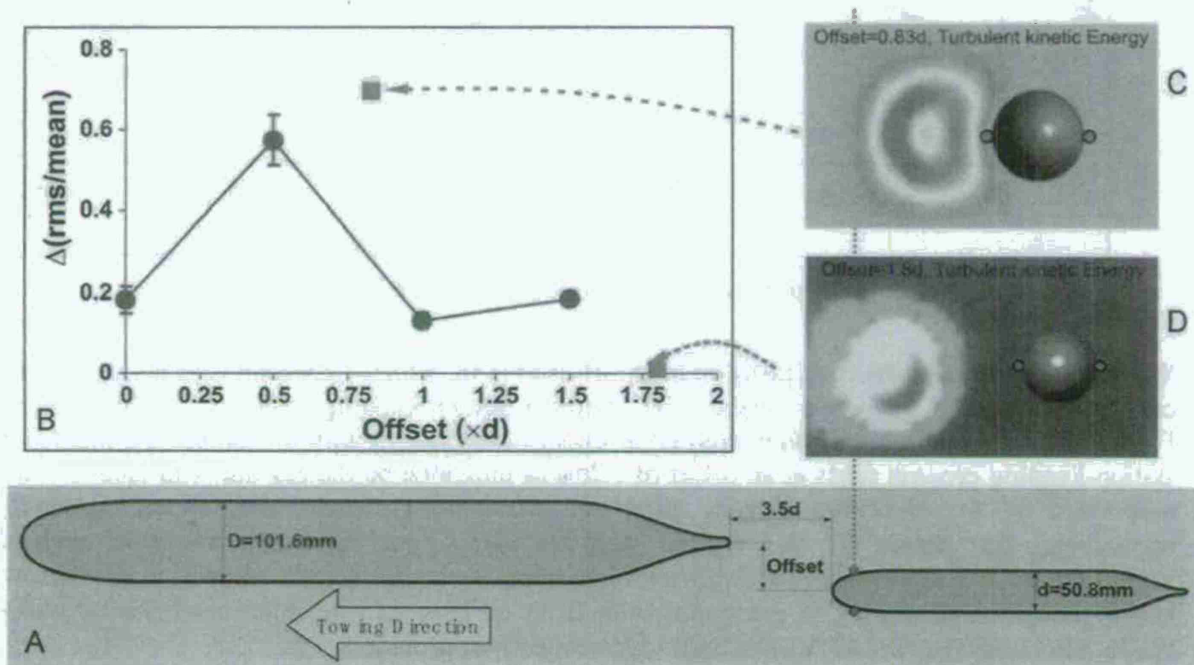


Figure 13: *A*, Diagram showing station keeping for tail-to-head case. *B*, experimental results of difference of turbulent intensity with varying offset. *C*, sectional view of turbulent kinetic energy from CFD at an offset of $0.83d$. *D*, sectional view of turbulent kinetic energy from CFD at an offset of $1.8d$.

Using Figure 13B as a station calibration chart, we have realized autonomous station keeping for the trailing case. Figure 14A illustrates the control algorithm we developed. The station keeping is a step-by-step process. In each step, the two AHCs pick up some signals. The signals are evaluated in terms of turbulence intensity rms/mean, and then the difference $\Delta(\text{rms/mean})$ is derived. By comparing this value with the calibration chart, decision can be made on which direction the follower should move to. The computer-controlled stage then brings the follower to the next position, and a new step starts again by repeating the same process. Through this kind of step-by-step iteration, the follower eventually approaches a desired station-keeping position.

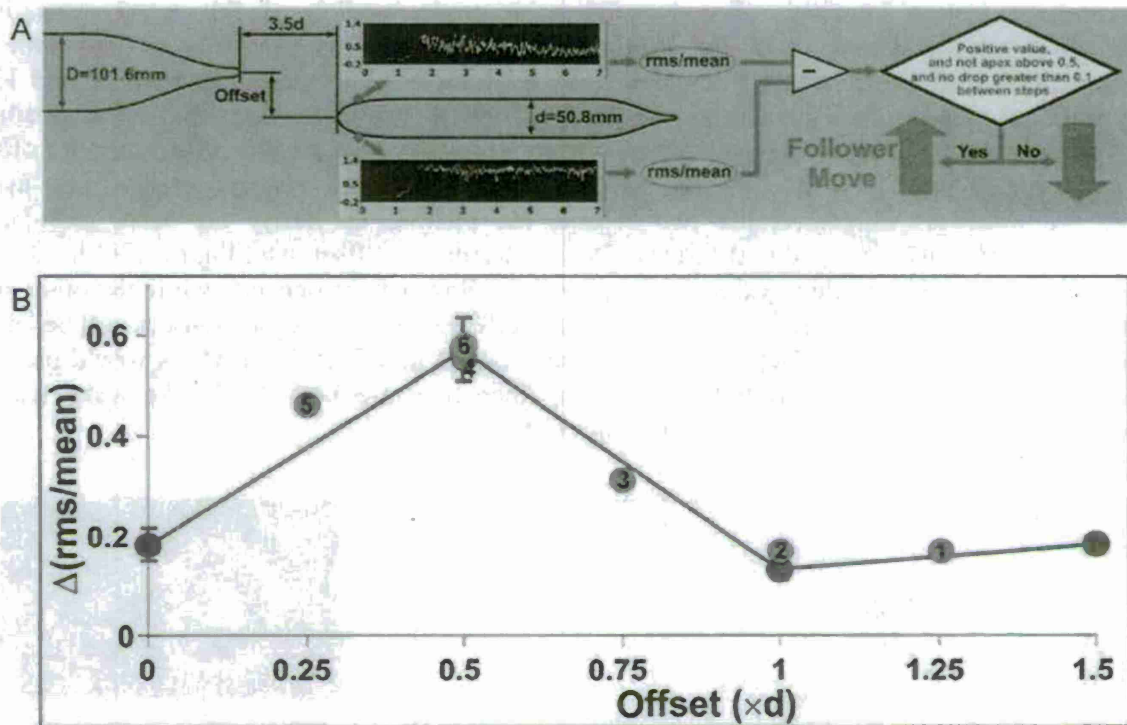


Figure 14: A, station-keeping algorithm. B, station-keeping approach.

With an aimed station-keeping position at an offset of $0.5d$, which corresponds to the peak of the calibration chart as shown in Figure 13B, detailed station-keeping approach is illustrated in Figure 14B by a sequence of numbered color dots in comparison with the calibration chart. The station-keeping process starts at an offset of $1.25d$ as indicated by the red dot with label 1. Then automated by the algorithm (Figure 14A) and the control system, the follower gradually approaches, and passes by, the desired station-keeping position. Being aware of such an overshoot by the algorithm, the follower then turns back and finally maintains the station-keeping position as shown in green dot with label 6. This ALL-enabled autonomous station keeping between the two AUVs has been video-typed (not provided).

Canalled artificial haircell sensor

Fish have two types of neuromasts in their lateral line system – superficial neuromasts and canalled neuromasts. The AHCs discussed in the foregoing were inspired by superficial neuromasts, which are distributed on the skin surface. In contrast, canalled neuromasts are situated in a protective canal (Figure 15A). There are open pores along the canal that allow water exchange with the surrounding. In fact, the canal flow is driven by the pressure difference between the neighboring pores, which is resulted by the surrounding flow outside of the canal. Biological studies indicate that canalled neuromasts are superior to superficial neuromasts in some perspectives. To name a few, the canal (i) functions as a band-pass mechanical filter, (ii) increases the signal-to-noise ratio, and (iii) provides physical protection to the neuromasts.

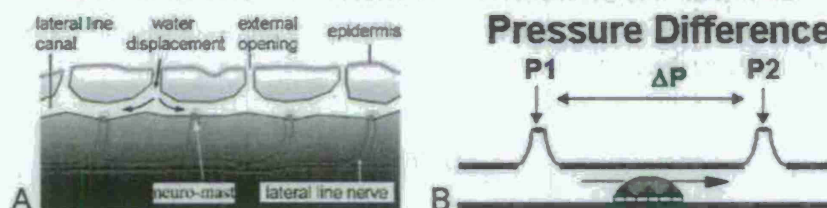


Figure 15: *A*, schematic illustrating neuromasts in a canal. *B*, the flow inside the canal communicates with local flow around the fish via pores.

By learning from the anatomic structure and the functionality of the canalled neuromast in fish, we developed canalled AHCs. Microfabricated AHCs, which have been discussed in the foregoing, was chosen for this purpose (Figure 16A). An array of AHCs were flush-mounted in the milled slots on the printed circuit board (PCB) first, with the sensing directions of individual AHCs all along the array (Figure 16B). The canal structure was fabricated using stereolithography technique to ensure the accuracy. It was manually assembled to the AHC array and held down by super glue. The AHCs were then wire-bonded to the PCB to achieve electrical connection to the outside circuitry. After encapsulating the wire-bonds with Epoxy, the whole canaled AHC structure was planarized using PDMS to form a hydrodynamically favorable

smooth front surface (Figure 16C). This prototype canal structure was nearly a scaled-up version of a fish lateral line canal. The canal is of a semi-cylindrical shape of diameter 4mm. The pores were evenly distributed with a spacing of 5mm, which matches with the AHC spacing. The round opening of an individual pore is of diameter 0.8mm.

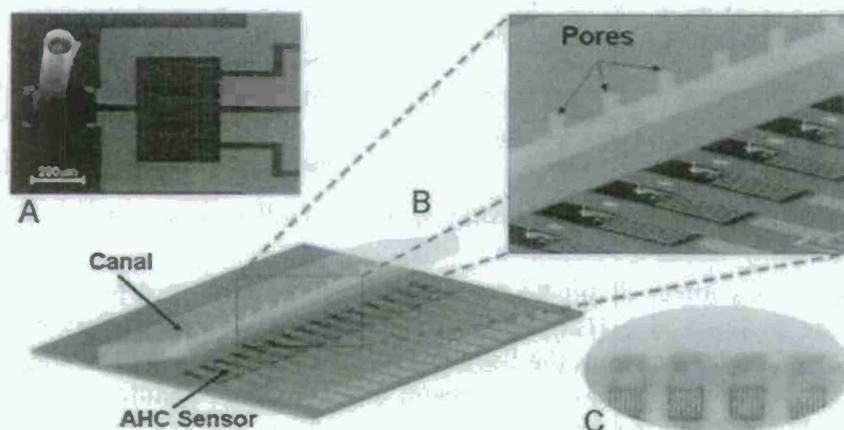


Figure 16: *A*, Scanning electron micrograph of an AHC. *B*, Diagram illustrating the structural detail of the canalled AHCs.

To better understand the canal flow, efforts have been made from the analytic perspective. Motion of water outside canal is first transferred into canal fluid motion before a haircell sensor is excited. Fish canal neuromasts are commonly described as detectors of outside water acceleration. Therefore it is useful to express the fluid velocity inside the canal in response to acceleration of water outside the canal. Assume that the outside fluid motion causes a pressure gradient across the pores (Figure 15B), the pressure gradient corresponds to water acceleration A via $dp/dx = -\rho A$, where ρ is the density of water. A periodic outside water acceleration can be expressed as $A(t) = A_0 e^{i\omega t}$, where A_0 is the amplitude. The pressure-driven oscillatory laminar flow inside a tube has been solved analytically by other researchers. Inside a canal of radius R , at a distance r from the canal axis, the velocity of an oscillating fluid with frequency f and viscosity μ can be described as:

$$u(r, f) = A_0 e^{i\omega t} \frac{-i}{2\pi f} \left[1 - \frac{J_0\left(\sqrt{-2i} \frac{r}{\delta}\right)}{J_0\left(\sqrt{-2i} \frac{R}{\delta}\right)} \right], \quad (1)$$

where J_0 is the Bessel function of the first kind, order zero, and δ is the boundary layer thickness inside the canal, $\delta = \sqrt{\mu / (\rho \pi f)}$. The velocity profiles are frequency dependent. Shown in Figure 17 are some examples of the circular-symmetric velocity profile across the cross-section of a circular canal. Snap shots of the profile are taken at several moments during a cycle. The radius R is equal to the equivalent hydraulic radius of the present prototype canal. The fluid inside the canal is water. The acceleration amplitude A_0 is arbitrarily chosen to be 1 m/s^2 , corresponds to 10^3 Pa/m pressure gradient amplitude in water. It is kept constant for different frequencies.

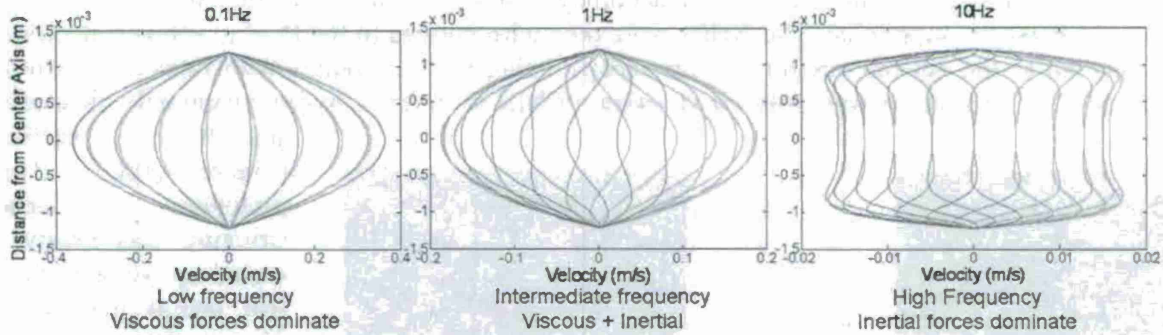


Figure 17: Velocity profile inside the canal under oscillatory pressure gradient at different frequencies.

At low frequencies ($\sim 0.1 \text{ Hz}$), viscous forces dominate resulting in a fully developed parabolic velocity profile. At intermediate frequencies ($\sim 1 \text{ Hz}$), both viscous and inertial forces affect the profile. The resulting profile starts to deviate from the fully developed parabolic shape. At high frequencies ($\sim 10 \text{ Hz}$), the fluid inertial force becomes dominant and causes an annular profile with a flattened center section. The apex no longer reaches the center of the canal but happens at a distance of about 2.3δ away from the wall of the canal.

The dimensionless parameter governing such a flow is given by $2\pi f R^2 / \nu$, where $\nu \equiv \mu / \rho$ is the kinematic viscosity of the fluid. When $2\pi f R^2 / \nu < 4$, the flow is considered viscous force

dominated; when $2\pi f R^2/\nu > 4$, it is considered inertial force dominated. The centerline velocity magnitude vs. frequency is plotted in Figure 18. The magnitude is constant as low frequency and drops off quickly at high frequency. It can be viewed as a first order low-pass filter with respect to constant outside fluid acceleration/pressure gradient ($dp/dx = -\rho A$). The corner frequency is estimated to be $f_0 \approx 4\nu/2\pi R^2$, which is essentially the border condition between viscous force dominated flow and inertial force dominated flow defined by the dimensionless parameter $2\pi f R^2/\nu$. The corner frequency of the prototype canal is calculated to be 0.4Hz.

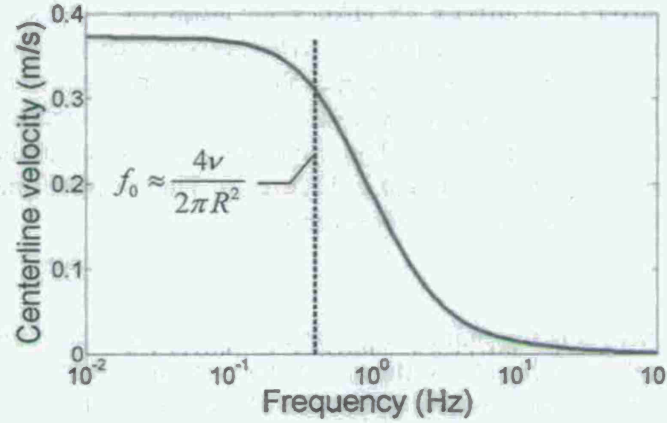


Figure 18: Centerline velocity inside the canal under oscillatory flow with constant pressure gradient amplitude.

In the presence of an AHC inside the canal, however, the AHC response with frequency does not follow the trend presented in Figure 18. The change is caused by the flow interaction with the sensing hair. Under oscillating boundary layer flow conditions, the governing equation of the hair's angular motion is the conservation of angular momentum:

$$(I + I_\rho + I_\mu)\ddot{\theta} + (R + R_\mu)\dot{\theta} + S\theta = 4\pi\mu G \int_0^L V_F y dy + \left(\frac{\pi\rho d^2}{4} - \frac{\pi^2\mu G}{g\bar{w}} \right) \int_0^L \dot{V}_F y dy, \quad (2)$$

where I is the moment of inertia of the hair, I_ρ and I_μ are additional contribution to the moment of inertia associated with water density and viscosity, R_μ is the damping constant due to water viscosity, S is the torsional restoring constant of the silicon cantilever beam, and G is a quantity that can be calculated from physical parameters of the hair, water, and far field flow waveform. Specific calculations regarding the AHC sensor can be found in our earlier work. The only unknowns in the equation are V_F and \dot{V}_F . With

an AHC inside a canal, V_F is essentially the velocity profile inside the canal caused by oscillatory pressure gradient introduced in the foregoing. Using MATLAB, the velocity profile and its time derivative can be calculated and integrated over the length of the hair at any given instant. As a numerical experiment, acceleration amplitude was again arbitrarily chosen to be 1m/s^2 (10^3Pa/m pressure gradient amplitude). Results were then plugged into MATLAB ordinary differential equation (ODE) solver to solve the equation for the angular displacement θ .

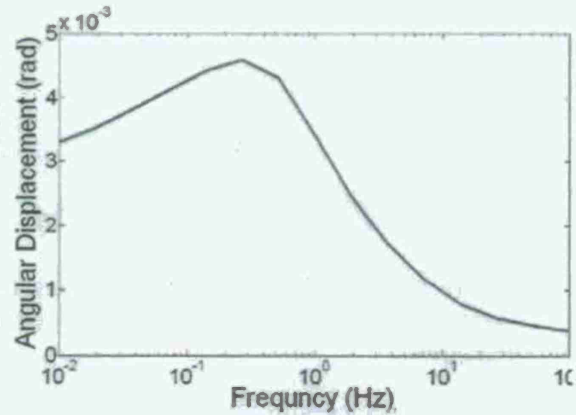


Figure 19: Simulated AHC response inside a canal under oscillating flow conditions.

The numerical result of the steady-state angular displacement amplitude vs. frequency is presented in Figure 19. The result suggests a band-pass characteristic with a peak at 0.4Hz. Below the peak frequency, AHC response decreases gradually. Above the peak frequency, it drops at a much steeper slope. Yet, this drop rate is much milder comparing that in Figure 18. To verify the simulation result, a canal AHC was tested under oscillatory pressure gradient at different frequencies. The oscillatory pressure gradient is generated by a dipole source as schematically illustrated in Figure 20. The pressure amplitude generated by a vibrating sphere in plane of vibration axis is given by:

$$p(r, \theta) = -\frac{\rho a^3 \cos \theta}{2r^2} A_0 \sin(\omega t), \quad (3)$$

where a is the radius of the sphere, r is the distance away from the center of the dipole, θ is the angle with respect to the axis of the vibration, and A_0 is the acceleration amplitude of the sphere. Normalized pressure amplitude along the canal is superimposed on top of the canal AHC array as shown in Figure 20. With focus on the two pores marked as P1 and P2, the distance between the two pores is $\Delta x = 24\text{mm}$, and the dipole source is right above the pore P1 at a distance of $r = 11.35\text{mm}$ (measured from the center of the sphere to the top of the canal). The radius of the sphere is $a = 6.35\text{mm}$. With some approximation, the pressure gradient amplitude can be finally determined by

$$\frac{p_1 - p_2}{\Delta x} = -\frac{\rho a^3}{2r^2 \Delta x} A_0 \sin(\omega t). \quad (4)$$

The dipole frequency was swept from 0.4Hz up to 95Hz and the dipole acceleration was monitored by an accelerometer attached to the shaker. Pressure gradient amplitudes were then calculated using equation (4) based on the accelerometer reading. By maintaining nearly constant pressure gradient amplitude during the frequency sweep, the experimental results are as presented in Figure 20B. Indeed a band-pass characteristic of the canal AHC is demonstrated. The experimental results show a peak frequency at 0.6Hz, which is slightly higher than the simulation result (0.4Hz).

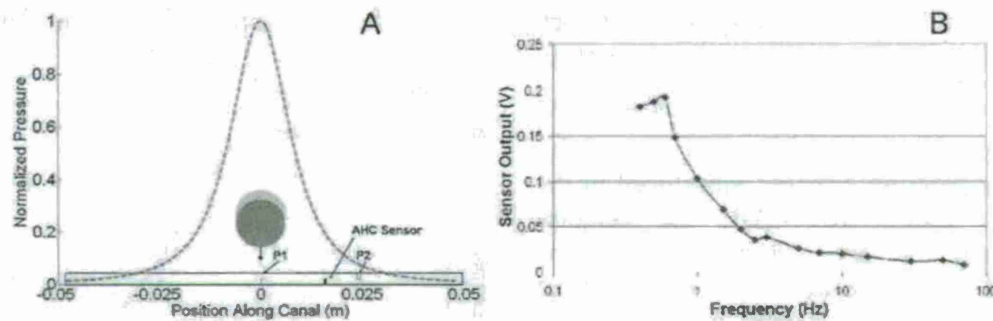


Figure 20: *A*, diagram illustrating canal AHC, dipole source, and pressure profile along the canal. *B*, response of canal AHC with frequency under constant pressure gradient amplitude.

Following the successful demonstration of the band-pass function of the canal AHC, we examined another capability enabled by the canal structure – reduction of background noise from the hydrodynamic environment. In doing so, both a superficial AHC and a canal AHC were

employed for comparative experiments in a water channel (Figure 21). A dipole field was also superimposed to the channel flow by setting up a vibrating sphere in running water. The sphere vibrating frequency was fixed at 20Hz. During the experiments the two types of AHCs were placed close to each other as shown in the bottom-right picture of Figure 21. The support/holder of the AHCs strongly interacted with the channel flow, and the induced turbulent noise level increased with increasing inflow velocity. Four inflow velocities in presence of the dipole field were examined – no flow, low speed (0.04m/s), medium speed (0.08m/s), and high speed (0.12m/s).

Figure 22 shows spectra of signals from the two AHCs. In still water with dipole field only, the superficial AHC presents stronger peak at dipole frequency than the canal AHC; this is due to the sensitivity difference rather than the structural difference (canal) of the sensors. As the inflow velocity increases, the superficial sensor becomes increasingly noisy, especially in the low frequency regime. On the other hand, the canal AHC is barely affected by the background turbulent noise. Due to the flow interaction with the

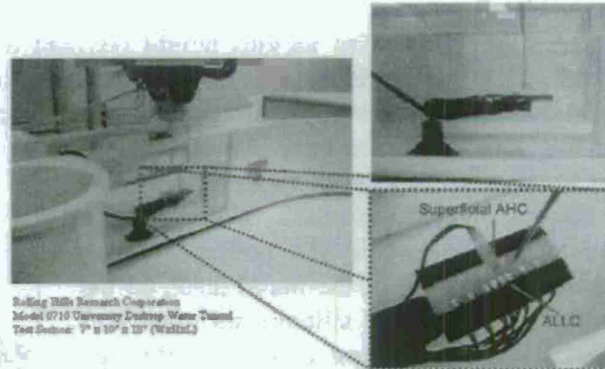


Figure 21: Setup of running water comparative experiments.

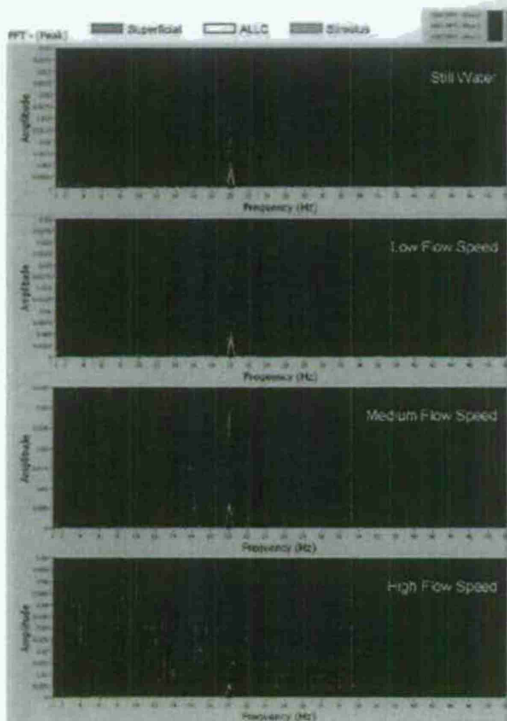


Figure 22: Spectral comparison between superficial and canal AHCs at various inflow velocities.

AHC holder, the flow field near to the AHCs was filled with small-scale vortices. The superficial AHC was more susceptible to such small-scale vortices due to its micrometer size scale. The small-scale vortices would not, however, cause any appreciable pressure difference across the pores of the canal since the distance between the pores is generally larger than the scale of the vortices. Eventually, the superficial sensor becomes overwhelmed by the low frequency noise and renders incapable to detect the 20Hz stimulus while the canal sensor performs just as well.

The result of this comparative experiment has directly demonstrated the advantage of using canal AHCs over superficial AHCs in noisy environment. In real life conditions, the noise level is likely to be much stronger, e.g., in river flows; the benefit of having a canal sensor will become more beneficial. Just like the superficial and canal neuromasts of a fish, the two kinds of sensors will go under different subdivisions of labor – superficial AHCs for flow velocity and direction sensing and canal AHCs for flow sensing with featured frequencies in noisy environments.

Characterization of AHC under turbulent flow conditions

Inspired by superficial neuromasts of fish, a superficial AHC possesses a sensing hair sitting on a flat surface – the substrate. This structure of AHC is especially advantageous for boundary layer flow sensing of various underwater water vehicles, just like its biological counterpart does. Due to the fact that most underwater vehicles create turbulent boundary layer flow under normal working conditions, systematical characterization of the AHC performance under turbulent boundary layer flow conditions is of great importance for potential applications.

A series of AHCs with various height (H) and diameter (D) of the hair, as well as the beam length (L) were fabricated for characterization purpose (Figure 23A). To create a hydrodynamically favorable frontal surface of the AHC, which is a smooth surface with the sensing hair to be the only protrusion into the local boundary layer flow, new sensor packaging and mounting schemes have been developed. To enable the new packaging scheme, the layout of the metal leads on the frontal surface of the silicone substrate was specially designed, and associated through holes for electric connection were also made (Figure 23B). The detailed sensor packaging scheme is illustrated in Figure 23C. The major steps are summarized in the following: (i) prepare PCB (no copper layer) with a set of grouped through holes for arrayed sensors and with each group of holes exactly matching with the through holes on an individual sensor chip; (ii) strip one end of a wire having solid metal core of diameter smaller than the through holes on the PCB, and assure the striped length equal to the thickness of the PCB-chip assembly; (iii) put the stripped end of the wire fully into a PCB hole, and then glue them together using epoxy from the bottom side (Figure 23C, close-up); (iv) with all the wires glued to the PCB, place a sensor chip on top of the PCB, and let the protruded metal cores of the wires on the PCB fit in the through holes on the chip; (v) glue the chip to the PCB using superglue; (vi) apply silver paste to the circular areas on top of the chip to establish the electric connections between the sensor chip and the wires; and (vii) parylene-coat the packed sensor for water-proofing.

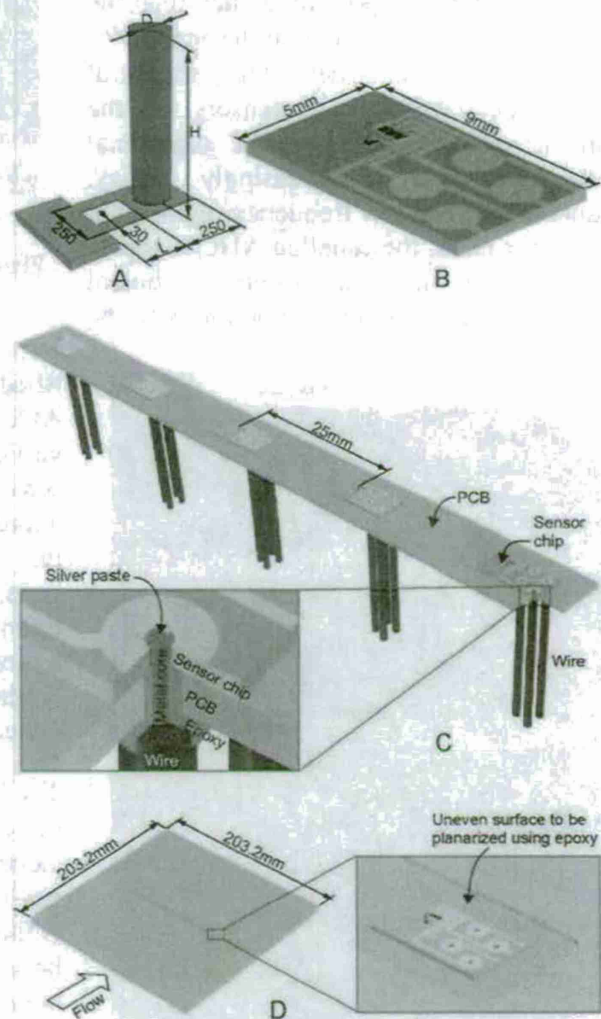


Figure 23: A, sensor dimensions (in μm). B, sensor chip with metal leads for electrical connection. C, sensor packaging scheme. D, sensor mounting to a testing plate.

With an array of five sensors packaged to a PCB in a shape of a stripe (Figure 23C), the sensor array was then integrated to a test plate for experimental study (Figure 23D). The plate is a part of the bottom wall of a water tunnel that can generate turbulent shear flow. A slot of a T-shape cross section was made in the middle of the plate. The slot allows flush-mount of the sensor array to the frontal surface of the plate – the inner wall of the water tunnel, and the sensor wires can come out from the backside – the outer wall of the tunnel. The close-up in Figure 23D shows the frontal surface of the sensor array-plate assembly. Obviously, the sensor chip forms an island in the slotted area of the plate, although the top surface of the sensor chip is at the same elevation with the surface of the plate. To planarize the uneven surface, epoxy glue was applied to fill up the sunken area. The epoxy also serves to seal the assembly from leaking.

The experiments were conducted in the Applied University Research, Inc. water tunnel located in Radford, Virginia. The test section (Figure 24A) is a constant height channel of dimensions 244cm (L) \times 24cm (W) \times 5.1cm (H). The sensor array on the test plate was located 213.4cm downstream of the test section entrance. The tunnel is capable of generating fully developed turbulent shear flows at various Reynolds numbers. Five Reynolds numbers, based upon the channel bulk flow and the hydraulic diameter, in the range of 10 000 to 200 000 were explored for sensor characterization.

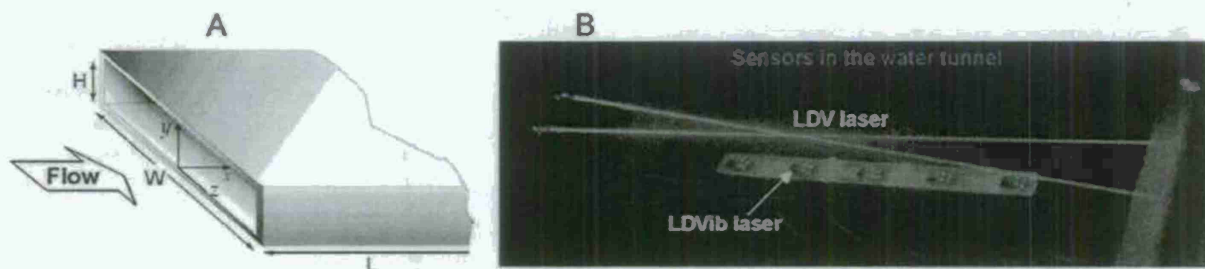


Figure 24: *A*, schematic illustrating the test section of the water tunnel. *B*, picture showing the experimental instrumentation inside the test section.

With each Reynolds number explored, the turbulent velocity statistics and time-dependent signature were measured using a single-component laser-Doppler velocimeter (LDV). As illustrated in Figure 24B, the haircell sensors were flush-mounted to the floor of the channel, where as the two crossing laser beams (in green) were from LDV. In order to directly compare LDV results with sensor responses, data acquisition for both LDV and sensors were synchronized. The cross-point of the laser beams were located either 5mm upstream or 5mm downstream of the hair of a specified sensor at various elevations. Another means of measurement – laser-Doppler vibrometer (LDVib), was also employed to characterize the hair vibration under turbulent flows. This measurement requires the laser beam to directly shine on the tiny hair (Figure 24B, red dot) that sits on top of a doped silicon cantilever (Figure 23A). As the sensing element of a haircell sensor to flows, the doped silicon cantilever is also sensitive to lighting conditions. For this reason, the LDVib measurements were conducted separately from sensor measurements.

A total of 15 sensors were prepared for experiments. They covered a variation of parameters D , H , and L , which are defined in Figure 23A. Due to accidental damage, only two sensors were eventually tested in the AUR water tunnel. In this report discuss focuses on one sensor performance only. For this specific sensor tested, the hair is of diameter $D = 80\mu\text{m}$, height $H = 650\mu\text{m}$, and the cantilever beam is of length $L = 200\mu\text{m}$.

The turbulent boundary layer profiles were first obtained using LDV. The mean stream-wise velocity profiles measured for five Reynolds numbers are plotted in Figure 25A using viscous wall scaling and compared to Spalding's continuous law of the wall (1961). In order to determine the friction velocity, LDV mean velocity data from the logarithmic region of the velocity profile were fit to the log law equation: $U^+ = \frac{1}{\kappa} \ln y^+ + B$, where $\kappa = 0.41$ is the von Kármán constant and $B = 5.2$ is another empirical constant. A typical dimensional near-wall approach flow profile at $Re = 200,000$ was provided in Figure 25B. The mean and RMS measurements were obtained within about $200\mu\text{m}$ from the facility wall. In this figure, the scale of the mean and turbulence flow structure relative to the haircell is depicted by plotting the haircell along the profile y -direction axis (ordinate of the plots). For different Reynolds numbers, the near wall gradients of the mean and RMS velocities successively increase near the wall with increasing Reynolds number as the viscous length decreases with Reynolds number.

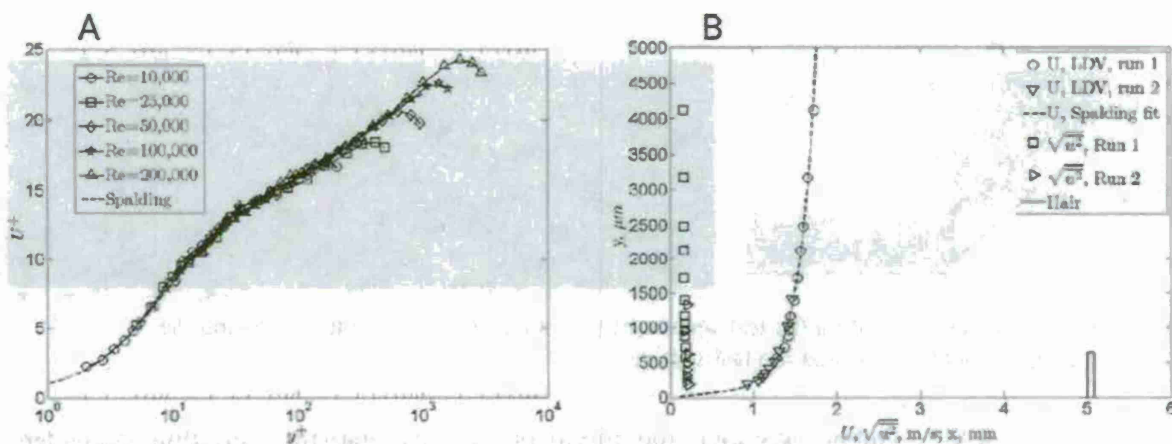


Figure 25: *A*, stream-wise velocity profiles in the channel through the range of Reynolds numbers tested. The dashed line is Spalding's (1961) blend between the linear viscous sublayer region and the logarithmic region. *B*, a typical dimensional near-wall approach flow profile data depicting the velocity and RMS velocity magnitudes along with the stream-wise location of the hair on the abscissa. These data were acquired at the stream-wise station 5mm upstream from the hair and at $Re = 200,000$.

Under different turbulent boundary layer flow conditions, typical haircell sensor responses were provided in Figure 26 in terms of time trace and power spectral density. Due to the fabrication defect, all the tested sensors performed poorly in maintaining stable zero-outputs before and after a testing run. However, the dynamic responses to turbulent flows (AC components) were very well captured by the sensors, which will be further discussed in correlation with LDV and LDVib measurements. With focus on the haircell sensor's AC responses, in Figure 26 the mean values of the signals were removed. Low-pass filter with cutoff frequency of 400Hz was also applied. It is evident that with increase of Reynolds number, the sensor signal becomes stronger and noisier gradually.

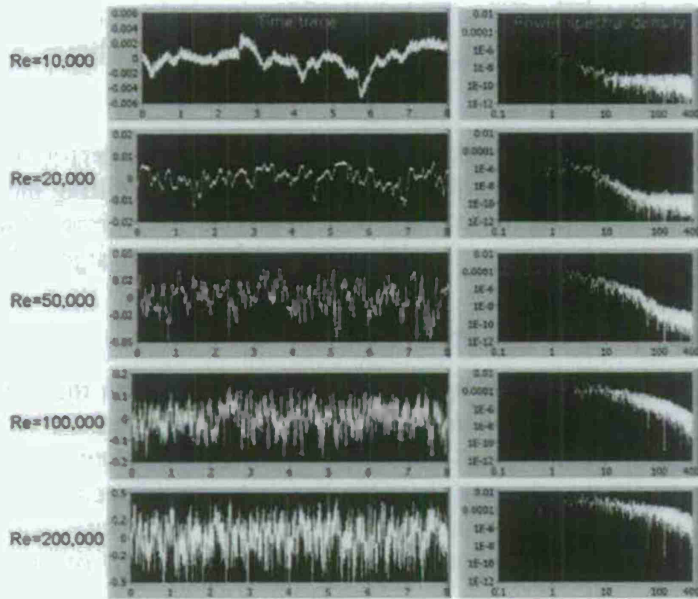


Figure 26: Time traces (left) and corresponding power spectral density (right) of the haircell sensor in response to turbulent boundary layer flow at various Reynolds numbers.

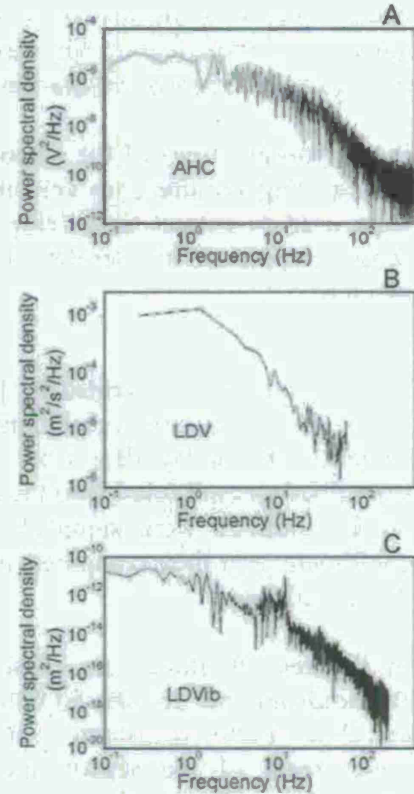


Figure 27: Comparison of power spectral densities obtained by different means at Re = 50 000. *A*, haircell sensor. *B*, LDV. *C*, LDVib.

Figure 27 compares the frequency responses to a turbulent shear flow at Re = 50 000, obtained by different means – haircell sensor, LDV, and LDVib. In general, the spectrum from the haircell sensor resembles that from LDV; the LDV data were taken 5mm downstream of the hair at an elevation of 650μm from the wall. Such resemblance suggests that the haircell sensor is capable of responding to the local turbulent flow faithfully. The LDVib spectrum, which reflects the hair vibration under turbulent flow excitations, also demonstrates a similar global pattern except for a peak at around 9 Hz. The 9Hz peak is due to the facility vibration caused by the flow-driving pump. The peak was not picked up by either the sensor or the LDV, since the local turbulent flow structure was much stronger than the facility vibration.

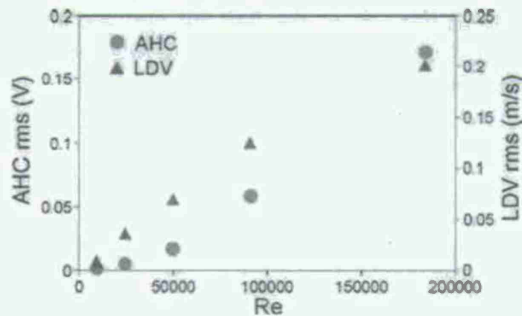


Figure 28: rms responses of the haircell sensor and the LDV with variation of Reynolds number.

The rms response of the haircell sensor with variation of Reynolds number was compared with that of LDV (Figure 28). Both data sets were based on an average of 7 time repetitive runs, and the error bars are too small to be plotted in this figure. It is clear that for both the haircell sensor and the LDV, the rms values increase monotonically and nonlinearly with increasing Reynolds number. Yet, the difference is evident; the second order derivative of the LDV plot is negative, whereas the second order derivative of the sensor plot is positive. This difference is

mainly due to the intrinsic nonlinear behavior of the haircell sensor, which has been verified via numerical simulation in our earlier work. Note that the above difference can be eliminated through careful sensor calibration.

Further observations of the response of the artificial haircell sensor to the flow were performed by acquiring simultaneous velocity and sensor data in a synchronized fashion. The resulting data were used to extract time-delay statistical correlations between the velocity behavior and the sensor response. The correlation coefficient between the velocity and haircell sensor signals is given as

$$R_{\text{velocity/voltage}} = \frac{\overline{uv}}{\sqrt{\overline{u^2}}\sqrt{\overline{v^2}}}$$

The $R_{\text{velocity/voltage}}$ is bounded by $[-1, 1]$ where 1 represents perfect correlation between the data and -1 is perfect anti-correlation; values near zero indicate little relationship between the two signals. Time delay data were obtained by shifting the sensor voltage measurements by a prescribed amount relative to the LDV velocity measurements. After the shift, the delayed sensor voltage outputs were sampled once for each corresponding LDV sample. The correlation coefficient was then computed for each set of time-delayed signals to the desired set of time-delay statistics.

In Figures 29, three sets of sensor data at Reynolds number 25 000, 50 000 and 200 000 correlate LDV measured velocities 5mm downstream of the sensor and one set of sensor data at $Re = 50\,000$ correlates the LDV measured velocity at 5mm upstream of the sensor. The elevation for the LDV measurements is the height of the sensor – 0.65mm. The dashed vertical line demarks the time delay value given by the ratio of the stream-wise spacing (d) between the velocity measurements and the haircell to the velocity of the approach flow at the top of the hair (U_{top}). This value is given as a reference for comparison to the time-delay value at which peak correlation is observed. These time-delayed peak correlations at various Reynolds numbers once again suggest loyal responses of the haircell sensor to the approaching/passing-by turbulent flows.

Personnel Supported

Yingchen Yang
Nannan Chen
Huan Hu
William Jacobs
Ozgur Yacuzcetin

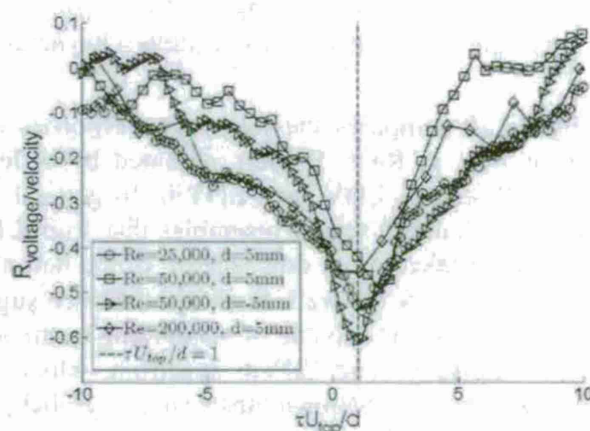


Figure 29: Time-delay correlation coefficient data for flow and LDV parameters given by the inset legend. Time delay is normalized by the flow velocity at the top of the haircell and the stream-wise spacing between the velocity measurements and the sensor.

ALGORITHM DEVELOPEMTN ON BIOINSPIRED FLOW SENSING

(Co-PI Douglas Jones, UIUC)

Objective

Develop signal-processing algorithms that enable various functions of arrayed haircell sensors in underwater applications.

Flow-Imaging Algorithm

The haircell sensors are designed to sense movement of water or air. Therefore, they can be directly used for source location applications in which the sensors can be installed on a platform such as a submarine to form an array and detect any source of vibration in the surroundings. At the early stage of the program, we started developing an algorithm to work with an array of MEMS hot-wire sensors as shown in Figure 30.

The hot-wire sensor operates on the principle of convective heat lost. That means the hot-wire element is heated above the ambient temperature using an electrical current. When it is exposed to a flow medium, the fluid convectively removes heat from the hot wire and causes its temperature to drop and its resistance value to change. So a hot-wire sensor can measure the local velocity of fluid at its location.

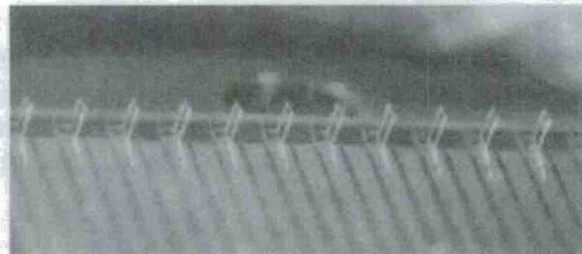


Figure 30: An optical micrograph of an array of hot-wire anemometers.

While exposed to a dipole field, which is a flow field generated by a sphere vibrating in water, an array on hot-wire anemometers will respond and form a spatial pattern. From such a response, we can build an algorithm to infer the location of the dipole source.

The goal of the signal-processing algorithm is producing a 2D image of the energy-level distribution of flow-creating moving objects in the surroundings. The approach is to scan all possible source locations in the surrounding region and to compute a likelihood function representing the level of agreement between the measured array response and the expected pattern assuming a dipole source at that location. The expected pattern can be derived from analytical models or from training templates.

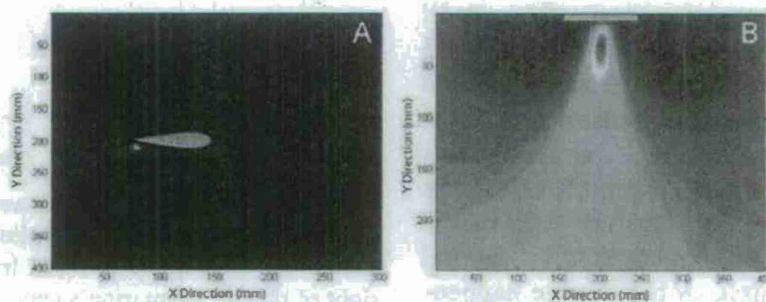


Figure 31: *A*, 2D pattern enabled by minimum variance beamforming algorithm to process signals from a linear array of MEMS hot-wire anemometers. *B*, 2D pattern generated by using the same algorithm to process signals from a fish contoured array of commercial hot-wire anemometers.

Different algorithms may produce different likelihood functions. In our earlier work we used a mean squared error function to generate images for detection and localization of a single source. This method is a maximum likelihood estimator under single-source assumptions. Another approach is based on a minimum variance beamforming framework or Capon's method. The method has been applied for far-field beamforming situation to search for direction of arrivals by exploiting the phase information. In this application, we adapted Capon's method for near-field context by using the magnitude information of sensors' outputs. With this approach we manage to produce much sharper images of the source locations. Figure 31 shows the successful images of an oscillating dipole source using either MEMS hot-wire sensors or commercial sensors. The algorithm achieves robustness over different types of sensors.

With Artificial haircell sensors being developed in Liu's group, an adaptive beamforming algorithm has been specifically developed for dipole source localization and hydrodynamic imaging. Technical details are provided in Liu's report.

Wake-Tracking Algorithm

Wake tracking is also an attractive application for hair-cell sensors. It is the capability of sensing the wake generated by a moving vehicle in water and using that information to follow or track that vehicle. In order to explore that capability, we attached two hair-cell sensors near the nose of a small model of a submarine and let it followed a bigger model as shown in diagram in Figure 32. Analyzing the signals from those two sensors on each side of the following submarine, we discovered that the difference in the ratio of root-mean-square over mean can reveal whether the following submarine is in the wake or not. This can be used as the signature of the wake imposing on the small submarine. Figure 32 depicts the change of that signature when the small submarine shifting its position from the left to the middle and the right of the big submarine's central axis. A big change happens when the small submarine start moving in the wake.

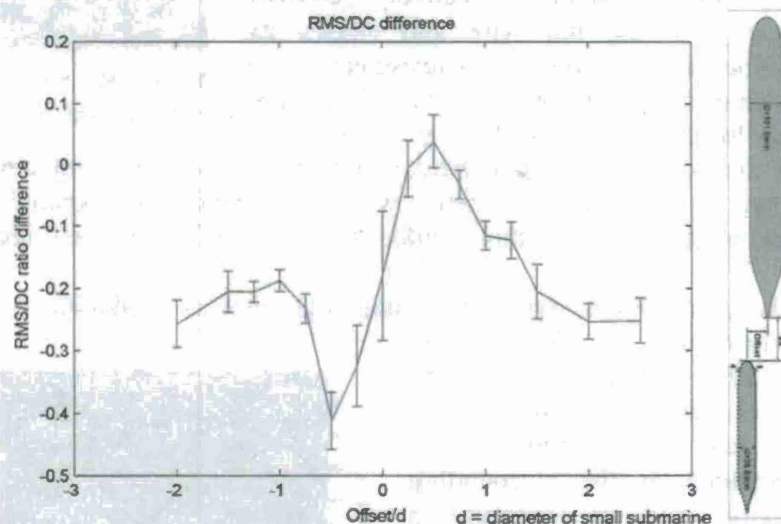


Figure 32: Wake signature sensed by two hair-cell sensors at the nose of the small submarine in following a big submarine as the small submarine shifting its position from the left to the middle then to the right of the big submarine's central axis.

Due to the time limit, we could not fully explore this effect for system of many pairs of sensors. However, the discovery of wake signature can lead to development of a more comprehensive and

complete algorithm that can automatically control and maintain the position of the small submarine staying behind and inside the wake of the big submarine.

Weak-Electric Sensing and Sparse Beamforming Algorithm

Besides working with hair-cell sensors to develop artificial sensory system with capability of near-field underwater imaging, we also investigated another bio-inspired sensing mechanism call weak-electric sense. Sensing via a weak electric field has been seen in nature in study of many types of electric fish.

Those fish can actively generate a weak electric field around its body in close range then detect the interference when an object presents in its electric field. Based on that principle, we built a proof-of-concept system to verify the idea of weak-electric sense (Figure 33).

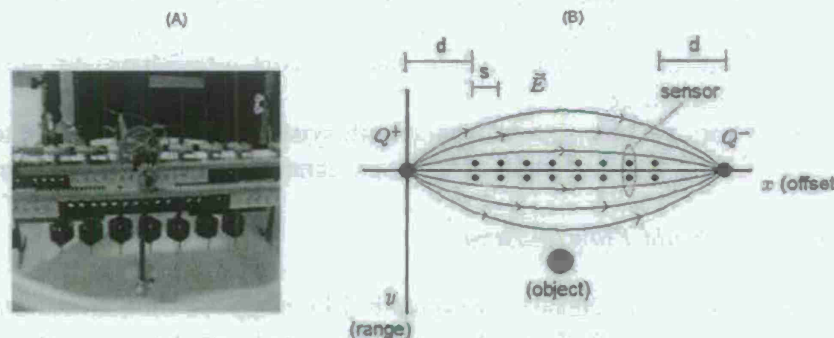


Figure 33: *A*, a proof-of-concept of weak-electric sensing experiment setting. *B*, operating principle of a weak-electric sensing system.

Together with the new idea of weak-electric sense, we also introduced a new concept of sparse beamforming algorithm. Instead of computing a likelihood function for each inspected location as in previous algorithm, we exploited the fact that the distribution of sources is very sparse in inspected space.

Therefore, the source location problem can be formed into an optimization problem with a constraint in sparsity of sources. We actually use the standard L1-optimazation technique to solve the sparse beamforming

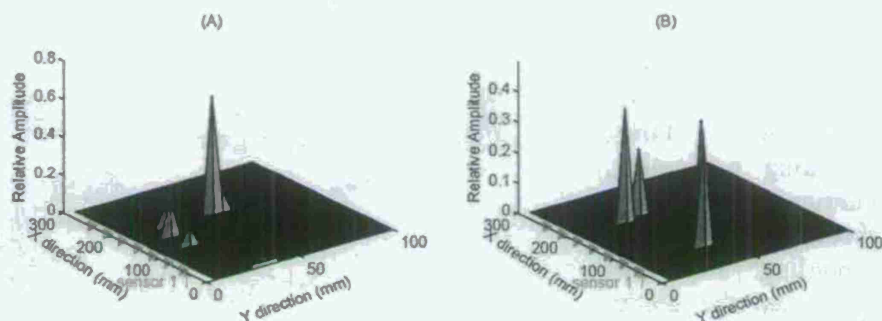


Figure 34: *A*, image of successfully mapping a plastic ball at about 45 mm in front sensor 5. *B*, image of mapping simultaneously 2 plastic ball objects at about 45 mm in range and between sensors 1 & 2 and sensors 5 & 6.

The results for real experiment shown in Figure 34 prove that the concept of both weak-electric sense and sparse beamforming can work in practice.

Personnel Supported

Nam Nguyen
Michael Lockwood

BIOINSPIRED HAIRCELL SENSOR WITH SYNTHETIC HYDROGEL CUPULA

(Co-PI Vladimir V. Tsukruk, MSE, Georgia Tech, GA)

Objectives

- Understanding of biological machineries in engineering terms
 - Understanding of fish cupula fundamental morphological and mechanical properties for efficient fluidic detection
 - Understanding of spider hair micromechanics for air detection
- Design of bioinspired “capped” sensors with enhanced performance
 - Synthesis of hydrogel materials with controlled shape and elastic properties resembling fish cupulae
 - Fabricate hair-sensor capped with synthetic hydrogel cupula to maximize response to fluidic flow as two distinct cases: canal and superficial structures

Enhanced Fluid Flow Sensing

The flow hair-like sensors developed in Liu group are mechanical-based piezoresistive hairs that were inspired by fish flow lateral line flow receptors (see Liu report). The current hair sensors consist of a polymer hair on a silicon-based microcantilever. The whole sensor is covered in parylene, which acts as a water proofing coating on the sensor. The flow-derived signal is transduced through a bending-induced resistance change. These sensors in an original design have a minimum detection threshold of above 0.2 mm/s. Maximizing the sensitivity and minimizing the detection threshold by different means are very important for many practical reasons, including enhancing the sight range of the system and increasing the spacing of a sensor grid.

Fish rely on flow receptors for several important tasks, including navigating, hunting prey, rheotaxis and schooling. Fish have developed the ability to sense flow rates in water with velocities as low as several micrometers per

second. The lateral line is a system of flow transducing neuromasts running along the outside of the fish body and inside a series of pores/canals along the body of fish, called superficial neuromasts and canal neuromasts, respectively. A neuromast typically includes from 20 to 1000 mechano-sensing hair cells. Neuromasts, the basic flow sensing unit in fish, is made up of many mechanosensing hair cells covered by a single, compliant bio-hydrogel structure called a cupula (Figure 35). Cupulae are usually around 100-1000 μm long, but their size and properties have been shown to vary greatly for different species. These cupulae couple the mechanosensing hair

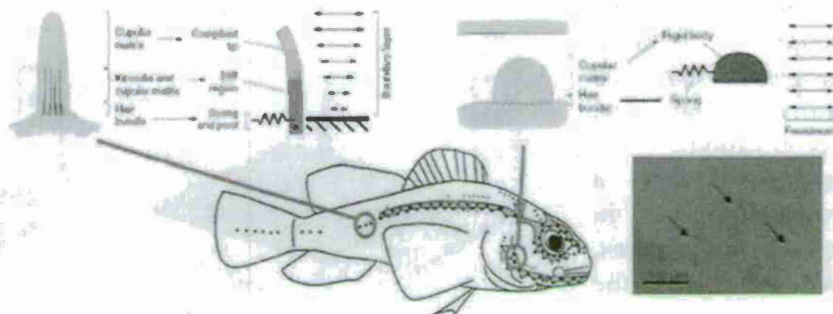


Figure 35: An optical image of goldfish superficial cupulae and schematics of canal neuromasts and superficial cupulae.

cells to the surrounding water flow by increasing the drag of the neuromasts, thereby enhancing the signal transmission to the hair cell.

In order to guide the development of an artificial cupula, the mechanical properties of superficial cupula in blind cave fish should be characterized. Thus, the mechanical properties of blind cave fish cupula were directly measured using fluid-based surface force spectroscopy with a colloidal probe. The elastic modulus of the fish cupula was measured in water using an atomic force microscope (AFM) operated in force-volume mode in accordance with usual approach developed in our group (Figure 36). The loading plot in coordinated penetration versus the applied load (Hertzian coordinate plot) was observed to be highly non-linear as caused by viscoelasticity of the materials associated with time-dependent, viscous response. The Voight viscoelastic model was combined with the Hertzian contact model to fit the non-linear loading data for the cupula. The biohydrogel was measured to have an elastic modulus of 9 kPa and a relaxation time of 0.42 seconds, characteristics of compliant and viscous materials.

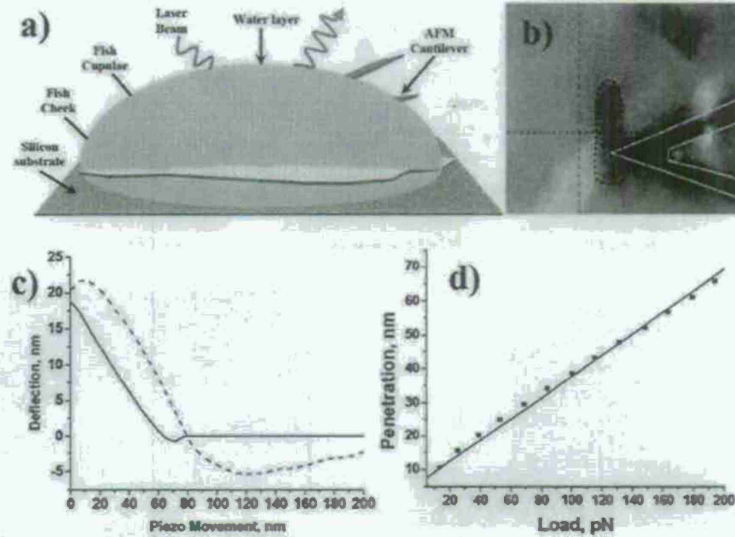


Figure 36: *A*, schematic of setup for cupula properties measurements. *B*, a screen shot of the cantilever pressing on a stained cupula. *C*, a typical force distance curve from fish cupula. *D*, data fit to Hertzian constant model of elastic material.

The synthetic cupulae with comparable mechanical properties were fabricated by photo-crosslinking tetra-acrylate functionalized poly-ethylene oxide glycols (PEG) (Figure 37). The initiator used cross-link the acrylate functionalized PEG was 2,2-dimethoxy-2-phenylacetophenone dissolved in 1-vinyl-2-pyrrolidone. The PEG was deposited directly on hair sensor and then exposed to ultraviolet light at 365 nm light under varying intensities and times. Photomasks were used to localized crosslinking and thereby patterning the PEG into different shapes through selective exposure and crosslinking of the hydrogel.

The flow sensor testing was carried out under water by shaking dipole placed at set distances from the sensor surface (Figure 37). The dipole amplitude and frequency was controlled and monitored, while simultaneously monitoring the Fourier transform of the sensor piezoresistive output. The dipole amplitude was varied to obtain the sensitivity and minimum threshold stimuli were measured by lowering the dipole amplitude until the sensor output became erratic. A second test involved constant (DC) laminar flow over the sensors in a flow chamber. In this test the flow velocity was varied controllably and the sensor piezoresistive output was simultaneously monitored. After the measurements were performed on the initial sensor with a bare hair, then the sensor was encapsulated in a dome-shaped cupula and tested under identical

flow conditions. The unaltered sensors tested here had minimum water velocity detection thresholds of around 0.2 mm/s, and after the synthetic cupula was applied to the sensors the threshold velocities improved by over 2.5 times to roughly 0.075 mm/s (Figure 37). Theoretical estimations indicated that the expected signal amplification for the increased cross-sectional area accounted for only about half of the actual signal amplification, indicating that additional contributions to the signal absorption. Apparently, the dome-shaped synthetic cupulae introduced above is important biomimicking design for canal-based sensing the tall superficial cupula is the appropriate biological analogue of the other type of flow sensing discussed below.

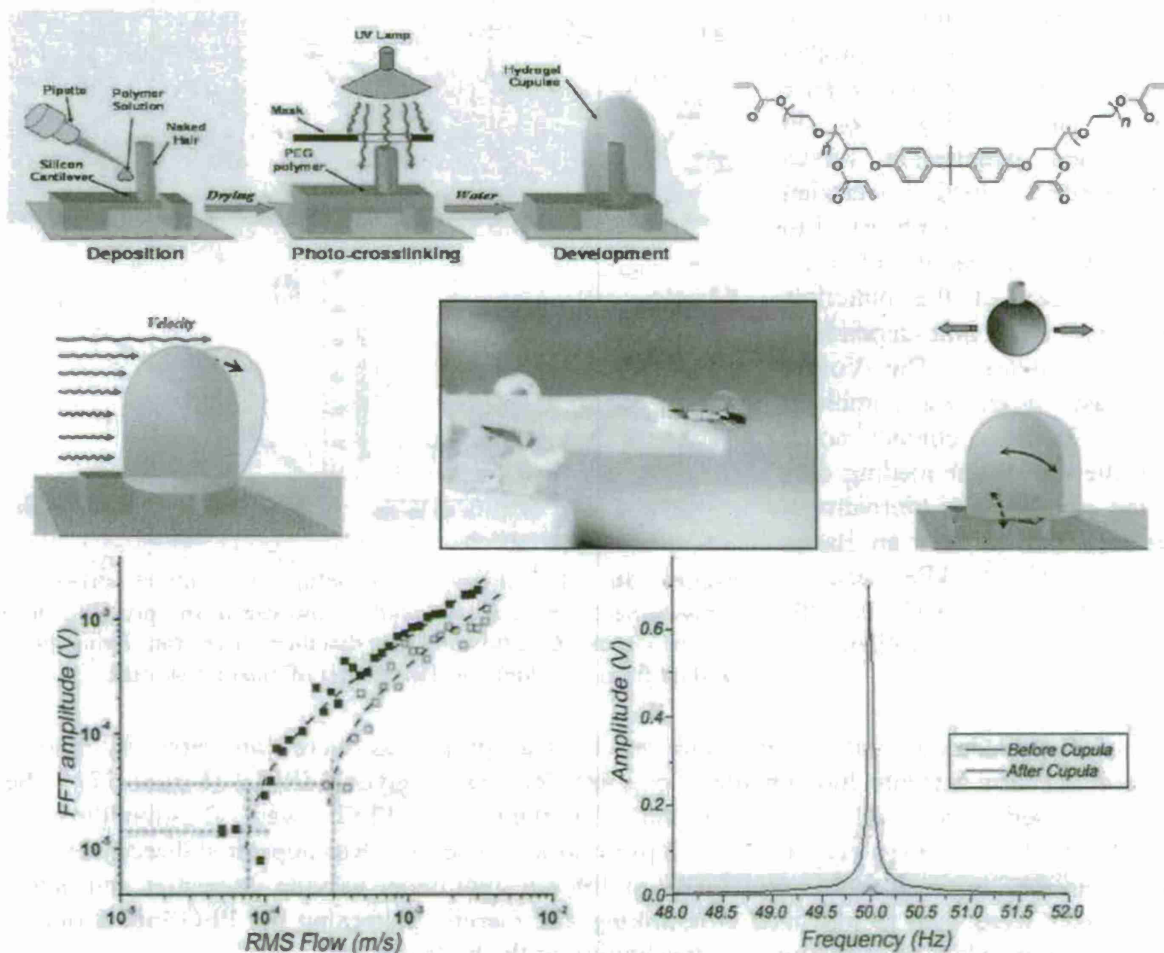


Figure 37: Fabrication procedure and chemical structure of synthetic cupula (top), cupula fabricated directly on hair sensor and sensitivity testing (laminar and oscillating flows) (center), and sensor response of bared hair (open circles) and cupula-capped hair (closed circles) and hair response to oscillating flow for bare (red) and cupula-capped (black) hair sensors.

High-Aspect Artificial Cupulae

The focus of this development was to build on previous demonstrations of improvements to engineered hair sensors from bio-inspired support structures. Specifically, the aim was to improve the previous dome-like cupula's performance by fabricating a higher-aspect ratio

cupula, much like that of fish superficial cupula. The dimensions and aspect ratio of blind cave fish superficial cupulae chosen for Bioinspiration were measured using confocal fluorescence microscopy and conventional optical microscopy (Figures 36, 38). The superficial cupulae were measured to have an average height of $104 \pm 13 \mu\text{m}$, a width of $26 \pm 3 \mu\text{m}$, and thus an aspect ratio of 4.0 ± 0.8 . We used this aspect ratio as a general guide for the development of high-aspect ratio synthetic cupula.

In order to fabricate tall synthetic cupula with a shape like that of superficial cupulae of fish (flag-like), we developed a controlled drop-casting method. To facilitate this endeavor a 3-axis micro-positioner used in conjunction with a side-view camera to position a syringe filled with the PEG macromonomer solution directly above the hair of the sensor (Figure 38). Then several drops of PEG solution were precisely dropped onto the hair without wetting the base surface. This method provided a degree of control over the height and width of the cupula by controlling

the number of drops and the volume of each drop, respectively. Furthermore, cupula collapse was prevented by avoiding wetting the surface surrounding the sensor. A study indicated that fish's bio-hydrogel cupula material was softer ($E \sim 10$'s Pa) than our blind cave fish measurements and that the stiffer cupula of blind cave fish was due to their rather dense network.

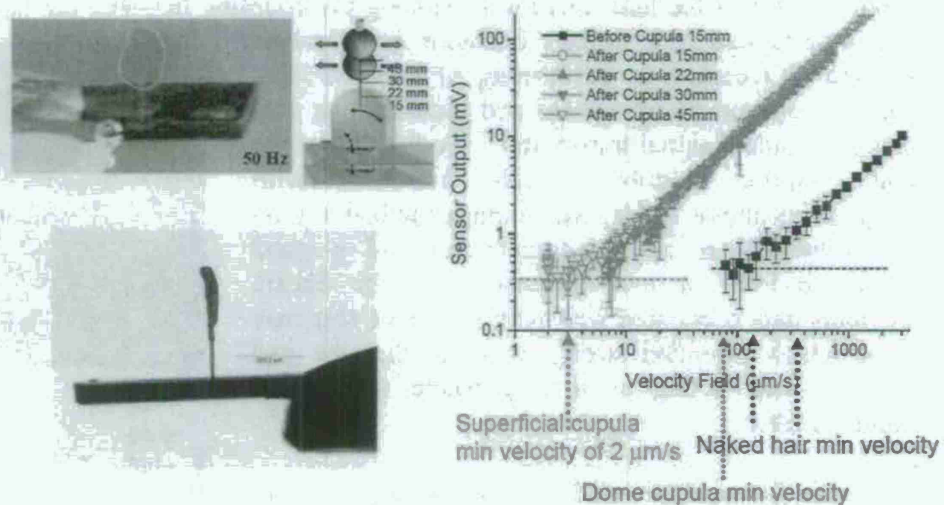


Figure 38: Tall superficial synthetic cupula on hair sensor (left) and sensor outputs vs velocity flow for bare and cupula-capped hairs (right).

The performance of the higher-aspect ratio synthetic cupula as a sensing enhancement structure was tested in a similar manner as the dome-shaped cupula, using the standard dipole test (Figure 38). There was an impressive difference in sensor performance before and after the addition of the bio-inspired structure: the sensitivity improvement was over 60 times more for the high-aspect ratio cupula, a tremendous improvement (Figure 38). The high-aspect ratio cupula improved the sensor minimum detectable velocity from $100 \mu\text{m/s}$ to $2\text{--}3 \mu\text{m/s}$. Whereas, the dome-shaped cupula resulted in a minimum threshold velocity of $75 \mu\text{m/s}$; overall the minimum detection threshold improvement of the high-aspect cupula out-performed the dome-shaped by 15 times. The achievement of an overall minimum detectable flow is quite remarkable considering limits of initial bare hair sensors within $0.1\text{--}0.2 \text{ mm/s}$. Furthermore, it is even lower than the minimum detectable flows of $18\text{--}38 \mu\text{m/s}$ that has been measured in different fish.

Therefore, through the bio-inspired approach of fabricated sensor super-structures with similar shape and properties, we were able to truly rival the performance of our biological models.

Air Flow and Vibration Sensing in Spiders

Wandering spiders (*Cupiennius*) are a genus, which unlike most spiders, do not use webs for hunting (see above). Their hunting strategy relies heavily upon their highly evolved vibration sensing receptors and wind-sensing receptors. Barth work with these creatures has revealed many unique and amazing features about their sensing. Therefore, understanding the ability of the wandering spider to efficiently process information may inspire novel solutions to signal processing challenges associated with large arrays of sensors.

The hair receptors have a hairs-on-hair morphology that increases the surface area (drag) to mass (inertia) ratio of the hair, thereby increasing the coupling between the hair and the flowing air. We investigated a high-pass behavior in vibration sensing slit receptors by performing AFM-based force spectroscopy on an associated pad material that acts as a mechanical signal transmitter. We found that the pad's elastic modulus steeply increased with frequencies above 10 Hz, which made the pad a good stress transmitter at high-frequencies and a good stress absorber at low frequencies. The elastic modulus data correlated well with the nerve response data, which provided strong evidence that the pad material was acting as a viscoelastic mechanical stimulus filter.

The main focus of this study was to directly measure the mechanical properties of the trichobothria. Furthermore, we were interested in investigating the origin of the high-pass behavior seen at low-frequencies in the nervous response data. We directly characterized the mechanical response of the air-flow receptors using AFM force-spectroscopy mode (Figure 39). The tests were performed by landing an AFM probe on a trichobothria of a live wandering spider. Nonetheless, the torsional constants were measured from experimental data (Figure 39) to be on the order of 10^{-11} Nm/rad, which is in good agreement with past work involving fluid-dynamics. In order to properly fit the data over the experimental frequency range, a 3-parameter model was utilized, which consists of a spring-element in parallel with a spring and dash-pot element that is in series.

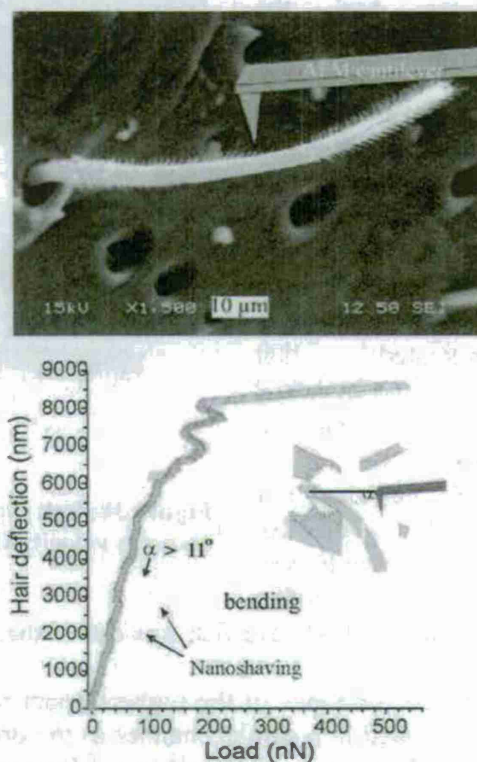


Figure 39: SEM of a trichobothria with a schematic cantilever added. Notice the hairs-on-hair morphology has been shaved off (top). A load-penetration curve that shows the pivoting response of the receptors, until it finally reaches the socket edge, at which point it bends (bottom) (see inset).

The higher than expected damping constant indicates a viscoelastic component in the receptor structure. It was suggested that the time-dependant dash-pot element was either the nerve-coupling structure or the nerve coupling structure itself. Without measuring the mechanical properties of the individual components, it is not possible to decisively determine the origin of the viscoelastic behaviour. Nonetheless, the implications of the different scenarios can be qualitatively interpreted and can be translated into implications for engineered sensors for leveraging. Depending, on whether the frequency stiffening component acts to transmit mechanical energy or not, determines whether the component will act in a high-pass or a low-pass role, respectively.

Personnel Supported

Dr. M. Julian, 2005-2006

M. Lemieux, 2005-2006

S. Peleshanko, 2006-2007

M. Ornatska, 2006-2007

M. McConney, 2005-2008

K. Anderson, 2007-2008

MATERIAL STUDY FOR BIOINSPIRED HAIRCELL SENSORS

(Co-PI Rajesh Naik, Air Force Research Laboratory)

Objectives

Development of multi-layered haircell to improve its resilience, and creation of an antifouling coating over the entire sensor.

Rubbery Photoresist Formulation

Our team has developed a rubbery photoresist, based upon poly(butadiene)-dimethacrylate, with several desired properties such as high flexibility and ease of use. Considerations of designing this photoresist included ensuring proper adhesion between all layers, enough flexibility so that the resulting haircells could bend 90° over 1000 times yet not be too flexible that vibration sensitivity was lost, high definition in the patterning process, and that the fabrication process remain as close as possible to traditional photoresist techniques and equipment. Typical height dimensions of this two-tiered haircell were 60µm for the lower rubbery resist and 740µm for the upper glassy resist, with a diameter of 80µm.

Prior to our collaboration, the haircell was made using solely SU-8 photoresist on top of a silicon wafer. The SU-8 monomer has eight epoxy groups, and when crosslinked, produces a very hard, glass-like material. It efficiently transmits any signal to the transducer, though it is fragile and will almost certainly break if dropped. The idea behind our research was to create a rubbery section to the lower tenth of the haircell to provide some flexibility in the overall device. After the bottom section is made, the SU-8 would be layered on top using the same mask.

The process began by applying a mono-layer adhesion promoter to the silicon substrate. By using 3-(trimethoxysilyl)propyl methacrylate, a covalent bond between the silicon substrate and the silane group was made, creating a surface rich with methacrylate groups. These groups were necessary to react with the rubbery resist formulation, which is acrylate-based.

The rubbery resist formulation incorporated three starting materials, the majority of which included a poly(butadiene)-dimethacrylate. This material is a slightly yellow, transparent, viscous monomer that cures into solid polymer with properties similar to a stiff rubber. A 6 wgt% type 1 photoinitiator was added that has both good surface and depth of cure. Finally, a 10 wgt% glycidyl-methacrylate was added to the formulation to promote adhesion with the upper, SU-8 layer. It should be noted that this formulation contained no solvent and did not require a pre-bake step. The resist was spin coated onto the primed device to a thickness of approximately 60 nm. The resulting coating was viscous enough that it behaved like a solid and would not flow after application.

Still, it should be patterned soon after coating. The wafer was placed in the mask aligner and the mask was pressed against the wafer for one minute before exposure. Exposure times were typically one minute. Afterwards, the mask was gently removed from the wafer since the uncured monomer remained tacky. The uncured monomer was dissolved by developing the system in SU-8 developer. The device was cleaned in propanol and blown dry (Figure 40).

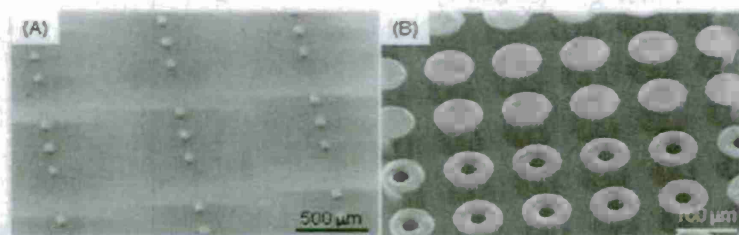


Figure 40: *A*, series of rubbery haircell sections patterned on a silicon wafer. *B*, close up of the rubbery haircell sections, including hollow haircells. Notice the high definition and the close spatial resolution.

SU-8 was then spin coated onto the wafer and the process repeated. The resulting hair is shown in Figure 41. It has been demonstrated that without the glycidyl-methacrylate addition to the rubber-resist formulation, the SU-8 does not adhere and washes off the rubber during its development stage.

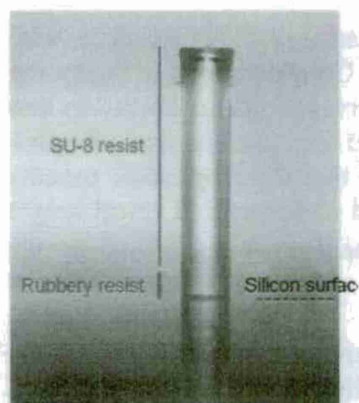


Figure 41: A completed two-tiered haircell composed of a rubbery polymer section on the bottom and a glassy SU-8 polymer section on the top.

The flexibility of just the rubbery section of the resist was tested by dragging the tip of a profilometer over a series of nine posts. In this test, the sample was moved under the tip of a stationary, sharp needle that had a downward force of 15mg. As the needle encountered a post, it bent the post until enough resistance was felt, at which time it lifted over the post. Once a scan was completed, the needle was raised, the stage returned to its original position, and the process was begun again. This procedure was repeated over a thousand times, over a period of ten hours. All the posts were unaffected after 230 scans. However, by the 243rd scan, one post had broken in half. After a thousand scans, a second post had also broken in half while a

third post had a small section nicked out of it. In the end, roughly 70% of the posts successfully withstood this rigorous test.

Anti-Fouling Coating Formulation

The second phase of this project focused on creating an antifouling coating for the sensors. Since these sensors were mounted on underwater vehicles, there was a high probability that they would be fouled. Although initially not visible to the eye, microfouling usually begins within hours of submersion. Microfouling involves diatoms, bacteria, and scum in general. Once these organisms form a foothold onto the sensor, macrofouling begins. Barnacles, mussels and seaweed are examples of macrofouling. Past strategies to control fouling include formulating paints that slowly leech out toxic compounds to continuously clean the surface of ships. However, there is ample evidence that these paints have a severely negative impact on the environment and are being phased out. Other strategies involve driving the vehicle quickly and to use the fluid velocity to pressure wash the ship. Another strategy can be to create micron-sized irregular surface patterning to make it difficult for microfouling to adhere.

Our strategy was to use a passive protective coating to prevent microfouling materials from sticking. Poly(ethylene glycol) (PEG) is a highly water soluble polymer that has antifouling properties when its molecular weight is over 4400 g/mole. Considerations for the antifouling coating include the requirement that the film is thin enough that it doesn't affect the device's sensitivity, is able to coat all the hidden surfaces of the artificial haircell, is uniform, flexible and adheres well to the device. The device is delivered for its antifouling coating just after it has been coated with parylene-A. The parylene coating is commonly used by electrical engineers to form a conformal, pinhole free coating with outstanding water and gas impermeability. The parylene-A used in this research is rich with amine groups, which will allow further chemistry to be performed.

The application of the coating is a four-step process. The first two steps amplify the number of primary amines available on the surface of the parylene. While every parylene-A repeat unit has an amine group, it is expected that the majority of them will be hidden under the surface of the coating. The few that are exposed will need to be increased so that it can be assured the entire surface of the sensor is coated with the antifouling material. The first step is to submerge the device in a 20% solution of pentaacrylate/methanol at 50°C for one hour. The amines on the parylene-A react with the acrylate groups via a Michael addition to create a covalent bond. After rinsing to remove excess pentaacrylate, the process is repeated by submerging the device in a 20% solution of tris-(2-aminoethyl)amine/methanol at 50°C for an hour. When completed, the device is rinsed to remove excess tris-amine. By now, it is expected that the population of amine groups on the parylene-A surface has grown significantly. The third step converts these amine groups into reactive methacrylate groups by submerging the device into a 10% glycidyl-methacrylate/methanol solution at 50°C for one hour. After rinsing, the device is ready for the final step of coating with PEG.

The PEG monomer formulation comprises of a twelve repeat unit PEG, capped with a monomethacrylate. A 3 wt% photoinitiator is added, and the resulting mixture is diluted further with methanol. The device is submerged in this formulation and exposed to 365nm UV light for

30 minutes. Afterwards, the device is quickly rinsed with methanol and then washed overnight in 50°C water. The coating is now complete. White light interferometry reveals that the thickness of the coating is between 30-40nm. Knowing how flexible PEG normally is and how thin this coating is when compared to the dimensions of the haircell, it is safe to assume that the coating will not affect the sensitivity of the device.

The success of the application of the coating can be verified by comparing the change of contact angle of a drop of water on the surfaces, and by analyzing the surfaces by atomic force microscopy (AFM). As seen in Figure 42, the value of the contact angle of water dramatically decreases after applying the hydrophilic PEG layer. The contact angle for an unmodified parylene-A surface is $82.55^\circ \pm 1.61$ ($n=18$), whereas the PEG functionalized parylene-A surface angle is $10.79^\circ \pm 0.47$ ($n=9$). Likewise, AFM reveals that the surface with the PEG coating becomes more rough, with an RMS roughness of 4.85nm, as opposed to 2.30nm. The surface texture of the two types of surfaces are also noticeably different (see Figure 43).

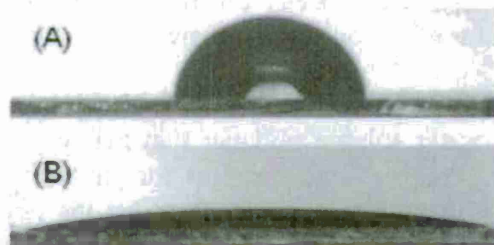


Figure 42: *A*, a drop of water on bare parylene-A coated onto a silicon wafer. *B*, a similar drop of water on a PEG-treated parylene-A wafer.

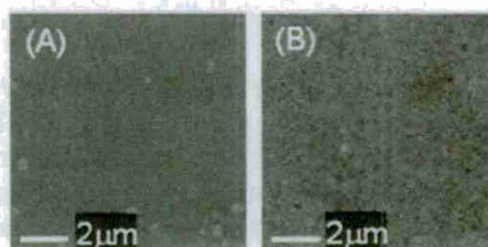


Figure 43: AFM phase images. *A*, a parylene-A covered silicon surface; *B*, a similar PEG-coated parylene-A surface.

The efficacy of the PEG coating can be tested using two techniques. The first is a relatively simple test that takes advantage of the notoriously adhesive properties of bovine serum albumin (BSA). A solution of fluorescently-labeled BSA is spotted onto both bare parylene-A and a wafer that has been treated with PEG. After waiting for a minute and then rinsing with water, the samples are imaged under a fluorescence microscope. Not only is the outline of the drop easily visible after spotting the control, the smear from the BSA being quickly submerged into the rinse water is also easily visible. This contact occurs in milliseconds, yet is unmistakable. On the contrary, the BSA did not attach at all to the PEG coating, further indicating its effectiveness in preventing fouling.

A second, more rigorous test was performed with the two types of slides by incubating them at 37°C overnight, with shaking, in a culture of *E-coli* that constitutively expressed green fluorescent protein (GFP). After the incubation stage, the samples were removed from the media and quickly rinsed in water. After drying, the slides were imaged

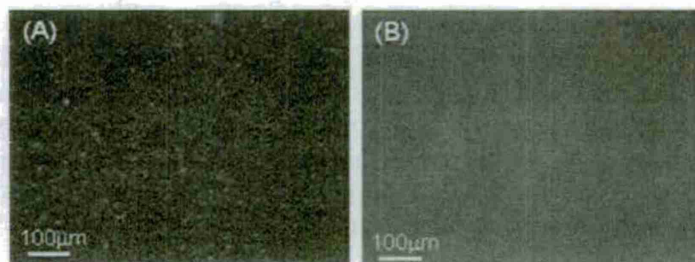


Figure 44: *A*, GFP-expressing E Coli attached to the surface of parylene-A. *B*, lack of GFP-expressing E Coli on PEG-treated parylene-A surface.

using a fluorescent microscope (see Figure 44). As before, it is apparent that the bacteria have begun to adhere to the control slide, where there is no evidence that they attached to the PEG-coated slides. Since this test highly encouraged the fouling of the surfaces with ample food, warmth and shaking, it is anticipated that the sensors will easily resist fouling in an aquatic environment.

Samples of the two types of slides were submerged in a salt water aquarium as an age study to try to replicate the actual conditions the sensors might encounter. The samples were placed in porous containers that allowed the water to flow through easily. The samples were removed at regular intervals, quickly submerged in fresh water to remove any unbound material, and then imaged under a light microscope (see Figure 45). Two types of records were taken: (1) a traditional optical image of the surface, and (2) a similar fluorescent image of the surface. The second type of photograph would highlight any living organisms. It is readily apparent that the untreated surfaces quickly fouled within three days. Conversely, the treated surfaces prevented fouling almost five times as long, simply by using this passive system.

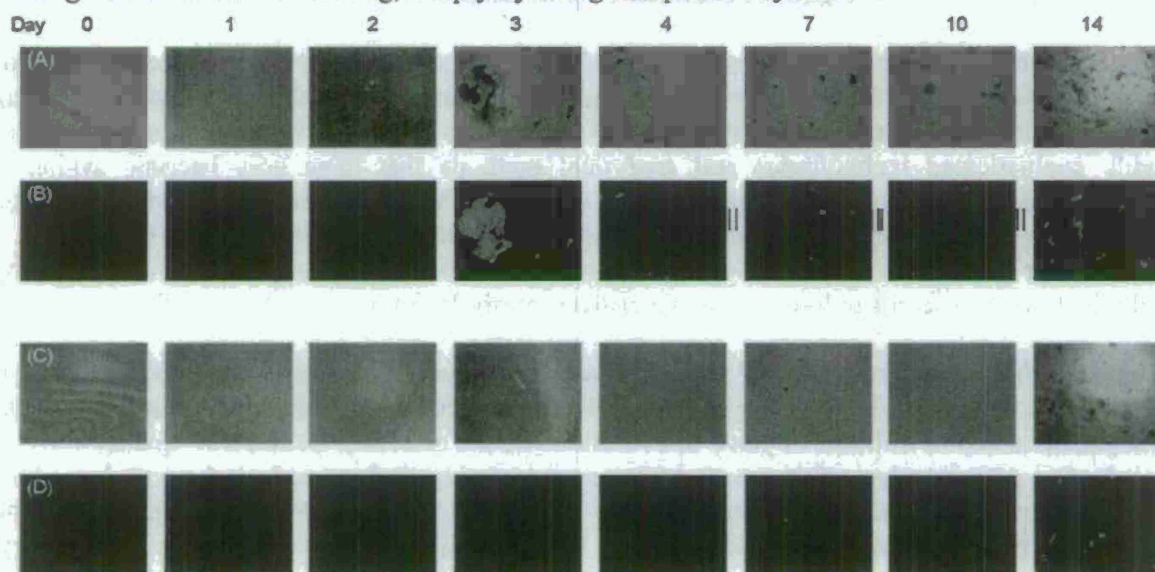


Figure 45: An age study of test coupons submerged over two weeks in a salt water aquarium. *A*, optical microscope viewgraphs of parylene-A coated silicon wafers. *B*, fluorescent microscope images of the same samples. The samples become noticeably fouled by the third day. *C*, PEG-coated parylene-A wafers as viewed under an optical microscope. *D*, fluorescent images of the same samples. Fouling does not begin to appear until the fourteenth day.

Personnel Supported

Lawrence Brott

ANALYTICAL AND NUMERICAL STUDIES ON FISH NEUROMASTS AND ARTHROPOD FILIFORM HAIRS

(Co-PI Joseph Humphrey, University of Virginia)

Objectives

The work performed under this contract by the UVA team falls under four main headings: (i) Sensors and Sensing in Biology and Engineering; (ii) Arthropod Motion Sensing Filiform Hairs; (iii) Fish Neuromasts; (iv) Seal Whiskers. In addition, Navier-Stokes based numerical calculations were performed for complex geometries corresponding to a pair of small-scale submarine-shaped objects aligned parallel to and close to each other. However, these data were preliminary at best and served principally for guidance. They have been communicated in earlier annual PPT reports and, as a consequence, are not reported here.

2008 - "Sensors and Sensing in Biology and Engineering"

Although the idea of *applying principles found in nature* to the design of engineering systems has a long history, only recently has biomimetics begun to establish itself with rapidly increasing impact in both biology and engineering. One of the reasons for this development is a number of highly sophisticated technologies and analytical methods that have now become available, highlighted among others by molecular biology on the one hand and micro- and nano-fabrication technologies in engineering on the other. The general interest in looking upon nature as a database for possible solutions of complex problems that have already been worked out by biological systems seems to have reached a critical threshold from where it is rapidly expanding.

There is *no life without sensors and sensing*. Even at the level of bacteria sensory performance is already well developed, guiding the cell's activity in its specific environment. Among the higher animals, hundreds of millions of years of evolution and the effects of permanent 'quality control' by selective pressures have fine tuned many sense organs to their specific tasks with incredible perfection, often reaching the limits of the physically possible regarding sensitivity and selectivity, but also impressive with regard to the efficient use of materials and energy. Biological sensory systems thus have an enormous potential for technical, industrial and medical applications. This applies to sensors specialized for many different forms of energy such as optical, electrical, magnetic, mechanical and chemical for the detection of light, electrical and magnetic fields, sound, vibrations, motion, pressure, strain and stress, to name a few. It includes sensory capacities alien to our human experience such as, for example, sensitivities in the infrared and ultrasound, electro-magnetic reception, and strain detection.

Simultaneously, remarkable advances in the areas of *synthetic materials and fabrication techniques* are making it increasingly possible to construct highly sensitive, selective, and relatively inexpensive micro/nano-electromechanical devices finding important sensory applications in a number of areas including: security (detection of air- and water-borne toxic materials); fluid medium motion sensing (in, for example, autonomous flying or underwater vehicles); medicine (implantable drug delivery systems, analysis of micro/nano-liter chemical solutions, surgical tactile gloves); the industry (nano-liter amplification of DNA).

in order to make *effective use of these innovation potentials*, and to develop new research strategies and new ways of thinking, it is of prime importance to intensify the dialogue among biologists, engineers, physical scientists, physicians and mathematicians, and to promote their actual collaboration and cross-disciplinary creativity. In this regard, the demands of industry, medicine, government and military agencies with respect to the development and application of sensor arrays, data reduction, evaluation and communication, and actuation decisions, all in the presence of background noise, are numerous and increasing in importance.

The *main goal of this Conference* is to bring together biologists, engineers, physical scientists, physicians and mathematicians for an exchange of first hand knowledge of the frontiers of research in their respective specializations and to prepare the ground for innovative lines of highly multi-disciplinary future work. These persons represent a wide spectrum of individuals from academia, government labs and industry. As seen from the program outline the topics to be treated cover a broad spectrum of problems ranging from processes of energy transformation and transduction to sensor array fabrication and application. These different fields are all linked and glued together by what a sensory system has to accomplish, both in biology and engineering. The outcomes and action items resulting from the Conference will be summarized to inform government agencies, foundations, academia, and industry concerning current and emerging research areas in need of sustained or new funding.

A conference as ambitious as this one could not have been organized without the considerable help of the session chairs to whom we express our sincere appreciation. We thank the staff at Engineering Conferences International for their help in arranging for and then helping to run the conference at the Grand Hotel San Michele in Cetraro (Calabria), Italy. Funding in support of the conference was generously provided by the Air Force Office of Scientific Research, the Engineering Conferences International, the National Science Foundation, the Office of Naval Research, the University of Vienna, and the University of Virginia.

2008 - "Medium Flow-Sensing Hairs: Biomechanics and Models"

Arthropods use fluid medium motion-sensing filiform hairs on their exoskeleton to detect aerodynamic or hydrodynamic stimuli in their surroundings that affect their behavior. The hairs, often of different lengths and organized in groups or arrays, respond to particular fluid motion amplitudes and frequencies produced by prey, predators, or conspecifics, even in the presence of background noise peculiar to the environment. While long known to biologists and experimentally investigated by them, it is only relatively recently that comprehensive physical-mathematical models have emerged offering an alternative methodology for investigating the biomechanics of filiform hair motion. These models have been developed and applied to quantitatively predict the performance characteristics of filiform hairs in air and water as a function of the relevant parameters that affect their physical behavior. They even allow the exploration of possible biological evolutionary paths for filiform hair changes resulting from physical selection pressures. In this communication we review the state of knowledge of filiform hair biomechanics and discuss two physical-mathematical models to predict hair dynamical behavior. One modeling approach is analytically exact, serving for quantitative purposes, while the other, derived from it, is approximate, serving for qualitative guidance concerning the parameter dependencies of hair motion. Using these models we look in turn at the influence of

these parameters and the fluid media physical properties on hair motion, including the possibility of medium-facilitated viscous coupling between hairs. The models point to areas where data is currently lacking and future research could be focused. In addition, new results are presented pertaining to transient flows. We qualitatively explore the possibility of an overlapping water-air niches adaptation potential that may explain how, over many generations, the filiform hairs of an arthropod living in water could have evolved to function in air. Because flow-sensing hairs have served to inspire corresponding artificial medium motion micro-sensors, we discuss recent advances in this area. Significant challenges remain to be overcome, especially with respect to the materials and fabrication techniques used. In spite of the impressive technological advances made, nature still remains unrivalled.

2008 - "Response of Cricket and Spider Motion Sensing Hairs to Air Flow Pulsations"

Closed form analytical solutions are presented for the angular displacement, velocity, and acceleration of motion sensing filiform hairs exposed to air flow pulsations of short time duration. The specific situations of interest correspond to a spider intentionally moving towards a cricket, or an insect unintentionally moving towards or flying past a spider. The trichobothria of the spider *Cupiennius salei* and the cercal hairs of the cricket *Grillus bimaculatus* are explored. Guided by earlier work, the spatial characteristics of the velocity field due to a flow pulsation are approximated by the local incompressible flow field due to a moving sphere. This spatial field is everywhere modulated in time by a Gaussian function represented by the summation of an infinite Fourier series, thus allowing an exploration of the spectral dependence of hair motion. Because of their smaller total inertia, torsional restoring constant, and total damping constant, short hairs are found to be significantly more responsive than long hairs to a flow pulsation. It is also found that the spider trichobothria are underdamped, while the cercal hairs of the cricket *Grillus bimaculatus* are overdamped. As a consequence the spider hairs are more responsive to sudden air motions. Analysis shows that while two spiders of different characteristic sizes and lunge velocities can generate pulsations with comparable energy content, the associated velocity fields display different patterns of spatial decay with distance from the pulsation source. As a consequence, a small spider lunging at a high velocity generates a smaller telltale far-field velocity signal than a larger spider lunging at a lower velocity. The results obtained are in broad agreement with several of the observations and conclusions derived from combined flow and behavioral experiments performed by Casas et al. (2008) for running spiders, and by Dangles et al. (2006) for spiders and a physical model of spiders lunging at crickets.

2008 - "Surface force spectroscopy point load measurements and viscoelastic modelling of the micromechanical properties of air flow sensitive hairs of a spider (*Cupiennius salei*)"

The micromechanical properties of spider air flow hair sensilla (trichobothria) were characterized with nanometre resolution using surface force spectroscopy (SFS) under conditions of different constant deflection angular velocities $\dot{\theta}$ (rad s⁻¹) for hairs 900 – 950 μ m long prior to shortening for measurement purposes. In the range of angular velocities examined (4×10^{-4} – 2.6×10^{-1} rad s⁻¹) the torque T (Nm) resisting hair motion and its time rate of change \dot{T} (Nm s⁻¹) were found to vary with deflection velocity according to power functions. In this range of angular velocities the motion of the hair is most accurately captured by a three parameter solid model, which numerically describes the properties of the hair suspension. A fit of the three-

parameter model (3p) to the experimental data yielded the two torsional restoring parameters $S_{3p} = 2.91 \times 10^{-11} \text{ Nm rad}^{-1}$ and $S'_{3p} = 2.77 \times 10^{-11} \text{ Nm rad}^{-1}$ and the damping parameter $R_{3p} = 1.46 \times 10^{-12} \text{ Nm s rad}^{-1}$. For angular velocities larger than 0.05 rad s^{-1} , which are common under natural conditions, a more accurate angular momentum equation was found to be given by a two-parameter (2p) Kelvin solid model. For this case the multiple regression fit yielded $S_{2p} = 4.89 \times 10^{-11} \text{ Nm rad}^{-1}$ and $R_{2p} = 2.83 \times 10^{-14} \text{ Nm s rad}^{-1}$ for the model parameters. While the two parameter model has been used extensively in earlier work primarily at high hair angular velocities, to correctly capture the motion of the hair at both low and high angular velocities it is necessary to employ the three-parameter model. It is suggested that the viscoelastic mechanical properties of the hair suspension work to promote the phasic response behaviour of the sensilla.

2007 - "Directional Asymmetry in Responses of Local Interneurons in the Crayfish Deutocerebrum to Hydrodynamic Stimulation of the Lateral Antennular Flagellum: Experimental Findings and Theoretical Predictions"

We have recorded spiking responses from single, bimodally-sensitive local interneurons (Type I) in the crayfish deutocerebrum to hydrodynamic and odorant stimuli flowing in two directions past the lateral antennular flagellum. Changing the direction of seamless introductions (meaning, with minimal variations of fluid velocity magnitude) of odorant flow past the flagellum, from proximal \rightarrow distal to distal \rightarrow proximal, did not consistently affect the dose-dependent responses of Type I neurons. By contrast, changing the direction of an abruptly initiated flow of water (or odorant) past the flagellum resulted in consistently larger numbers of spikes in response to this hydrodynamic stimulation when the flow direction was proximal \rightarrow distal. This response asymmetry is discussed in relation to its possible relevance regarding antennular flicking behavior. The putative involvement of flagellar hydrodynamic receptors, the beaked hairs, and the hydrodynamic flow asymmetries they are exposed to, are examined theoretically in the following companion paper by Humphrey and Mellon (2007).

2007 - "Analytical and Numerical Investigation of the Flow Past the Lateral Antennular Flagellum of the Crayfish *Procambarus clarkii*"

Analytical and numerical methodologies are combined to investigate the flow fields that approach and pass around the lateral flagellum of the crayfish *Procambarus clarkii*. Two cases are considered, the first being that of a free-flicking flagellum and the second corresponding to a flagellum fixed inside a small bore tube. The first case is the natural one while the second corresponds to the experimental configuration investigated by Mellon and Humphrey (2007) in a companion communication. In that study the authors observed a hydrodynamic-dependent asymmetry in the spiking responses recorded from single, bimodally-sensitive local interneurons (Type I) in the crayfish deutocerebrum, whereby the direction of an abruptly initiated flow of fresh water (or odorant) past the flagellum resulted in consistently larger numbers of spikes in response to the hydrodynamic stimulation when the flow direction was proximal-to-distal. In this communication we show that the proximal-to-distal and the distal-to-proximal flows produced in the flagellum-in-tube experiment correspond closely to the flows associated with the downward and upward strokes, respectively, of a free-flicking flagellum. We also show from calculations of the drag forces acting on the putative mechanoreceptor sensilla circumferentially distributed around the flagellum that there are at least two sources of hydrodynamic asymmetry possibly

related to the electrophysiologically asymmetry observed: a) the sense (but not the magnitude) of the drag forces acting on medial and lateral mechanoreceptors changes, in the same way for both, with change in flick direction; b) during a downward (an upward) flick, a ventral (dorsal) mechanoreceptor experiences a larger drag force magnitude than a dorsal (ventral) mechanoreceptor. These natural hydrodynamic asymmetries are correctly reproduced in the flagellum-in-tube experiment.

2007 - "The Air Flow Generated by a Flying Prey Insect around a Wandering Spider and its Motion Sensing Hair Sensilla"

Spiders use cuticular filiform hairs (trichobothria) to detect air motions generated by flying prey and predators. The wandering spider *Cupiennius salei* has about 900 such hairs on its pedipalps and legs. Their length and base diameters range from 100 μm to 1400 μm and 5 μm to 10 μm , respectively, and hairs of different length are arranged in characteristic clusters. Using an optically transparent test section for digital particle image velocimetry measurements, we analyzed the flow field generated by a flying prey (*Calliphora erythrocephala*) around *Cupiennius salei*. The humming fly was placed in biologically important positions with respect to the spider. The flow fields ahead of the fly showed velocities detectable by the trichobothria from a distance of at least 13.2 cm. Since their frequency content differs significantly from that of background flow they may well be used by the spider as signals indicating the fly's approach. Flow patterns change with the fly in different positions. The closer the fly was to the spider the more the absolute values for peak velocity and turbulence intensity increased. The peak velocity and the turbulence intensity above the fourth walking leg (WL4) changed from 5.11 mm/s and 29 % with the fly approaching the spider and 10 cm away from its center to 13.84 mm/s and 97 % (only 5 cm away). As the trichobothria do not respond to constant air velocity but to its fluctuations (Barth and Höller 1999), the rms values and the turbulence intensity are of major interest. The increasing turbulence intensity may well indicate to the spider that a fly is approaching. When comparing the peak velocities and the turbulence intensity right above the tarsi of each walking leg the highest values were measured above the walking leg closest to the fly (see WL4). The values decreased for the walking legs further away. Thus above WL1 and with the fly approaching the spider from behind and 5 cm away from its center the values for peak velocity and turbulence intensity were only 2.68 mm/s and 63 %. Considering the differences at the eight legs of the spider these may well be used as indicators of the azimuthal direction towards the prey.

2008 - "Drag Force Acting on a Neuromast in the Fish Lateral Line Trunk Canal: Part I - Numerical Modeling of External-Internal Flow Coupling"

Fish use a complex, multi-branched, mechanoreceptive organ called the lateral line to detect the motion of water in their immediate surroundings. This study is concerned with a subset of that organ referred to as the lateral line trunk canal (LLTC). The LLTC consists of a long tube no more than a few millimeters in diameter embedded immediately under the skin of the fish on each side of its body. In most fish, pore-like openings are regularly distributed along the LLTC, and a minute sensor enveloped in a gelatinous cupula, referred to as a neuromast, is located between each pair of pores. Drag forces resulting from fluid motions induced inside the LLTC by pressure fluctuations in the external flow stimulate the neuromasts. This study, Part I of a

two part sequence, investigates the motion-sensing characteristics of the LLTC and how it may be used by fish to detect wakes. To this end, an idealized geometrical/dynamical situation is examined that retains the essential problem physics. A two-level numerical model is developed that couples the vortical flow outside the LLTC to the flow stimulating the neuromasts within it. First, using a Navier-Stokes solver, we calculate the unsteady flow past an elongated rectangular prism and a fish downstream of it, with both objects moving at the same speed. By construction, the prism generates a clean, periodic vortex street in its wake. Then, also using the Navier-Stokes solver, the pressure field associated with this external flow is used to calculate the unsteady flow inside the LLTC of the fish, which creates the drag forces acting on the neuromast cupula. Although idealized, this external-internal coupled flows model allows an investigation of the filtering properties and performance characteristics of the LLTC for a range of frequencies of biological interest. The results obtained here and in Part 2 show that the LLTC acts as a low pass filter, preferentially damping high frequency pressure gradient oscillations, and hence high frequency accelerations, associated with the external flow.

2008 - "Drag Force Acting on a Neuromast in the Fish Lateral Line Trunk Canal: Part II – Analytical Modeling of Parameter Dependencies"

In Part 1 of this two-part study, the coupled flows external and internal to the fish lateral line trunk canal (LLTC) were consecutively calculated by solving the Navier-Stokes equations numerically in each domain. With the external flow known, the solution for the internal flow was obtained using a parallelepiped to simulate the neuromast cupula present between a pair of consecutive pores, allowing the calculation of the drag force acting on the neuromast cupula. While physically rigorous and accurate, the numerical approach is tedious, and inefficient since it does not readily reveal the parameter dependencies of the drag force. In Part 2 of this work we present an analytically based physical-mathematical model for rapidly calculating the drag force acting on a neuromast cupula. The cupula is well-approximated as an immobile sphere located inside a tube shaped canal segment of circular cross-section containing a constant property fluid in a steady-periodic oscillating state of motion. The analytical expression derived for the dimensionless drag force is of the form

$$\frac{|F_N|}{|P_L - P_R| \pi (D/2)^2} = f\left(\frac{d}{D}, \frac{L_t}{D}, \omega_D^*\right)$$
 where $|F_N|$ is the amplitude of the drag force, $|P_L - P_R|$ is the amplitude of the pressure difference driving the flow in the inter-pore tube segment, d/D is the ratio of sphere diameter to tube diameter, L_t/D is the ratio of interpore tube segment length to tube diameter, and $\omega_D^* = \omega (D/2)^2 / \nu$ is the oscillating flow kinetic Reynolds number (a dimensionless frequency). Present results show that the dimensionless drag force amplitude increases with decreasing L_t/D and maximizes in the range $0.65 \leq d/D \leq 0.85$, depending on the values of L_t/D and ω_D^* . It is also found that in the biologically relevant range of dimensionless frequencies $1 \leq \omega_D^* \leq 20$ and segment lengths $4 \leq L_t/D \leq 16$, the sphere-tube (neuromast-canal) system acts as a low pass filter for values $d/D \leq 0.75$, approximately. For larger values of d/D the system is equally sensitive to all frequencies but the drag force is significantly decreased. Comparisons with Navier-Stokes calculations of the drag force show good agreement with the analytical model results. By revealing the parameter dependencies of the drag force, the model serves to guide biological understanding and the optimized design of corresponding bioinspired artificial sensors.

2007 - "Hydrogel-encapsulated microfabricated haircell mimicking fish cupulae neuromast"

Biological organisms interact with their surroundings by means of a variety of sensory systems of which a number of ones is based upon micromechanical principles such as bending hairs for tactile sensing in human beings, shaft-like deflection of stiff hairs for vibration detection in spiders, flexible membranes for night vision in snakes, long whiskers for wake tracking in seals, and superficial neuromasts (hairs) for navigation in some fish. In contrast, active sonar systems are widely used for a variety of civil and military applications in underwater environment. However, passive sensor systems similar to fish provide a huge advantage in "silent" observation of the environment which does not reveal the source and does not interfere with moving vehicles and various life forms. Although these receptors have been studied for many years, the microfabrication of artificial hair-like sensors mimicking the functions of the natural ones has begun only recently, and has usually been based on relatively basic, idealized structures involving the simplistic materials design principles of biological receptors matched to current silicon-based microfabrication technologies. In this report, we introduce a combined, hybrid soft-hard material design of a hair flow microsensor, which closely mimics the superficial neuromast of a blind cavefish *Astyanax fasciatus mexicanus* with its superior ability to navigate blindly in a hydrodynamically complex underwater environment. The glycoprotein cupulae couple the arrays of hairs to the surrounding environment maximizing and mediating drag forces along a moving body. For these motives, we propose new strategy of the hydrogel encapsulation of an artificial haircell microsensor obtained with conventional CMOS microfabrication technology and deployed for sensitive flow detection. A combination of haircell sensor with a hydrogel cupula grown by wet-chemistry micropatterned photopolymerization suggested here creates an integrated hair-cupula sensor with superior flow detection ability comparable with blindfish. We suggest that this symbiotic technology may enable the self-navigating ability of autonomous underwater vehicles.

2007 - "Experimental and Numerical Investigation of a Fish Artificial Lateral Line Canal"

Fish use the mechanosensory lateral line to detect water motions in their immediate surroundings and thus are able to avoid predators, track prey, swim in schools, and circumnavigate underwater objects. The basic unit of the lateral line is the neuromast, a sensory structure that consists of mechanosensitive hair cells enveloped in a gelatinous cupula. Lateral line neuromasts are distributed along the head and body of fish, either superficially on the skin or in subepidermal water-filled canals that open to the surroundings through a series of pores (Coombs et al. 1988). Water motions external to the fish induce pressure driven water motions inside the lateral line canal that drag on the cupulae of canal neuromasts causing them to be displaced by a few nanometers. These displacements, in turn, stimulate the underlying hair cells (Kalmijn 1988) which then signal the presence of the external water motions to the fish brain. Researchers have investigated fluid motions inside artificial lateral line canals (ALLCs) in response to sinusoidal external water motions to understand the functional significance of lateral line canals (LLCs). These studies have shown that LLCs behave like straight ALLCs of roughly the same cross sectional area. If an ALLC is stimulated in still water with a small-amplitude vibrating sphere placed adjacent to the canal, the water velocity inside the canal is proportional to the component of the external water acceleration that is parallel to the canal (Denton and Gray 1983). Up to now the filter properties of ALLCs have only been investigated in still water and only with a vibrating sphere as an external stimulus source. However, a fish may face a more complicated situation

because either the fish moves, the water moves, or both move. We have conducted a collaborative investigation of this problem by performing numerical calculations at the University of Virginia and experimental measurements at the University of Bonn.

2006 - "Numerical Calculation of the Flow in the Fish Lateral Line Canal: Applications to Predators Tracking Prey"

Fish use sensors inside the lateral line trunk canal (LLTC) to detect the motion of water in their surroundings. The LLTC is a complex sensory organ consisting of a long tube no more than a few millimeters in diameter embedded immediately under the skin of the fish on each side of its body. In most fish, pore-like openings are regularly distributed along the LLTC, and a minute sensor enveloped in a gelatinous cupula, referred to as a neuromast, is located between each pair of pores. Drag forces resulting from fluid motions induced inside the LLTC by pressure fluctuations in the external flow stimulate the neuromasts. The present study investigates the motion-sensing characteristics of the LLTC and how it may be used by fish to track prey. A two level numerical model is presented that couples the surrounding flow outside the LLTC to that stimulating the neuromasts within it. First the unsteady flow past a pair of simulated prey/predator fish in coasting motion is calculated using a Navier-Stokes solver. Then the pressure field associated with this external flow is used to drive the flow inside the LLTC of the predator, which creates the drag forces acting on the neuromast. The model is used to investigate the filtering properties and performance characteristics of the LLTC for a range of unsteady flows of biological interest. The results obtained suggest that the LLTC preferentially filters high frequency pressure gradient oscillations, and hence high frequency accelerations, associated with the external flow.

2007 - "Design, Fabrication and Testing of a Bioinspired Hybrid Hair-Like Fluid Medium Motion Sensor Array"

Many animals detect motions in air and water by means of specialized hair-like sensilla that respond with high sensitivity and specificity to the fluid medium motion. For a review see Humphrey and Barth (2007). Examples are the filiform hairs of arthropods such as arachnids, crustaceans and insects, and the vibrissae of seals. In the case of the arthropods the sensors are relatively small (diameter ~ 5 -10 microns, length ~ 100 – 1000 microns). In the case of seals they are much larger (diameter ~ 1 -2 mm, length ~ 50 – 150 mm). These sensors are generally clustered in arrays consisting of hairs of different lengths which, for example, in the case of the cricket *Grillus bimaculatus* and the spider *Cupiennius salei* can result in frequency fractionation of the motion signals detected. We have designed, fabricated and tested a new type of hybrid sensor array that embodies favorable features taken from the spider trichobothria (such as the flexible membrane structure that supports a trichobotrium) and the seal vibrissae (such as the larger hair length). Each sensor in the array is embedded in a polydimethylsiloxane (PDMS) platform that simulates the spider trichobothrium membrane. Four pairs of capacitors associated with each sensor allow the N-S and E-W detection of fluid motion parallel to the plane of the platform. Sensitivities in the order of few picofarads per 0.5° angular displacements of the sensors are obtained. Measurements and modeling of the sensor array are presented and discussed.

2006 - "Investigation of a Bioinspired Whisker-Like Fluid Motion Sensor"

Sensors and sensing technologies to obtain flow information at near real time for the control of new underwater morphing structure applications are being investigated. Inspiration for a new type of fluid motion sensor finds its origin in the vibrissae (whiskers) of seals. Recent research has shown the remarkable sensitivity and specificity of these biological sensors to detect hydrodynamic trails left by potential prey. The impressive sensory performance characteristics of seal whiskers suggest the developmental potential for corresponding synthetic fluid motion sensors. An analytical study of the dynamic response of a synthetic whisker-like beam has been carried out to understand its response to predefined vortical flow fields. A parametric study has been conducted to examine how the geometrical and material parameters (i.e. length, cross-section, and stiffness) can be manipulated to produce characteristic responses for different applications. This theoretical understanding is being used in a companion experimental study to develop a synthetic whisker-like sensor. The performance characteristics of the experimental sensor are compared to the beam model predictions.

Personnel Supported

Charlotte Barbier
Shriram Pillapakkam
William Eberhardt

FLOW-SENSING RELATED FISH BEHAVIORAL STUDIES

(Co-PI Sheryl Coombs, Bowling Green University)

Objectives

Behavioral studies on the orienting behavior of mottled sculpin and on active flow-sensing and wall-following behaviors of blind cavefish.

Research overview

The primary goals of BGSU efforts were to (a) investigate the behavioral use of lateral line flow information by fish, (b) determine some of the performance capabilities and limitations of lateral-line mediated behaviors, (c) identify the sensorimotor strategies that fish use to achieve behavioral goals (e.g. to capture prey) and (d) work with BioSEnse engineers to translate these strategies into engineering design rules for enhancing performance capabilities of engineered systems. To accomplish these goals, we used behavioral approaches to investigate lateral line-mediated behaviors in two species of fish that (a) rely heavily on lateral line sensory information for their natural behaviors and (b) use flow information in two, fundamentally different ways. Lake Michigan mottled sculpin, *Cottus bairdi*, feed predominantly at night. In the absence of vision, mottled sculpin exhibit an unconditioned, lateral line-mediated, orienting response to prey-like water vibrations. This orienting response was used in behavioral assays of their ability to determine prey location when distance and orientation (axis of prey movement) were varied (Braun and Coombs, In Press; Coombs and Patton, 2009). In particular, we tested the

hypotheses that (a) mottled sculpin use excitation peaks (local 'hot spots') in stimulation patterns along the lateral line to determine the location of an artificial prey and (b) that vibratory sources can elicit both unconditioned orienting behaviors dominated by lateral line inputs, as well as classically-conditioned (learned) behaviors dominated by inner ear inputs.

Whereas mottled sculpin use a form of *passive* flow-sensing to detect the minute water motions created by prey movements, Mexican blind cavefish, *Astyanax mexicanus*, can additionally use a form of *active* flow-sensing to detect stationary features in their environment. That is, they use their own swimming movements to generate a flow signal for probing the environment, much as bats or dolphins produce echolocating sounds for probing theirs. Rather than using the auditory system to detect sound reflections from stationary features, however, blind cavefish use their lateral line system to detect object-generated distortions in their self-generated flow field. Because these fish have evolved non-visual means to compensate for an evolutionary loss of eyes in response to living in total darkness, they are ideal animal models for studying the role of active flow-sensing in obstacle avoidance and spatial navigation. In blind cavefish studies, we investigated their ability to use active flow-sensing for wall-avoidance and wall-following behaviors, believed to be important for spatial exploration of novel environments (Sharma et al, 2009; Patton et al, in prep).

Spatial Excitation Patterns in Dipole Orientation by Mottled Sculpin (Coombs and Patton, 2009)

Information contained in the spatial excitation pattern along arrayed sensors in the lateral line system of Lake Michigan mottled sculpin, as well as other surface-feeding fish and amphibians, is thought to play a fundamental role in guiding prey-orienting behaviors. However, the way in which prey location is encoded by the excitation pattern and used by the nervous system to direct orienting behaviors is largely unknown. The neural representation of prey location is made difficult by the fact that the stimulus field about vibratory (dipole) sources is not radially symmetrical and by the fact that source orientation (axis of vibration), distance and location (both azimuth and elevation) all

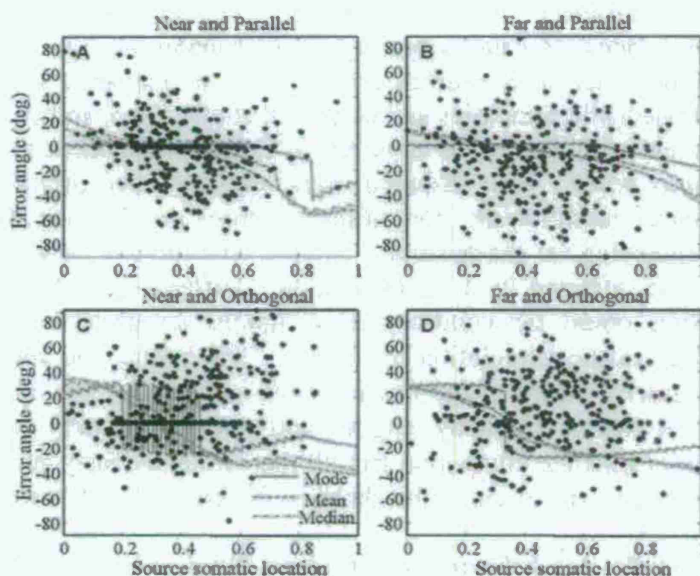


Figure 46: Predicted (grey lines) vs actual (black dots) orienting errors as a function of somatotopic location of the source along the fish for each of the four stimulus conditions: a (near and parallel), b (far and parallel), c (near and orthogonal) and d (far and orthogonal). Near and far distances = 3 and 6 cm, respectively. Somatotopic location is scaled to one fish body length, where 0 represents the most rostral (snout) location and 1 represents the most caudal (tail) location. Predicted errors are plotted for each of three generic models (mode- grey solid line, mean- grey dashed line, and median- grey dot dashed line).

interact to determine the pattern of stimulation along the somatotopically-distributed lateral line system. In this study, we tested the hypothesis that mottled sculpin use excitation peaks (local 'hot spots') to determine the somatotopic location of an artificial prey (vibrating sphere/dipole source) along the body surface. Dipole orientation (axis of sphere vibration re: long axis of the fish) was manipulated to produce excitatory peaks in different body locations without changing the actual sphere location. Dipole distance was manipulated to cause changes in the spatial extent and peak amplitude of stimulation patterns. In addition, we used modeling techniques and a few simplifying assumptions to test whether the orienting responses of mottled sculpin are guided by local 'hot spots', defined by measures of central tendency (the spatial mode, mean or median) of activity patterns along the mottled sculpin lateral line system. Our results show that orienting accuracy is largely independent of source orientation, but not source distance and that turning directions are not guided by local hot spots in the somatotopic activation pattern of the lateral line (Figure 46). Rather, we propose that there is an array of neural filters in the midbrain that are tuned to particular combinations of source orientation, distance and somatotopic location.

Vibratory sources as compound stimuli for both the ear and lateral line (Braun and Coombs, In Press)

An underwater vibratory source simultaneously presents acoustic and hydrodynamic disturbances. Because vibratory dipole sources are poor sonic projectors, most researchers have assumed that such sources are of greatest relevance to the lateral line system (LL). Both hydroacoustic principles and empirical studies have shown that vibratory dipole sources are also a potent stimulus to the inner ear of fishes. Responses to vibratory sources in mottled sculpin (*Cottus bairdi*) were assessed using unconditioned orienting, differential and non-differential-classical conditioning. Orienting responses are dominated by LL inputs and eliminated by LL pharmacological inactivation. Simple conditioning depends on inputs from other systems and was not affected by LL inactivation. Differential conditioning alters behavioral control, and sculpin could be conditioned to ignore substrate borne vibrations and respond only to hydroacoustic stimulation of the ear. The lateral line and inner ear of mottled sculpin do not necessarily exhibit range fractionation, as both systems operate over a similar distance from the animal (within 1.5 body lengths) and respond to many of the same sources. Vibratory dipole sources generate compound stimuli that simultaneously activate multiple octavolateralis systems, and animals make use of the channels differentially, depending on the behavioral task.

Wall-following behaviors by Mexican Blind cavefish (Sharma et al, 2009; Patton et al, In Prep)

In a series of behavioral studies, we examined a very simple, yet little-understood behavior in which visually-deprived animals as diverse as cockroaches and humans, tend to seek out and follow the walls or boundaries of a novel environment. Despite numerous and varied speculations about the function of this widespread behavior, there have been few, if any, direct tests of its actual function in any species. We hypothesized that wall-following behavior is part of an overall sensorimotor strategy for exploring novel environments when long-range, visual sensing of distant landmarks from a single vantage point is prevented. To test this hypothesis, we investigated behavioral responses to novel environments in two morphs of the same species

(*Astyanax* sp): Mexican blind cavefish, which rely solely on non-visual senses and Mexican tetra, which normally have access to both visual and non-visual senses. The following questions were addressed: (1) Do sighted morphs exhibit wall-following in the dark, but not in the light, as predicted by the exploratory hypothesis? (2) Do blind cavefish exhibit enhanced wall-following capabilities compared to sighted morphs in the dark? (3) Can artifactual, non-functional explanations for wall-following behaviors be excluded? (4) What are the relative contributions of touch and touch-at-a distance (lateral line) to wall-following behaviors of blind cavefish?

In the first of two studies, the behaviors of Mexican blind cavefish and sighted Mexican tetra were videotaped after fish were introduced into a novel environment under dark (infrared) or well-lit conditions. Both sighted river morphs and congenitally blind, cave-dwelling morphs exhibited wall-following behaviors with subtle but significant differences in response to a novel environment in the dark. In contrast, sighted morphs placed in the same novel, but well-lit environment exhibited dramatically different behaviors that fell into two general categories: (1) holding stationary positions near the wall for long periods of time (a behavior never observed in the dark for either blind or sighted morphs) or (2) moving in and around the central region of the environment without moving along the walls. Blind cavefish appeared to have enhanced wall-following capabilities compared to sighted morphs in that they exhibited (1) a more nearly parallel orientation of the head and body with respect to the wall compared to a more wall-ward orientation of the head in sighted morphs, (2) a higher degree of continuity and persistence of wall-following behaviors, and (3) a more rapid development of consistently high swimming speeds (~1.5 BL/s).

Wall-following behaviors of both blind and sighted morphs in the dark suggest that both morphs use short-range, non-visual (lateral line and touch) senses and locomotor strategies to compensate for the loss of vision. In contrast, reduced levels of locomotor activity and the absence of wall-following behaviors in sighted morphs under well-lit conditions suggest that locomotor strategies associated with the use of short range senses (wall-following) are not required when long-range, visual cues are available. Differences between wall-following behaviors of blind and sighted morphs in the dark may largely be understood in terms of differences in active flow-sensing capabilities and strategies for acquiring short-range information through the lateral line system. We conclude that both sighted and blind morphs have inherited a primitive wall-following behavior from their sighted ancestor and that over time, wall-following behaviors of blind morphs have evolved to become more finely honed for exploratory purposes than those of sighted morphs. Anatomical specializations of the lateral line as well as behavioral specializations for active flow-sensing are likely to contribute to these enhanced abilities.

In the second of two studies, we investigated the function and sensory basis of wall-following behavior. There are at least two proposed functions for this behavior: (1) an exploratory function for finding resources and acquiring knowledge about the spatial configuration of the new space and (2) a protective function for finding shelter and escape routes. An alternative explanation for this behavior is that it has no particular biological relevance at all and is merely an incidental consequence of how the fish's movements are redirected every time the walls of a concave environment are encountered as a barrier to forward motion. Regardless of the true function,

blind cavefish exhibit remarkable entrainment to the wall surface, maintaining a very narrow range of distances from, and nearly parallel orientations to the wall when following it.

In order to (1) determine the sensorimotor strategies that blind cavefish use for following walls and (2) test the hypothesis that wall-following behaviors are an incidental consequence of reactions to walls as barriers, we used digital video to record the wall-following behaviors of fish in a goggle-shaped arena that had straight and both concave and convex surfaces of equal radii of curvature (21.5 cm or ~ 5 fish body lengths). We reasoned that if fish were using a purely reactive strategy, they would cease to follow the wall after they traveled along the concave portion of the arena and reached the transition point between concave and convex portions. That is, the wall at this point would no longer impede forward motion, so the fish would continue along a straight path. Alternatively, if fish were using a regulatory strategy to follow walls (i.e. moving towards the wall when it was perceived as being too far away and moving away from the wall when it was perceived as being too close), they would continue to follow around the convex curve. Studies were conducted under IR illumination in a light-tight environment to rule out possible contributions of non-retinal photoreceptors in the pineal gland. Fish were divided into two groups – a control group for which the lateral line system was intact and a treatment group for which the lateral line system was pharmacologically blocked by immersing fish in a 0.05 mmol L⁻¹ solution of CoCl₂. In addition, the frequency of departure from a convex surface that continuously changed its radius of curvature from 15 cm (~ 3 fish body lengths) to <5 cm (~ 1 body length) was measured using a third group of untreated fish.

Results from these studies revealed that for fish with functional lateral lines, the departure rates from the continuously changing convex surface increased in a nearly linear fashion from 0 (15 cm radius of curvature) to 100% (5 cm radius). The ability of fish to follow convex walls is thus clearly constrained by the radius of curvature. For a sufficiently large, fixed radius of curvature (21.5 cm) in the goggle arena, the mean success rate (N=8) for following half way around the convex wall was quite high (Fig. 2, light grey bars behind black bars) and much greater than that expected by chance alone. Furthermore, the mid-way point is 16.5 cm (~ 4 body lengths) beyond the concave-to-convex transition point, where the reactive hypothesis predicts that departures from the wall should occur. For a criterion distance twice as long (all the way around the curve), success rates

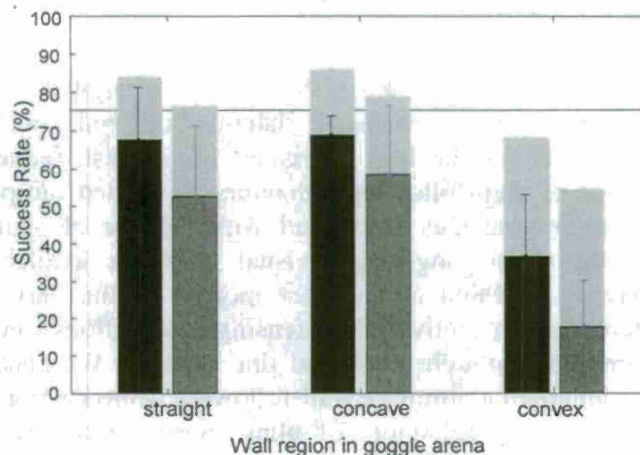


Figure 47: Mean success rates (8 normal fish and 8 lateral-line blocked fish) for following walls in different regions of the goggle-shaped arena. Black bars indicate the mean frequency with which normal fish followed straight, concave, or convex walls for their full length (33 cm), whereas dark grey bars to the right indicate the mean frequency with which treated fish did the same. Light grey bars behind the black bars indicate the mean frequency with which normal fish followed at least half (~ 16 cm) of the wall region in question, whereas light grey bars behind the dark grey bars indicate the same for lateral-line blocked fish. Error bars, in all cases indicate standard deviations from the mean.

were reduced, but nevertheless substantial and significantly greater than chance (Figure 47, black bars). In all cases, success rates for following around the convex surface were less than those for straight or concave surfaces (Figure 47). Pharmacological blocking of the lateral line reduced the frequency with which fish were able to follow the wall for distances of either 16.5 or 33 cm, but only significantly so for the convex curve (Figure 47, dark grey bars).

Based on these results, we conclude that wall-following behaviors cannot be explained by a simple, reactive strategy to avoid barriers whenever they are encountered or by chance alone. Rather, fish seem to be alternately attracted and repelled from the wall in a regulatory-like fashion. While the evidence is clear that blind cavefish are capable of actively regulating their distance from a convex wall, following such a wall clearly poses greater difficulties for them than does following a straight or a concave wall. This difficulty can be explained by the increased probability of moving further away from the wall when gliding on a straight course past a convex surface as compared to a concave or straight surface. The probability of moving further away from a convex surface should increase as the radius of curvature decreases, a prediction that is consistent with results showing an increase in wall departure rates as a function of decreasing radius of curvature.

Although it is clear that the lateral line is not necessary for wall-following behaviors, significant reductions in wall-following along convex regions of the arena after lateral line inactivation clearly show that the lateral line plays a role. One explanation for the significance of this effect for convex, but not straight or concave surfaces is that lateral line information is particularly important at distances just beyond the pectoral fin reach of the fish. Thus, if fish swim out of reach of the pectoral fin when gliding past a convex surface, lateral line information is needed to guide them back to the wall after losing tactile contact. The regulatory hypothesis postulates that fish regulate their distance from the wall, meaning that when their senses inform them that they are too close, they move away and when too far away, they move closer. These results are thus consistent with the idea that tactile senses play a dominant role in informing fish when they are too close, whereas the lateral line plays a dominant role in informing them when they are too far away.

Personnel Supported

Paul Patton, Ph.D, Research Scientist
Brandon Casper, Ph.D., Postdoctoral Fellow
Saurabh Sharma, Graduate Student

BIOLOGICAL STUDY ON LATERAL LINE SENSING OF FISH

(Co-PI Horst Bleckmann, University of Bonn, Germany)

Objectives

To study the responses of midbrain lateral line units of goldfish under hydrodynamic stimuli, and to explore how the lateral line of goldfish uses its sensory structures to encode hydrodynamic stimuli.

Electrophysiological study

Single midbrain (toral) lateral line units of goldfish do not encode the position of an object. However, if the responses (spike rate and phase angle) of several midbrain lateral line units are taken into account, the position and vibration direction of a stationary sphere can be determined (Figure 48). Thus up to the level of the midbrain (torus semicircularis), the information about sphere position and sphere vibration direction is not encoded at the single unit level of but presumably as a population code. One of the most important findings of the physiological study is, that some midbrain lateral line units do not confuse

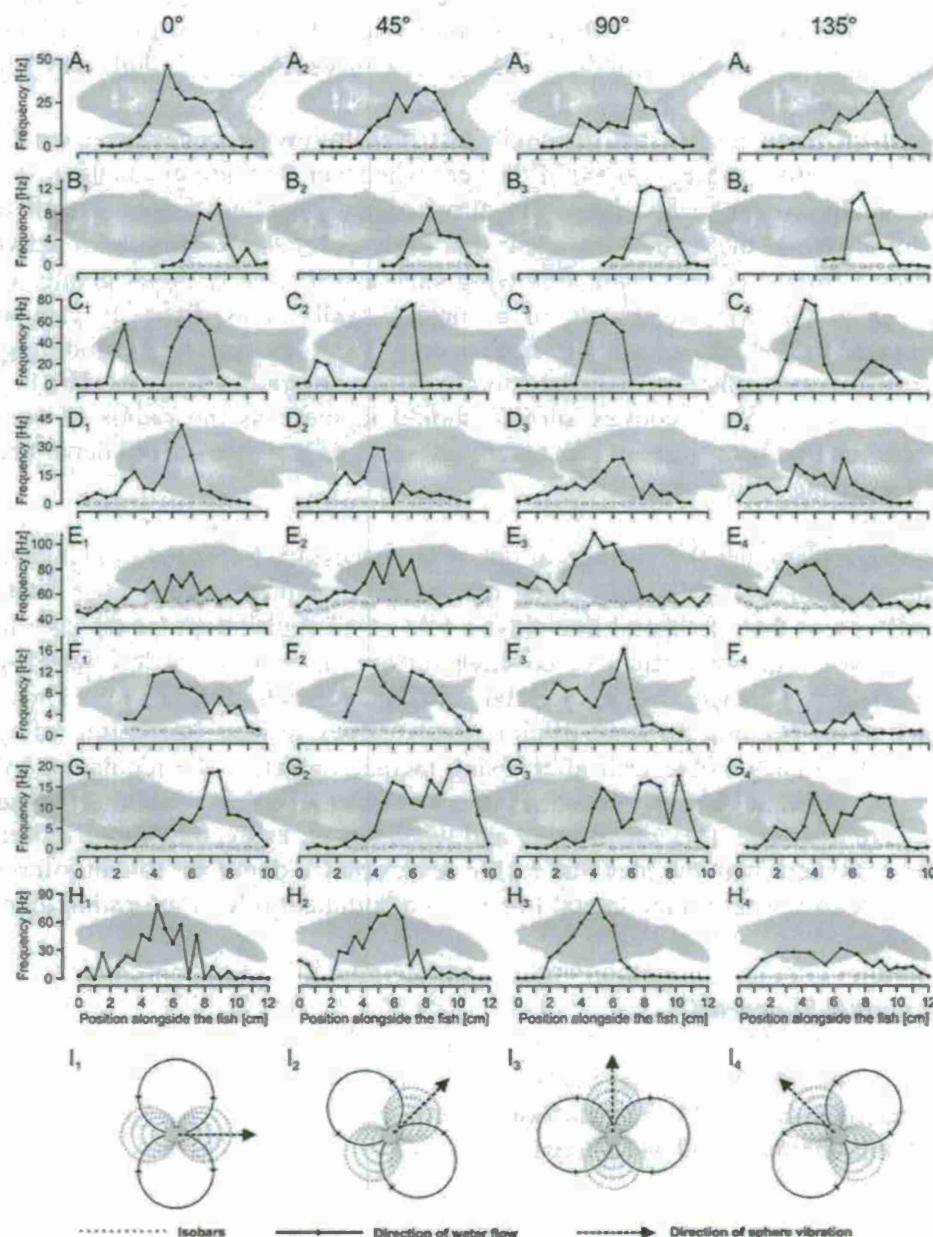


Figure 48: Spatial excitation patterns of eight (A-H) midbrain units plotted in form of evoked (solid) and ongoing (dashed) activity caused by a stationary vibrating sphere stimulus as function of sphere position and axis of sphere vibration. The distance between fish and sphere was 10 mm. Axis of sphere vibration was 0° (parallel to the fish), 90° (perpendicular to the fish), 45° or 135°. Fish shown are actual experimental animals. Please note that the y-axis in E starts at 40 and that the y-axis scale in H differs from the others. Fish size and fish positions are to scale. I Directions of sphere vibration with isobars and flow lines.

sphere position with sphere vibration direction.

How do lateral line fibers respond to water currents

In order to understand how lateral line fibers respond to water currents we recorded the discharges of anterior and posterior lateral line nerve afferents while stimulating goldfish with bulk water flow. According to previous studies we found that with increasing flow velocity lateral line afferents increased their discharge rates. However, an increased response to flow rates occurred even if flow direction was reversed. Taken the morphology of the receptors into account into account, this contradicts a direct encoding of water velocity by the lateral line receptors. Thus, we showed that individual lateral line afferents do not encode the direction of running water.

Taking advantage of a detailed particle image velocimetry analysis of the water flow generated to stimulate the fish, we showed that the amount and amplitude of flow fluctuations increased with increasing flow velocity. Together with physiological data on lateral line fibers that showed an increase in bursting activity, these combined findings strongly suggest that lateral line afferents mainly respond to the fluctuations that develop under natural flow conditions, rather than to the bulk current flow.

How can the lateral line system encode velocity and direction of water currents

In the previous section we had shown that single lateral line afferents respond only to flow fluctuations and not to the steady component of a natural water flow. Consequently, a single lateral line afferent can encode neither bulk flow direction nor velocity. It is possible, however, for a fish to obtain bulk flow information using multiple afferents that respond only to flow fluctuations.

By means of particle image velocimetry, we showed that, if a flow contains fluctuations, these fluctuations propagate with the flow. A cross-correlation of water motion measured at an upstream point with that at a downstream point can then provide information about flow velocity and flow direction. Since the lateral line fibers, as shown above, respond to fluctuations rather than to the bulk flow, the lateral line system might be able to use the fluctuations to calculate water flow velocity and water flow direction. In order to test this hypothesis we recorded simultaneously from pairs of primary lateral line afferents while a fish was exposed to either bulk water flow, or to the water motion caused by a moving object.

We were able to confirm that the responses of pairs of lateral line afferents that innervate nearby sensoryreceptors were highly correlated, if they were time-shifted to correct for gross flow velocity and gross flow direction. This experimental evidence shows that in principal the lateral line system is able to detect water flow direction and velocity using a combination of 2 receptor structures. To prove that a cross-correlation mechanism can be used to retrieve the information about gross flow velocity and direction, we measured the flow-induced bending motions of two flexible micropillars separated in a downstream direction. A cross-correlation of the bending motions of these micropillars did indeed produce an accurate estimate of the velocity vector along the direction of the micropillars.

How do water currents affect the detection of sinusoidal stimuli

Having shown that single lateral line afferent fibers do not respond to the water velocity of a natural flow but rather to the fluctuations present in the flow, we wanted to gain a deeper understanding on how water flow affects lateral line stimulus encoding. We therefore investigated how fibres in the anterior lateral line nerve of goldfish, respond to sinusoidal water motions in a background of still or running water. Two types of fibres were distinguished: type I fibres, which most likely innervate superficial neuromasts, were stimulated by running water (10 cm s^{-1}) while type II fibres, which most likely innervate canal neuromasts, were not stimulated by running water. The responses of type I fibres to sinusoidal water motions were masked in running water whereas responses of type II fibres were not masked. We used particle image velocimetry data of the water motions generated in the experiments in order to be able to quantify the stimulus properties. These findings are in agreement with previous data obtained from the posterior lateral line nerve of goldfish. Furthermore, we demonstrated that for type I fibres the degree of response masking increased with increasing flow velocity, i.e. in our case with increasing amount of turbulences.

How do fish detect hydrodynamic trails

Fish use the lateral line system for prey detection, predator avoidance, schooling behavior, intraspecific communication and spatial orientation. In addition the lateral line may be important for station holding and for the detection of the hydrodynamic trails (vortex streets) generated by swimming organisms such as fish. We investigated the responses of anterior lateral line nerve fibers of goldfish to unidirectional water flow (10 cm s^{-1}) and to running water that contained a Kármán vortex street. Compared to still water conditions, both unidirectional water flow and Kármán vortex streets caused a similar increase in the discharge rate of anterior lateral line nerve fibers. If exposed to a Kármán vortex street, the amplitude of spike train frequency spectra increased at the vortex shedding frequency. This increase was especially pronounced if the fish intercepted the edge of a Kármán vortex street. Our data show that the vortex shedding frequency can easily be retrieved from the responses of anterior lateral line nerve fibers.

Personnel supported

Volker Hofmann
Adrian Klein
Gunnar Meyer
Björn Otto
Arne Rüter
Andre Steiner
Kai Voges
Randy Zelik

AIRFLOW ELICITING THE CAPTURE OF FLYING INSECT PREY BY A SPIDER

(Co-PI Friedrich G. Barth, University of Vienna, Austria)

Objectives

- Analysis and mathematical modelling of airflow sensors;
- Examination of the properties of arrays of sensors;
- Analysis of the airflow eliciting the spider's behaviour and identification of the spider's behaviour.

The airflow sensors – Individual hair design and mechanics

MODELLING. Spider -trichobothria and other filiform medium flow sensors are among the most sensitive sensors known. Their remarkable energy sensitivities are close to the thermal threshold. The sensors can be and have extensively been modelled as inverted pendulums representing damped second order mechanical systems.

The modelling part of our work brought to light and clarified numerous aspects of the hairs' mechanical properties and of their response to medium flow. It could not have been accomplished without the expertise (with mathematics and fluid mechanics) of JAC HUMPHREY (University of Virginia). Taking spider trichobothria as the main case we were able to formalize and quantify the properties of filiform sensors to an extent not known of any other biological mechano-sensor, except the vertebrate ear. Our work, which brings together experiments with live animals and physico-mathematical analysis, has now been put together in an exhaustive chapter on "*Medium flow-sensing hairs: biomechanics and models*" contributed to *Advances in Insect Physiology*, Vol.34 (Humphrey and Barth 2008).

ARTHROPOD - INSPIRED FLOW SENSORS. The work described in Humphrey and Barth (2008) permits a detailed interpretation of the functional implications of the various structural parameters of medium flow sensors. As an important consequence reliable predictions can be made on the effects of parameter variation in corresponding synthetic sensors. Thus the theoretical foundation for the development of *bio-inspired flow sensors following principles of arthropod air flow sensors* is exceptionally solid. Arthropod filiform hairs indeed represent an attractive alternative to the lateral line – inspired sensors (based on different physical properties) as developed and fabricated within BioSenSE. A likely advantage of an arthropod inspired hair sensor would be a simpler and easier to achieve way of increasing/adjusting sensitivity and frequency response to particular needs (by adapting the length l of the hair shaft and the elastic restoring force S and possibly also the damping coefficient R of the hair suspension) than is the addition and modification of a "cupula". A paper on the design, fabrication and testing of hair-like fluid motion sensors inspired by the spider work has indeed already been published (see Barbier et al. 2007, Humphrey and Barth 2008) and similar efforts mainly drawing from the work on cricket sensors are those by Krijnen and his group (Krijnen et al. 2007).

COMPARATIVE MICROMECHANICS. A comparison of air flow-sensing cuticular hairs of different arthropods such as spider, scorpion, cockroach and cricket revealed obvious similarities regarding principles of morphological "design" (Figure 49a). Results from the analyses of live

slice preparations made to see how exactly the deflection of the hair shaft is transmitted (transformed) to the sensory cells were particularly illuminating. (a) A prominent feature is the similarity in hair shaft length l (roughly 0.4 to 2 mm) across several vastly differing animal groups reflecting the importance of boundary layer thickness at the relevant signal frequencies as a major evolutionary constraint. (b) Another similarity is that the lever system represented by the hair shaft scales down movement of the hair tip considerably (by a factor of 500 and more) when transforming it to movement of its inner end (on the other side of the axis of rotation of the hair shaft) where the sensory cells attach. Force is thereby scaled up correspondingly. (c) At threshold (hair deflection by 0.1 to 0.01°) the displacement of the mechanosensitive membrane of the sensory cell dendrites is in the range of 1 nm and less, which obviously suffices to change the conductivity of mechanosensitive membrane channels sufficiently to produce an electrical response of the sensory cell (Schaber et al., in prep.).

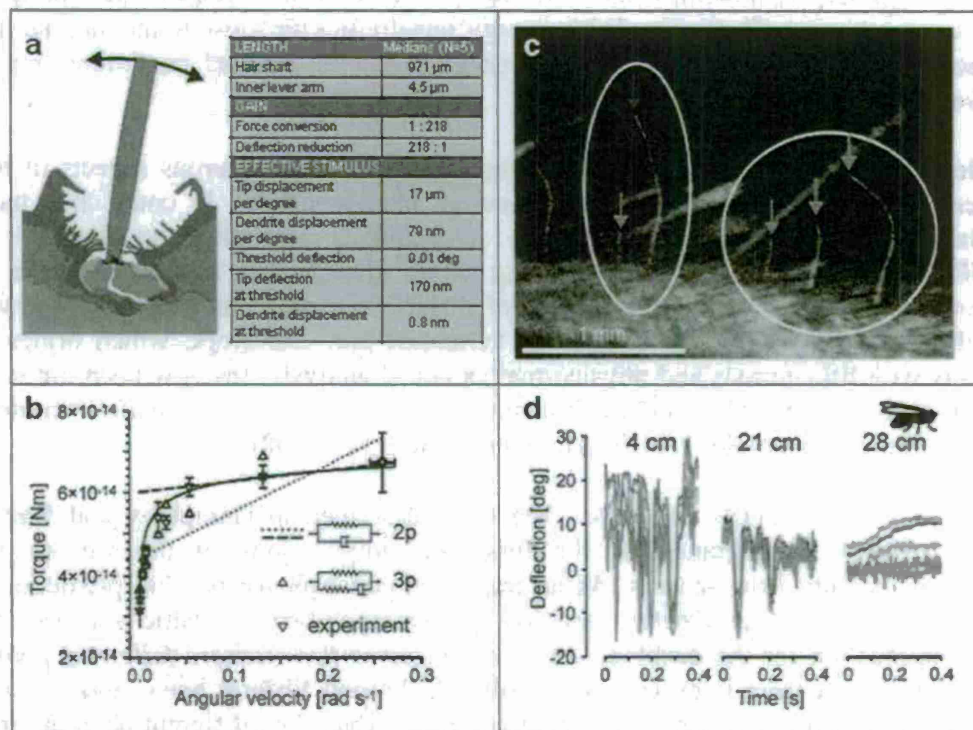


Figure 49: The extremely sensitive arthropod air flow sensing hairs represent a highly elaborate lever system for the transmission of the forces and deflections from the hair shaft to the sensory cells. **a**, Hair suspension of a scorpion trichobothrium; table: Mechanical properties of trichobothria of adult female *Cupiennius salei* spiders. **b**, The suspension of the trichobothria is highly viscoelastic. The experimentally determined and physically-mathematically modeled (2p, 3p) torques necessary to deflect a trichobothrium by a unit angle vary with different deflection velocities. **c**, The trichobothria on the metatarsus of the spider *Cupiennius salei* are arranged in characteristic arrays with hairs of different lengths within a group. **d**, The longer hairs are mechanically tuned to lower and the shorter hairs to higher frequencies. The graph shows the deflection of hairs of different length (color of arrows in c) to the wake of a fly buzzing at different distances from the spider (4 cm, 21 cm, 28 cm). At a distance of 28 cm the wake of the fly does not contain high frequency components anymore which explains the lack of a response of the shortest hairs.

FREQUENCY TUNING. An important aspect for increasing the signal to noise ratio is the proper limitation of the frequency range of the sensors. A fly signal and other prey generated signals typically contain higher frequencies (10Hz and up) than noise (1Hz, background flow). By making the sensor insensitive to air flows lacking the biologically relevant frequencies, selectivity and specificity are achieved. These not only enhance the signal to noise ratio and render the detection and recognition of the relevant signals easier but in addition unburden the central nervous system from complex signal analysis operations. Data based on the analysis of hair movement using laser Doppler vibrometers /LDV (Schaber et al., in prep.) indicate that non flow – sensitive hairs surrounding the flow sensors proper filter out low frequencies, thereby adding to the enhancement of the signal to noise ratio.

HAIR SUSPENSION. The coupling of the hair shaft's inner end to the sensory cells differs greatly from that of any technical solution we know of. It also differs greatly between insects and arachnids. To understand hair motion requires the specification of the torsional restoring parameter S (Nm/rad) and of the damping parameter R (Nms/rad). The procedures developed to quantify these parameters mathematically in combination with LDV measurements are described in Humphrey and Barth (2008).

In a more recent approach taken in collaboration with Vladimir Tsukruk and his laboratory at Georgia Tech surface force spectroscopic point load measurements and viscoelastic modelling were applied to determine the micromechanical properties of the trichobothrial suspension structures (McConney, Schaber et al., 2009, in press). The mechanical properties of the suspension of trichobothria were examined by deflecting the hair shaft with an atomic force microscope (AFM) cantilever at angular velocities ranging from 0.0004 – 0.26 rad/s. Surprisingly, the torque needed to deflect the trichobothrium drops significantly at deflection velocities smaller than 0.05 rad/s (Figure 49b). The measured data can be fitted with a three-parameter viscoelastic standard solid model yielding two spring parameters $S_1 = 2.9 \times 10^{-11}$ Nm/rad, $S_2 = 2.8 \times 10^{-11}$ Nm/rad and a damping parameter $R = 1.5 \times 10^{-12}$ Nms/rad for the hair suspension (Figure 49b). For angular velocities larger than 0.05 rad/s, which are the common ones under natural conditions, a two-parameter Kelvin solid model (also used in earlier work) provides a more accurate angular momentum equation with values for $S = 4.89 \times 10^{-11}$ Nm/rad and $R = 2.83 \times 10^{-14}$ Nms/rad. The most relevant conclusion from these findings is that the viscoelastic properties of the trichobothrium's suspension facilitate the start of hair motion, thereby promoting the phasic response behavior of the sensilla and thus the detection of rapid changes in air flows characteristic of biologically relevant air flow signals.

A similar fine-tuned role of material properties of non-nervous structures in the sensory periphery could recently be demonstrated using atomic force microscopy (AFM), surface force spectroscopy (SFS) and the application of nanoscale forces in another study carried out with Vladimir Tsukruk's group at Georgia Tech (McConney, Schaber et al. 2007). The viscoelastic nature of the cuticular material of a pad located distal to the highly sensitive substrate vibration sensors on the spider legs are largely responsible for this sensor's pronounced high pass characteristics. Young's modulus of the pad is close to 15 MPa at low frequencies (up to ca. 30 Hz) but increases rapidly with increasing frequencies up to ca. 70 MPa at 112 Hz. This finding implies a much reduced energy absorption and thus a much increased efficiency of stimulus transfer to the sensory structures proper. Again we have "adaptive" selectivity way out in the

sensory periphery to aid the detection and recognition of the relevant signals in a noisy environment. A paper on the biological relevance of the glass transition temperature of the pad material in a behavioural context is in preparation (Vogel et al. 2009).

FOUR SENSORY CELLS. Differences in the functional roles of the 4 sensory cells attached to each single trichobothrium are still under electrophysiological study. There are indications that apart from differences in the directionality of their response there may also be differences in the frequency responses (Schaber et al. in prep.). Having several information channels each specialized for a different parameter range (direction, frequency, flow velocity) would indeed significantly increase the power of a single sensor and - in case of synthetic sensors - reduce the number of sensors necessary to be attached to the AUV.

Arrays

DISPERSED ARRANGEMENT. A basic principle in sensory systems detecting and analyzing the spatio-temporal pattern of stimulus fields is the distributed arrangement of the sensors. This is seen in the circular arrangement of ca. 950 trichobothria on the legs all around the body of the spider (compare the dispersed arrangement of the lateral line sensors of fish). Following behavioral experiments the spider "sees" airflow signals equally well in all horizontal directions. Engineers seeking an effective arrangement of sensors on an AUV should pay attention to this. Thus an arrangement of say 8 sensors mounted on a torus protruding into the water might be a reasonable bio-inspired solution. A consideration of the literature on the connectivity of the sensors providing the information needed for a directed response would be helpful for engineering purposes as well (Barth 2002, Franosch et al. 2003, Stürzl et al. 2000, Brownell and van Hemmen

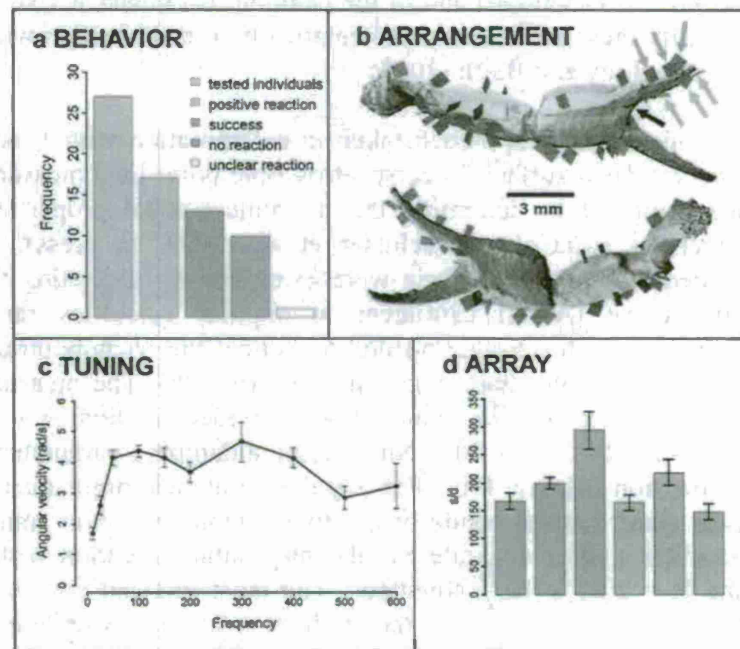


Figure 50: *a*, behavioral reactions (prey capture) of the scorpion *Smeringurus mesaensis* to the airflow generated by a flying moth. From 27 individuals, 17 showed prey capture movements, including 13 successive prey capture attempts. *b*, distribution and planes of oscillation of flow-sensitive hairs on a pedipalp of *S. mesaensis*. Most trichobothria are located on the external surfaces and preferably move in the direction of the pedipalp's long axis. *c*, frequency tuning, average of five 1300 μ m long trichobothria on the external surface of the scorpion's chela (see black arrow in *b*). *d*, s/d (distance/diameter) ratio for the dorsal and external trichobothria on the scorpion's finger (see orange and tan arrows in *b*). Viscosity-mediated coupling is expected not to play any significant role because of the high s/d ratios.

2001).

VISCOSITY - MEDIATED MOTION COUPLING. One of the basic questions in regard to medium flow sensor arrays is the spacing of the individual sensors. There may well be conditions under which the motions of neighboring sensors are not fully independent from each other. Taking an earlier in depth experimental and theoretical analysis of the potential of viscosity-mediated coupling between spider trichobothria (Bathellier et al. 2005; collaboration with JAC Humphrey) as the basis, we now examined corresponding scorpion arrays (Müllan et al., in prep.) (Figure 50). According to detailed morphological studies and the application of laser Doppler vibrometry and high speed video analysis to precisely measure the deflection of hairs in an array (Figures 49c,d) (Schaber et al. in prep.) the general result in both the spider and the scorpion is that the hairs indeed function independently in the relevant range of frequencies. Considering boundary layers the crucial parameter is the s/d ratio, s representing the distance between the sensors and d their diameter. The values found for this ratio are large enough (>30) to justify the neglect of mechanical interaction between hairs in the given cases (Figure 50d). This in turn implies that in an array the differences in the properties of the individual sensors can be used to enlarge the working range (absolute sensitivity, frequency range, directionality). As seen from the motion patterns of trichobothria in an array exposed to a fly- generated airflow (Figure 49d) patterns of hair deflection can be used to determine the distance to the stimulus source.

Synthetic "hair cell" sensors (as fabricated within BioSenSE) and arrays of them would have been an excellent subject to study in regard to the flow around them and the interaction between individual sensors. Unfortunately "hair cell" sensors were not available for that purpose.

POSITION ON BODY. Another big question concerning the arrangement of sensor arrays is: How do details of their position on the body reflect the structure of the flows they are meant to measure? The hypothesis is, that they indeed do reflect important features of the biologically relevant flows. Based on an elaborate surface scan and morphological analysis of the arrangement of the sensors and an LDV study of their mechanical frequency response and directionality (Figures 50b, c) we are currently trying to predict the flow around scorpion pedipalps and to thereby come closer to an answer to the above question (collaboration with JAC Humphrey).

Air flow / Wake tracking

FREELY FLYING FLY. As pointed out in the introduction to this report, knowing the details of a typical flow pattern to which the sensory system under study has been adapted by evolution, is of prime importance. However, it also is a particularly demanding task to identify the details of the airflow generated by a fly passing by and to reveal their relevance for the spider's behavioral response. After having worked extensively with flies flying under tethered conditions it became increasingly evident that an analysis of the flow generated by a FREELY flying fly was indispensable. Such an analysis implies that the fly has to fly within a thin vertical laser light sheet parallel to the spider's plane of symmetry and cutting all four legs on one side of its body.

Using the temporally highly resolved Dantec DPIV system (digital particle image velocimeter) (1000 velocity maps per second!) we now have time resolved velocity magnitude data of the

flow above the spider legs where the trichobothria are located (Klopsch et al. 2007, 2009, and in prep.) (Figure 51). Following a biological rule, the spider obviously does not use complicated mathematical procedures or figure matching but simplifies the analysis of the fly generated flow considerably in order to be able to react promptly and appropriately to it. To make use of simple solutions/rules makes sense in view of the variability of the flows the spider is naturally exposed

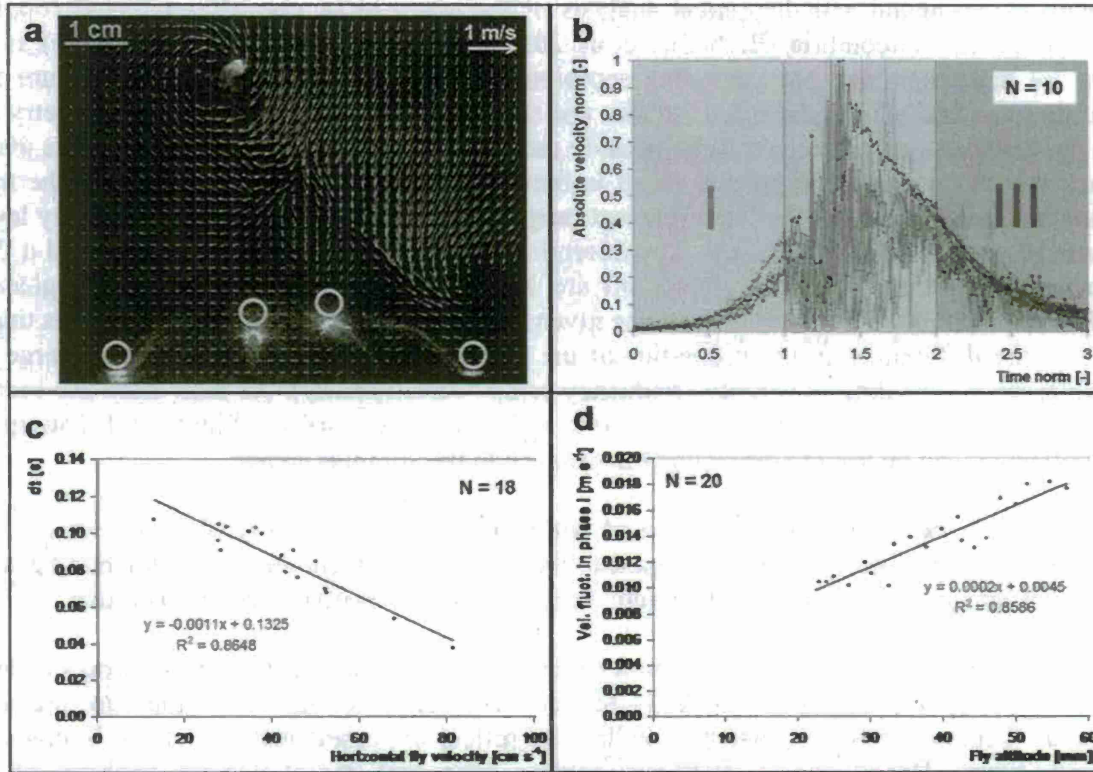


Figure 51: *a*, PIV measurement of the velocity field (velocity vectors) around a freely flying blowfly (approaching from the right) at the location of the spider's airflow sensors on its walking legs (orange circles: measurement sites selected for *b*, *c* and *d*). The flow field around the fly is characterized by a cone shaped wake region pointing downwards and backwards. As the wake moves forward together with the freely flying blowfly air is sucked into the wake region from behind (downwash) and pushed underneath the fly towards the front. This causes a circulating flow around the fly which is detected by the spider when the approaching fly is still several centimeters away (phase I in *b*). *b*, measurements of the absolute velocity of ten flights above a spider leg (for the measuring points see location of the orange circles in *a*). The signal is composed of three phases. In phase I the approaching fly is still in front of the spider's leg causing an exponential increase of the airflow velocity above the leg. The transition from phase I to phase 2 corresponds to a position of the fly directly above the spider's leg. When the fly passes above the leg the spider abruptly receives the highly fluctuating velocity signal from the wake (phase II) before the velocity signal decays again (phase III). Each velocity signal is normalized, its maximum representing 1. In order to make the comparison between different experiments possible the time information regarding the three phases is normalized as well. *c*, Time differences (dt) regarding the time of arrival of the flow signal induced by the fly between leg 1 and leg 4 (position indicated by the two outermost circles in *a*). dt decreases with increasing velocity (horizontal component) at which the fly flies. *d*, The fluctuations of the absolute velocity in phase I increase linearly with the fly's altitude above the substrate (spider).

to. The data we now have are quite unique and promise a lot of attention after having been published properly (Klopsch et al. in prep.).

EXCLUSION OF OTHER STIMULUS MODALITIES. Before concentrating on a detailed analysis of the airflow signal, the effect of other stimulus modalities on the spider's behavior in the given context had to be examined. As demonstrated by many time consuming experiments, vision, substrate vibration and airborne sound are irrelevant in the given context (Klopsch et al., in prep.). It therefore indeed are parameters contained in the airflow which enable the spider to recognize the fly generated signal and to orient towards it.

AIRFLOW PHASES I TO III. As revealed by high speed video analysis (Indiecam GmbH) the spider reacts to an approaching fly and often turns towards it even before it is hit by the fly's wake (which is directed down- and backward at an angle of ca. 45°). As seen in Figure 51a the circulating flow component in front of the flying fly contains velocities large enough (> 1mm/s) to excite trichobothria. This is *phase I* of the flow which is characterized by an exponential velocity increase above the spider leg and a small degree of fluctuation. When the fly is right above the spider the flow changes abruptly to *phase II* (the wake) characterized by both much more fluctuation and larger flow velocities (Figure 51b). The transition from phase I to phase II is the point in time when the spider actually jumps into the air to catch the fly. In *phase III* the signal decays again but at that time the spider has already jumped.

The conclusion then is that *phase I* of the flow raises the spider's attention and informs it about the horizontal direction the fly is coming from. The abrupt *transition from phase I to phase II* triggers the jump. Importantly, we succeeded (Klopsch et al. in prep.) to design artificial flows imitating phase I and phase II and to apply them separately in behavioral experiments. These clearly support our conclusions in regard to their differential relevances.

DETECTION, RECOGNITION, LOCALIZATION, TIMING. Sensor sensitivity is high enough to respond to phase I flow, the frequency tuning of the sensors helps to selectively respond to the relevant signals which contain a typical range of frequencies and increases the signal to noise ratio (which in addition is increased by nocturnal activity when there is little background airflow), and the highly phasic response characteristics (no relevance of DC flow) of the sensors match the fluctuations typical of prey generated signals. Due to the dispersed arrangement of the sensors all around the spider body, differences in the time of signal arrival at the different legs can be and are indeed used by the spider to identify the horizontal direction to the signal source (Brittinger 1998; Barth 2002) and may in addition be used to judge the flight velocity of the prey (Figure 51c). Since the spectral composition of the signal changes with distance (mainly loss of higher frequency components; compare Figure 49d) it can be used to estimate distance to the source; at source distances large enough to result in a background noise like airflow (loss of higher frequency components) the spider does not jump anymore. A possible clue to judge the altitude of the prey fly is provided by the velocity fluctuation in phase I, which increases with altitude (Figure 51d).

GRADIENTS AND THE SELECTIVITY OF THE PERIPHERY. It should be noted that gradients of parameters like velocity magnitude, degree of turbulence, and time of signal arrival play a significant role for the localisation of prey. Organisms in general are much more interested in

changes/gradients than in constant (DC) values, a biological principle of interest to engineering as well. It should also be pointed out, that fine-tuned selectivity and specificity in the periphery is an enormously helpful tool to master complex tasks and to unburden the central nervous system from a lot of "computing". Again, this is a biological principle, which deserves more attention by engineering.

Personnel supported

Clemens Schaber
Christian Klopsch
Rainer Müllan

PUBLICATIONS

- Anderson K D, Lu D, McConney M, Han T, Reneker D, and Tsukruk V V. (2008). Hydrogel Microstructures Combined with Electrospun Fibers and Photopatterning for Shape and Modulus control. *Polymer*, 49, 5284-5293.
- Barbier C, and Humphrey J A C. (2006). "Numerical Calculation of the Flow in the Fish Lateral Line Canal: Applications to Predators Tracking Prey." In: *Proceedings of International Mechanical Engineering Congress and Exposition*, Chicago, Illinois.
- Barbier C, and Humphrey J A C. (2008). Drag Force Acting on a Neuromast in the Fish Lateral Line Trunk Canal: Part I - Numerical Modeling of External-Internal Flow Coupling. *J. Roy. Soc. Interface*
- Barbier C, Humphrey J A C, Paulus J, and Appleby M. (2007). "Design, Fabrication and Testing of a Bioinspired Hybrid Hair-Like Fluid Medium Motion Sensor Array." In: *ASME International Mechanical Engineering Congress & Exposition (IMECE)*, Seattle, Washington.
- Bleckmann H. (2007). "The lateral line system of fish." In: *Sensory Systems Neuroscience*, Hara T and Zielinski B, eds., Elsevier, Academic Press, 411-453.
- Bleckmann H. (2008). Peripheral and central processing of lateral line information. *J. Comp. Physiol. A* 194, 145-158.
- Bleckmann H, and Sand O. (2008). "Determining direction and distance using hydrodynamic input to the lateral line." In: *Springer Handbook of Auditory Research, Fish Bioacoustics*, Popper A and Fay R R, eds., Springer New York, 183-232.
- Bleckmann H, and Zelik R. (2009). Lateral line system of fish. *Integrative Zoology* 4, 13-25.
- Braun C B, and Coombs S. (in press). Vibratory sources as compound stimuli for the octavolateralis systems: dissection of specific stimulation channels using multiple behavioral approaches. *J. Exp. Psychol: Animal Behavior Processes*.
- Brücker H, and Bleckmann H. (2007). Vortex dynamics in the wake of a mechanical fish. *Exp. Fluids*, 43, 799-810
- Chagnaud B P, Bleckmann H, and Hofmann M H. (2007). Karman vortex street detection by the lateral line. *J. Comp. Physiol. A*, 193, 753-763.
- Chagnaud B P, Bleckmann H, and Hofmann M H. (2008). Lateral line nerve fibers do not code bulk water flow direction in turbulent flow. *Zoology*, 111, 204-217.

- Chagnaud B P, Brücker C, Hofmann M, and Bleckmann H. (2008). Measuring flow velocity and flow direction by spatial and temporal analysis of flow fluctuations in nature. *J. Neuroscience* 28, 4479–4487.
- Chagnaud B P, Hofmann M, and Mogdans J. (2007). Responses of dipole stimuli of anterior lateral line nerve fibres in goldfish, *Carassius auratus*, under still and running water conditions. *J. Comp. Physiol. A*, 193, 249-263.
- Chen J, Engel J, Chen N, Pandya S, Coombs S, and Liu C. (2006). "Artificial Lateral Line and Hydrodynamic Object Tracking." In: *MEMS 2006 Conference*, Istanbul, Turkey
- Chen N, Engel J, Chen J, Fan Z, and Liu C. (2005). "Micromachined Thermal Imaging Mesh for Conformal Sensing System." In: *The 4th IEEE International Conference on Sensors*, Irvine, California.
- Chen N, Engel J, Pandya S, and Liu C. (2006). "Flexible Skin With Two-axis Bending Capability Made Using Weaving by Lithography Fabrication Method." In: *MEMS 2006 Conference*, Istanbul, Turkey
- Chen N, Tucker C, Engel J, Yang Y, Pandya S, and Liu C. (2007). Design and characterization of artificial haircell sensor for flow sensing with ultrahigh velocity and angular sensitivity. *J. Microelectromech. Syst.*, 16, 999-1014.
- Coombs S. (2008). Anthropogenic sound sources and the lateral line system. *Bioacoustics*, 17, 65 - 69.
- Coombs S, Anderson E, Braun C, and Grosenbaugh M. (2007). The hydrodynamic footprint of a benthic, sedentary fish in unidirectional flow. *J. Acoust. Soc. Am.*, 122, 1227-1237.
- Coombs S, and Grossmann G D. (2006). Mechanosensory-based orienting behaviors in fluvial and lacustrine populations of mottled sculpin (*Cottus bairdi*). *Mar. Freshwater Behav. Physiol.*, 39, 113-130.
- Coombs S, and Patton P. (2009). Lateral line stimulation patterns and prey orienting behaviors of mottled sculpin. *J. Comp. Physiol. A* 195, 279.
- Dechant H E, Hößl B, Rammerstorfer F G, and Barth F G. (2006). Arthropod mechanoreceptive hairs: modeling the directionality of the joint. *J. Comp. Physiol. A* 192, 1271-1278.
- Engel J, Chen J, Chen N, and Liu C. (2005). "Development and Characterization of an Artificial Hair Cell Based on Polyurethane Elastomer and Force Sensitive Resistors." In: *The 4th IEEE International Conference on Sensors*, Irvine, California, 31 Oct- 31 Nov, 2005.
- Engel J, Chen J, Chen N, Pandya S, and Liu C. (2006). "Multi-Walled Carbon Nanotube Filled Conductive Elastomers: Materials and Application to Micro Transducers." In: *MEMS 2006 Conference*, Istanbul, Turkey
- Engel J, Chen N, Ryu K, Pandya S, Tucker C, Yang Y, and Liu C. (2006). "Multi-layer embedment of conductive and non-conductive PDMS for all-elastomer MEMS." In: *The 12th Solid State Sensors, Actuator, and Microsystems Workshop*, Hilton Head Island, SC.
- Fratzl P, and Barth F G. (under review). Biomaterial systems for mechanosensing and actuation. *Review for Nature*.
- Goulet J, Engelmann J, Chagnaud B P, François J-M P, Suttner M D, and Hemmen J L v. (2008). Object localization through the lateral line system of fish: Theory and experiment. *J. Comp. Physiol. A* 194, 1-17.
- Hill J, Bart-Smith H, Barbier C, and Humphrey J A C. (2006). "Investigation of a Bioinspired Whisker-Like Fluid Motion Sensor." In: *Proceedings of International Mechanical Engineering Congress and Exposition*, Chicago, Illinois.

- Humphrey J A C. (2008). Drag Force Acting on a Neuromast in the Fish Lateral Line Trunk Canal: Part II – Analytical Modeling of Parameter Dependencies. *J. Roy. Soc. Interface*
- Humphrey J A C, and Barth F G. (2007). "Medium Motion Sensing by Arthropods in Air and Water: Comparative Analysis and Implications for Bio-Inspired Synthetic Sensors." In: *ASME International Mechanical Engineering Congress & Exposition*, Seattle, Washington.
- Humphrey J A C, and Barth F G. (2008). "Medium Flow-Sensing Hairs: Biomechanics and Models." In: *Insect Mechanics and Control*, Casas J and Simpson S J, eds., 1-80.
- Humphrey J A C, and Mellon D. (2007). Analytical and Numerical Investigation of the Flow Past the Lateral Antennular Flagellum of the Crayfish *Procambarus clarkii*. *J. Exp. Biology*, 210, 2969-2978.
- Kant R, and Humphrey J A C. (2009). Response of Cricket and Spider Motion Sensing Hairs to Air Flow Pulsations. *J. Roy. Soc. Interface* 1-17.
- Klopsch C, Humphrey J A C, and Barth F G. (2007). "The Air Flow Generated by a Flying Prey Insect around a Wandering Spider and its Motion Sensing Hair Sensilla." In: *5th International Symposium on Turbulence and Shear Flow Phenomena*, Munich, Germany.
- Klopsch C, Humphrey J A C, and Barth F G. (2007). "Arthropod medium flow sensors: II. Properties of natural flows and cues potentially used for orientation." In: *10th Meeting of the Austrian Neuroscience Association*, Seggau.
- Liu C, Bleckmann H, Jones D, Coombs S, Barth F G, Brott L, Naik R, and Humphrey J. (2006). "Artificial haircell and artificial lateral line." In: *Conference on Bioinspired Designs*, Georgia Tech.
- Liu C, Engel J, Chen J, Chen N, Pandya S, Yang Y, Tucker C, Coombs S, Humphrey J, and Bleckmann H. (2006). "Polymer micro and nano scale fabrication technology development for bioinspired sensing." In: *IEEE International Conference on Nano/Micro Engineered and Molecular Systems*, Zhuhai, China.
- McConney M E, Anderson K D, Brott L L, Naik R R, and Tsukruk V V. (in press). Bio-Inspired Material Approaches to Sensing. *Adv. Funct. Mater.*
- McConney M E, Chen N, Lu D, Hu H, Coombs S, Liu C, and Tsukruk V V. (2009). Biologically inspired design of hydrogel-capped hair sensors for enhanced underwater flow detection. *Soft Matter* 5, 292 - 295.
- McConney M E, Schaber C F, Julian M D, Barth F G, and Tsukruk V V. (2006). "Characterization of ultra-sensitive air flow receptors of live wandering spiders." In: *MRS Symposium Mechanics of Biological and Bio-inspired Materials*, Boston MA.
- McConney M E, Schaber C F, Julian M D, Barth F G, and Tsukruk V V. (2007). Viscoelastic nanoscale properties of cuticle contribute to high-pass properties of spider vibration receptor (*Cupiennius salei* Keys.). *J. Roy. Soc. Interface*, 4, 1135-1143.
- McConney M E, Schaber C F, Julian M D, Eberhardt W C, Humphrey J A C, Barth F G, and Tsukruk V V. (2008). Surface force spectroscopy point load measurements and viscoelastic modelling of the micromechanical properties of air flow sensitive hairs of a spider (*Cupiennius salei*). *J. Roy. Soc. Interface*.
- McConney M E, Schaber C F, Julian M D, Humphrey J A C, Barth F G, and Tsukruk V V. (in press). Point load measurements of the micromechanical properties of air flow sensitive hairs of a spider (*Cupiennius salei*) using surface force spectroscopy. *J. Roy. Soc. Interface*.

- McConney M E, Schaber C F, MD M D J, Eberhardt W C, Humphrey J A C, Barth F G, and Tsukruk V V. (2009). Surface force spectroscopic point load measurements and viscoelastic modelling of the micromechanical properties of air flow sensitive hairs of a spider (*Cupiennius salei*). *J. Roy. Soc. Interface*.
- Mellon D, and Humphrey J A C. (2007). Directional Asymmetry in Responses of Local Interneurons in the Crayfish Deutocerebrum to Hydrodynamic Stimulation of the Lateral Antennular Flagellum: Experimental Findings and Theoretical Predictions. *J. Exp. Biology*, 210, 2961-2968.
- Müllan R, and Barth F G. (2007). "Arthropod medium flow sensors: III. Morphological properties of scorpion trichobothria and functional implications of sensor arrays." In: *10th Meeting of the Austrian Neuroscience Association*, Seggauberg.
- Nguyen N, Wiegand I, and Jones D L. (2009). "Sparse beamforming for active underwater electrolocation." In: *Proceedings of the ICASSP 2009*, Taipei, Taiwan.
- Pandya S, Engel J, Chen J, Fan Z, and Liu C. (2005). "CORAL: Miniature Acoustic Communication Subsystem Architecture for Underwater Wireless Sensor Networks." In: *The 4th IEEE International Conference on Sensors*, Irvine, California.
- Pandya S, Yang Y, Jones D L, Engel J, and Liu C. (2006). Multisensor Processing Algorithms for Underwater Dipole Localization and Tracking Using MEMS Artificial Lateral-Line Sensors. *EURASIP Journal on Applied Signal Processing*, 2006(Article ID 76593), 1-8.
- Pandya S, Yang Y, Liu C, and Jones D L. (2007). "Biomimetic imaging of flow phenomena." In: *32nd international Conference on Acoustics, Speech, and Signal Processing*, Honolulu, Hawaii.
- Peleshanko S, Julian M D, Ornatska M, McConney M E, LeMieux M C, Chen N, Tucker C, Yang Y, Liu C, Humphrey J A C, and Tsukruk V V. (2007). Hydrogel-encapsulated microfabricated haircell mimicking fish cupulae neuromast. *Adv. Mater.*, 19, 2903-2909.
- Pillapakkam S B, Barbier C, Humphrey J A C, Rüter A, Otto B, Bleckmann H, and Hanke W. (2007). "Experimental and Numerical Investigation of a Fish Artificial Lateral Line Canal." In: *5th International Symposium on Turbulence and Shear Flow Phenomena*, Munich, Germany.
- Rapo M A, Jiang H, Grosenbaugh M A, and Coombs S. (2009). Using computational fluid dynamics to calculate the stimulus to the lateral line of a fish in still water. *J. Exp. Biol.*, 212, 1494-1505.
- Schaber C F, and Barth F G. (2007). "Arthropod medium flow sensors: I. Sensory hair biomechanics of spider trichobothria (*Cupiennius salei*)." In: *10th Meeting of the Austrian Neuroscience Association*, Seggauberg.
- Schaber C F, McConney M E, Julian M D, Vogel E, Tsukruk V V, and Barth F G. (2007). "Arthropod force detectors: threshold curve of vibration receptor determined by material properties of stimulus transforming cuticle in *Cupiennius salei*." In: *10th Meeting of the Austrian Neuroscience Association*, Seggauberg.
- Sharma S, Coombs S, Patton P, and Perera T B d. (2009). The function of wall-following behaviors in the Mexican blind cavefish and a sighted relative, the Mexican tetra (*Astyanax* sp). *J. Comp. Physiol. A*, 185, 225.
- Yang Y, Chen J, Engel J, Pandya S, Chen N, Tucker C, Coombs S, Jones D L, and Liu C. (2006). Distant touch hydrodynamic imaging with an artificial lateral line. *Proc. Natl. Acad. Sci. USA*, 103, 18891-18895.

- Yang Y, Chen N, Tucker C, Engel J, Pandya S, and Liu C. (2007). "From artificial hair cell sensor to artificial lateral line system: development and application." In: *MEMS 2007 – 20th IEEE International Conference on Micro Electro Mechanical Systems*, Kobe, Japan.
- Yang Y, Jones D L, and Liu C. (under review). Recovery of rectified signals from hot-wire anemometers due to local flow reversal. *Rev. Sci. Instrum.*
- Yang Y, Nguyen N, Chen N, Lockwood M, Tucker C, Hu H, Bleckmann H, Liu C, and Jones D L. (under review). Artificial lateral line with biomimetic neuromasts to emulate fish sensing. *Bioinspiration & Biomimetics*.
- Yang Y, Pandya S, Chen J, Engel J, Chen N, and Liu C. (2006). "Micromachined hot-wire boundary layer flow imaging array." In: *CANEUS 2006 – Micro-Nano Technologies for Aerospace*, Toulouse, France.
- Yang Y, Pandya S, Jones D L, and Liu C. (2007). "Biomimetic flow sensing using artificial lateral lines." In: *The International Mechanical Engineering Congress & Exposition*, Seattle, WA.
- Yang Y, Pandya S, Tucker C, Jones D L, Engel J, Chen N, and Liu C. (2007). "Trail-following of turbulent wake using artificial lateral line." In: *5th International Symposium on Turbulence and Shear Flow Phenomena*, Munich, Germany.

REPORT DOCUMENTATION PAGE				Form Approved OMB No. 0704-0188	
<p>The public reporting burden for this collection of information is estimated to average 1 hour per response, including the time for reviewing instructions, searching existing data sources, gathering and maintaining the data needed, and completing and reviewing the collection of information. Send comments regarding this burden estimate or any other aspect of this collection of information, including suggestions for reducing the burden, to the Department of Defense, Executive Service Directorate (0704-0188). Respondents should be aware that notwithstanding any other provision of law, no person shall be subject to any penalty for failing to comply with a collection of information if it does not display a currently valid OMB control number.</p> <p>PLEASE DO NOT RETURN YOUR FORM TO THE ABOVE ORGANIZATION.</p>					
1. REPORT DATE (DD-MM-YYYY) 23-07-2009		2. REPORT TYPE Final Report		3. DATES COVERED (From - To) July 2005 to June 2009	
4. TITLE AND SUBTITLE Bioinspired Haircell Receptive Sensors			5a. CONTRACT NUMBER		
			5b. GRANT NUMBER FA9550-05-1-0459		
			5c. PROGRAM ELEMENT NUMBER		
6. AUTHOR(S) Chang Liu, Douglas Jones, Vladimir Tsukruk, Joseph Humphrey, Rajesh Naik, Sheryl Commbs, Horst Bleckmann, Friedrich Bath			5d. PROJECT NUMBER		
			5e. TASK NUMBER		
			5f. WORK UNIT NUMBER		
7. PERFORMING ORGANIZATION NAME(S) AND ADDRESS(ES) Northwestern University, Mechanical Engineering, 2145 Sheridan Rd, Evanston, IL 60208 UIUC, Coordinated Science Laboratory, 1308 W Main St, Urbana, IL 61801 Georgia Tech, University of Virginia, Air Force Research Laboratory, Bowling Green University, University of Bonn, University of Vienna			8. PERFORMING ORGANIZATION REPORT NUMBER		
9. SPONSORING/MONITORING AGENCY NAME(S) AND ADDRESS(ES) Defense Advanced Research Projects Agency 3701 North Fairfax Drive, Arlington, VA 22203			10. SPONSOR/MONITOR'S ACRONYM(S) DARPA		
			11. SPONSOR/MONITOR'S REPORT NUMBER(S) AFRL-DSR-VA-TR-2002-0489		
12. DISTRIBUTION/AVAILABILITY STATEMENT Approve For Public Release					
13. SUPPLEMENTARY NOTES					
14. ABSTRACT Artificial lateral line sensing technique inspired by the lateral line of fish has been developed through interdisciplinary collaborations among engineers, material scientists and biologists. Constituted by numerous superficial neuromasts and canal neuromasts, the lateral line of fish has been studied from both biological and engineering perspectives. By learning from the anatomic structure and the sensing mechanism of the biological system, superficial biomimetic neuromast (BN), canal BN, BN with artificial cupula, and artificial lateral line (ALL) have all been realized using MEMS technology and characterized under various flow conditions. The superficial BN has achieved unprecedented high sensitivity in fluid flow sensing. The canal BN demonstrated low-pass filtering and selective sensing capabilities. The artificial cupula pushed the BN's sensitivity to an even higher level. At the system level, different ALLs have been configured for some typical biologically-relevant flow-sensing scenarios using superficial or canal BNs. Implemented with specially developed algorithms, the ALLs successfully localized some underwater vibrating sources via hydrodynamic imaging, and demonstrated schooling capability.					
15. SUBJECT TERMS lateral line, artificial lateral line, artificial lateral line canal, neuromast, biomimetic neuromast, cupula, hydrodynamic imaging, localization.					
16. SECURITY CLASSIFICATION OF:			17. LIMITATION OF ABSTRACT	18. NUMBER OF PAGES 66	19a. NAME OF RESPONSIBLE PERSON Chang Liu
a. REPORT	b. ABSTRACT	c. THIS PAGE			19b. TELEPHONE NUMBER (Include area code) (847) 467-0701

